3-2014

Multimodal Imaging and Characterization of Biofilms

Kunal Vaidya

Multimodal Imaging and Characterization of Biofilms

by

Kunal Vaidya

B.S. Manipal University, 2007

M.S. Illinois Institute of Technology, 2009

A dissertation submitted in partial fulfillment of the requirements for the degree of Doctor of Philosophy in the Chester F. Carlson Center for Imaging Science, College of Science, Rochester Institute of Technology

March 2014

Signature of the Author: _____

Accepted by: _____

Coordinator, Ph.D. Degree Program Date

CHESTER F. CARLSON CENTER FOR IMAGING SCIENCE
COLLEGE OF SCIENCE
ROCHESTER INSTITUTE OF TECHNOLOGY
ROCHESTER, NEW YORK

CERTIFICATE OF APPROVAL

PhD Degree Dissertation

The PhD degree dissertation of Kunal Vaidya has been examined and approved by the thesis committee as satisfactory for the dissertation requirement for the Doctor in Philosophy degree in Imaging Science

_____
Dr. Daniel Phillips, Outside Chair

_____
Dr. María Helguera, Adviser

_____
Dr. Naval Rao, Committee Member

_____
Dr. Michael Pichichero, Committee Member

Dedicated to my uncle Jagdish Tandon
and my parents

Acknowledgements

I would like to thank Dr. María Helguera for her tireless support throughout the course of my graduate studies. Her constant encouragement made me believe in my abilities during times when things did not seems to be going in the right direction. She has played a pivotal role in my development as a scientist. She has been my greatest ally and has surpassed my expectations as an advisor. Thanks to Dr. Pichichero for introducing to me the problem that this thesis attempts to address, for providing access to his lab facilities and the expertise of his team at Rochester General Research Institute. His feedback was instrumental in preparing this dissertation document. Thanks to Dr. Rao for his invaluable guidance especially in relation to brainstorming SNR improvement techniques. He was my go-to person for discussing technical details of the methods I considered for my research work. Thanks to Dr. Phillips for providing his feedback during the process of preparing my thesis. I would like to convey my gratitude to Dr. Dabin Ren, Janeese Stevenson and Dr. Robert Osgood for preparing my culture plates as per my requirement. My friends in Rochester have helped me maintain a great work-life balance which has helped me work more efficiently. Special thanks to Samreen Jatana for her support throughout the course of my graduate studies.

I would like to thank my mother Jyoti Vaidya and father Dr. Pawan Vaidya for all their love and support throughout my life, especially to my father for nurturing the sense of curiosity in me that has helped me in my training as a scientist. I would like to thank my aunt Sucheta Tandon and my late uncle Dr. Jagdish Tandon for making me feel at home here in Rochester. Jagdish uncle has been an inspiration and his memory will continue to live on forever in my heart.

This dissertation would not have been possible without the support of the Center for Imaging Science. This work was supported, in part, by grants from a CIS Innovative Research Grant, COS Dean-Research Innovation Grant, Rochester Institute of Technology-Rochester General Health

System Alliance to María Helguera and Michael E. Pichichero, and NIH NIDCD R0108671 to Michael E. Pichichero.

The RIT confocal microscopy lab is supported through the National Science Foundation Major Research Instrumentation Program (#1126629), the RIT Office of the Vice President for Research, the Kate Gleason College of Engineering, and the RIT College of Science.

Abstract

Bacterial infection is a rampant problem faced by the medical community. The bacteria gene pool is capable of adapting itself to changing conditions building biofilms to ensure the survival of progeny. This ability reduces the efficiency of antibiotics and protects the bacteria from immune system eradication, prompting the need for a technology capable of early detection of biofilms. The ability to non-invasively image and characterize bacterial biofilms in children during nasopharyngeal (NP) colonization with potential otopathogens and during acute otitis media, (AOM) would represent a significant advance. Identifying the properties of biofilms is a crucial step towards establishing a viable imaging detection plan. In this thesis work two modalities based on different imaging principles were used to study the properties of biofilms and map their progression based on quantitative metrics as a function of time. Systematic time studies were performed on three preparations of an isolated *Haemophilus influenzae* (NTHi) species, *Streptococcus pneumoniae* (Sp) and a combination of *Haemophilus influenzae* and *Streptococcus pneumoniae* (NTHi+Sp)in an *in vitro* environment (N=3). A 15 MHz ultrasound acquisition system was built to study the detection of biofilms with ultrasound. Various spectral parameters - peak frequency shift, bandwidth reduction, intercept, mid-band fit, and integrated backscatter coefficient (IBC) - were recorded in a time study of biofilm growth by the bacteria and underlying trends in the progression of these metrics were attributed to the biofilms construction of specific bacteria or the combination of 2 bacteria. The frequency content of the backscattered signal was compared to a theoretical Form Factor model to estimate the effective scatter size which was also used as a characterization metric for biofilm growth. To confirm the ultrasound observations a second imaging modality was applied. Confocal laser-scanning microscopy produces 3D high-resolution time resolved data. Volumetric analyses of confocal microscopy data were used to further define structural properties of biofilms and complement ultrasound-based findings.

Table of Contents

LIST OF FIGURES

Chapter 1

1.1 Introduction and Motivation

Ultrasound Imaging has been widely used as a diagnostic imaging modality due to its non-invasive and non-ionizing properties. Traditionally ultrasound has been used to produce images from envelope detected radio frequency (RF) signals that show the visual structure of the target to make a diagnosis. These RF signals are created from reflections from acoustically different interfaces in the target. There has been a recent thrust in the use of ultrasound as a quantitative tool to discern properties of biological materials. Ultrasonic non-destructive testing is widely used in the industry to study the structure of materials. Ultrasonic RF echo signals contain more information than that pertaining to the structure alone. Modern signal processing techniques can be used to unearth a wealth of information that provides further insight into the properties of materials. Applications where structural B-mode images do not provide useful diagnostic information due to the discrepancy between the wavelength of ultrasound and the size of the scatterers in the targeted material are ideal for quantitative analysis of the interaction of the target with ultrasound. This information can be used to make accurate diagnostic decisions. The study of the interaction of ultrasound with biofilms has been carried out as a part of this dissertation.

Bacteria are microscopic organisms that reproduce by binary fission. At the average $37^{0}C$ body temperature, an entire population of bacteria can double in only 9.8 minutes [1]. Many of these rapidly growing populations of bacteria are also capable of growing in an exopolymer encased biofilm, a type of aggregative growth attached to a surface. The exopolymer is an organism-produced substance that may be composed of a variety of components that encases the bacteria to function as a shield, against which antibiotics and

the immune system are ineffective in curing infection [2]. Antibiotics and the immune system attack free-floating (planktonic) organisms, but are unable to eradicate bacteria encased in a biofilm. Biofilm-related infections are a major health problem. Biofilms often form on the surface of catheters inserted into ill persons to monitor blood pressure and urine output and on catheters used to infuse medicines to cancer patients [3]. Biofilms also form on the surface of tissues. Bacteria embedded in biofilms can cause infections observed in persons with cystic fibrosis. Previous research has shown that biofilms also form in the middle ear space during chronic and recurrent ear infections thereby making the infections recalcitrant to antibiotic treatment [2, 4]. Two bacteria species account for 90% of all ear, sinus and lung infections in children and adults; they are *Haemophilus influenzae* and *Streptococcus pneumonia* [5]. These same bacteria start the disease process by occupying the nose and throat [3, 6, 7] before ascending to the middle ear, [8-10] sinuses or lungs to cause infections so their detection in a biofilm in the nasopharynx would provide valuable medical information to the clinician. Currently there are no available technologies to detect the bacterial composition of a biofilm in vivo. There is an urgent medical need for such technology.

In order to correctly discern a bacterial biofilm from structures they attach to (catheters and human tissue surfaces), the acoustic properties of biofilms, in response to ultrasound, would need to be known. These characteristics could then be used to identify a biofilm *in vivo*, either on a plastic catheter or attached to the epithelial cells lining the nose, throat, middle ear, sinuses, or lung [11].

This dissertation investigates the acoustic and structural properties of *Haemophilus influenza and Streptococcus pneumonia* and a combination of the two as a co-culture in an

in vitro environment. Ultrasound is a cost effective diagnostic tool with great potential to be used in a clinical setting. The goal of my thesis project was to establish the efficacy of ultrasound as a diagnostic tool to determine the presence of biofilms and identify the differences in 2 bacterial species based on *in vitro* experiments. This project is innovative in application of quantitative ultrasound techniques to study biofilms formed by the aforementioned species that cause upper and lower respiratory infections.

A previously applied modality to study the structural properties of biofilms ex vivo is confocal microscopy. This modality produces images of superior resolution as compared to ultrasound; however, it cannot be used in a clinical setting as an in vivo application. This project uses confocal microscopy to corroborate the structural properties of biofilms compared to ultrasound-based findings.

1.2 Literature Review

Several researchers have used quantitative ultrasound techniques to characterize biological materials. Waag *et al.* [12] demonstrated the use of quantitative ultrasound in characterization using power spectra in isotropic media. Insana *et al.* [13] used pulse-echo ultrasound to describe small-scale structure in random media. Libgot-Calle *et al.* [14] used high frequency ultrasound to investigate the acoustic properties of whole blood during coagulation. Seth *et al.* qualitatively characterized middle ear effusions using ultrasound in terms of the viscosity of middle ear fluid using a comparison study involving 56 children between the age of 6 months and 17 years [15].

Accurate characterization of biofilms requires the use of pre-processing techniques to pre-condition the signal and ensure the use of efficient acquisition and processing parameters.

Liu and Zagzebski [16] demonstrated tradeoffs in these parameters, which were considered during data acquisition and subsequent processing.

Shemesh *et al.* [11] have proven that 50 MHz ultrasound can be used to image *Streptococcus mutans* biofilms on tooth enamel. They used the internal software of a Vevo 770 transducer to create two-dimensional and three-dimensional structural images of the biofilm and verified that from the second to seventh day of growth, the thickness of the biofilm increases. Kujundzic *et al.* [17] used high frequency ultrasound to monitor growth of biofilms on polymeric surfaces.

In [4] Bakaletz reviews the role of bacterial biofilms in the pathogenesis of otitis media and outlines the challenges faced by the medical community in identifying and treating biofilm infections.

Several researchers have used Confocal laser scanning microscopy (CSLM) as a tool to visualize their samples. Gennip *et al.* [18] demonstrated the use of CSLM to visualize biofilm development *in vivo* following intraperitoneal inoculation of mice with bacteria growing on hollow silicone tubes, as well as to examine the interaction between these bacteria and the host innate immune response. However there are very few studies that use the confocal data to quantitatively characterize the progression of biofilms as a function of time.

In [19] Heydorn *et al.* used a computational approach to characterizing a three dimensional stack of biofilms based on a set of quantitative metrics. Their study has been used as a starting point to build on for volumetric and textural analysis of confocal data of biofilms.

1.3 Overview of the Thesis Project

The first step towards detecting biofilms in vivo is the study of their properties in an *in vitro* environment based on quantitative parameters. Useful information about the unique properties of materials that interact with ultrasound waves can be found in the spectral content of the received echo RF signals. Processing the spectral content on these RF data can illuminate unique properties that are otherwise indiscernible. Knowledge of these properties may help lead to the detection of the presence of a mono-species biofilm, differentiate between mono-species biofilm formed by different species of bacteria or even detect multispecies biofilm. While many research groups have investigated the capability of ultrasound imaging of biofilms, the acoustic properties are still relatively unknown.

The specific aims of this project were to:

- Build a customized ultrasound acquisition system to collect RF data.
- Acquire data and develop pre-processing software for data visualization.
- Investigate and implement signal processing techniques to improve Signal to noise ratio (SNR) of ultrasound signal.
- Perform time studies of the aforementioned species in biofilms.
- Develop data quantification software to study the interaction of the ultrasound with the biofilms and use them to demonstrate reproducible trends corresponding to individual species and combination of species.
- Collect confocal microscopy data and perform characterization on the volumetric data based on metrics that describe the structure of biofilms in a similar time study.

- Study the conclusions based on confocal data to draw parallels between acoustic and confocal experiments.

1.4 Organization of report

- Chapter 2: Ultrasound Fundamentals and Custom Built Acquisition System: This chapter covers an overview of ultrasound imaging and specific details of the customized ultrasound acquisition system used for the study of biofilms.
- Chapter 3: Biofilms: This chapter gives a brief overview of what biofilms are and specifics of the two species of biofilms used in this study. The process of preparation of these biofilms is also outlined here.
- Chapter 4: Pre-processing of Ultrasound Signal: this chapter covers some signal processing techniques used to improve the SNR of the signal and the impact on the accuracy of the characterization process. These include Wavelet denoising techniques and frequency encoded pulse compression techniques.
- Chapter 5: Quantitative Characterization: This chapter gives a detailed description of the quantitative metrics used to evaluate changes in the biofilm over a span of time, experimental protocol and results.
- Chapter 6: Effective scatter size estimation: This chapter covers the theory behind using theoretical form factor models to estimate effective scatter size which is used as a characterization metric.
- Chapter 7: Confocal Microscopy: This chapter outlines the use of Confocal Microscopy to overcome the limitations of ultrasound imaging to produce higher

resolution time resolved 3D stacks of data. Metrics used to describe structural properties based on this data are described.

- Chapter 8: Results and conclusions: In this chapter the results of the two independent modalities used are presented and the trends observed are compared.

1.5 Papers published based on this research

- Vaidya, K., Osgood, R., Ren, D. Pichichero, M., Helguera, M., "Ultrasound Imaging and Characterization of Biofilms Based on Wavelet Denoised RF Data", *Ultrasound in Med. & Biol., Vol. 40, No. 3, pp. 583–595, 2014*
- Vaidya, K., Helguera, M., Ultrasound Characterization of Biofilms Using Wavelet Denoised RF Data, *ISBI, 2012, Image Acquisition and Reconstruction, Barcelona, Cataluña, Spain* (Poster Presentation), 2012
- Vaidya, K., Hatfield, K.; Helguera, M.; Pichichero, M., High Frequency Ultrasound Imaging and Characterization of Biofilms, *IEEE International Ultrasonic Symposium, Ultrasonics, Orlando, Florida, United States,* 2011
- Vaidya, K., Hatfield, K.,Helguera, M., Pichichero, M., Building Parametric Images of Biological Materials using High Frequency Ultrasound, International Conference on Biomedical Engineering, Manipal University, India, 2011

Chapter 2

Ultrasound is a cyclic sound pressure wave with frequency above the upper hearing limit of the human ear. A typical ultrasound imaging system comprises of a transducer that produces the ultrasound, a detector to sense the echo signal, which could be the same transducer that produces the ultrasound, a post processing unit and a display device for a human observer. An ultrasound transducer generates a mechanical wave, which bounces off the target and is collected back by the same transducer or a separate receiver. The echo signal is generated by the interaction of the pulse with the object being imaged. The received signal is used to produce a one-dimensional image along the line of sight of the transducer. Several adjacent lines create a raster two-dimensional image. The echo signals collected by the detector can be processed and arranged in several different ways for display to suit specific applications.

2.1 Analytical System Model

Macovski [20] derives a basic reflection model based on the following assumptions

- The diameter of the transducer is considered to be much larger compared to the wavelength of the propagation wave.
- The wave propagates with a velocity c, which is uniform throughout the medium of propagation and is attenuated with an attenuation coefficient α, which is also assumed to be constant.
- The target is modeled as an array of isotropic point scatterers having a reflectivity, R(x, y, z) that is assumed to be independent of the angle of approach of the ultrasound beam.

The following equation describes a two-dimensional ultrasound imaging system:

$$e(t) = K \left| \iiint \frac{e^{-2\alpha z}}{z} R(x,y,z) s(x,y) \breve{p}\left(t - \frac{2z}{c}\right) dxdydz \right| \qquad (2.1)$$

where

- K is a normalizing constant
- R(x, y, z) is the reflectivity if the body modeled as an array of isotropic point scatterers.
- α is defined as the attenuation coefficient, which is frequency dependent.
- s(x, y)is the lateral distribution of the propogating wave.
- $\breve{p}\left(t - \frac{2z}{c}\right)$ is the received pulse delayed by the round trip and modified by various linear processes like attenuation, scattering and diffraction.

The received pulse $\breve{p}(t)$ is the convolution of the transmitted pulse with the impulse responses of the transducer and other linear filters in the system. The envelope detected received pulse which is devoid of phase information is used to generate B-scan images.

There are four commonly used methods of displaying ultrasound echo data, which vary upon the complexity and amount of processed data.

2.1.1 A-scan Mode

This is the simplest mode in which a one-dimensional display of voltage versus time signal is generated. It is observed by connecting the received output from a transducer to an oscilloscope. The disadvantage of the A-scan mode is that it provides information about the object only along the line of sight and within the beam width of the transducer and it is tedious and time consuming to move the transducer laterally hence this modality cannot be used for real time applications. Quantitative ultrasound predominantly used this mode.

2.1.2 B-scan mode

This is the most common mode used to display an image of a target; B-scan images are essentially display of adjacent A-scan signals that are generated when the transducer is moving laterally. Only the envelope of the amplitude of the signal is used in the display. A 2D image is generated in the X-Z plane determined by the range direction and scanning direction. The brightness in the image provides a crude picture of the target.

2.1.3 C-scan mode

This refers to constant depth scanning mode that utilizes pulse echo signals. An electronically gated portion of the A-scan signal is used. The transducer has to be scanned laterally in the X-Y plane for this modality. The brightness image provides a picture of the scatterers/ reflectors located in the thin slice in the X-Y plane of the object at a distance z. The advantage is that the transducer can be focused at an optimum depth and optimum resolution can be maintained at all portions of the image. This modality is primarily used in non-destructive testing.

2.2 Ultrasound scattering Model

Ultrasound waves go through three types of scattering: specular, diffusive and diffractive [21] .

- Specular scattering: This occurs when the scattering object is large compared to the wavelength. In this case, the reflection process can be approximated as an incident ray with the scattered wave front following the shape of the object.
- Diffusive scattering: This occurs when the scattering object is small compared to the wavelength. The resulting scattering radiates in all directions with insignificant phase difference among reflections from the surface of the object.

- Diffractive Scattering: This occurs when the object size is in between the two extremes above.

The pulse propagation can be modeled through the material frequency response (MFS) written as a function of frequency, *f*, and depth of penetration, *z*, in the following manner

$$MFS(f,z) = e^{(\gamma(f).z)} \quad (2.2)$$

$$\gamma(f) = -\alpha(f) - i\beta(f) \quad (2.3)$$

$$\alpha(f) = \alpha_0 + \alpha_1|f|^y \quad (2.4)$$

$$\beta(f) = k_0(f) + \beta_E(f) \quad (2.5)$$

where $k_0 = 2\pi f/c_o$, c_o being the velocity of sound usually taken at the center frequency of the spectrum, $\beta(f)$ is an excess dispersion term resulting in frequency dependent phase velocity, and $\alpha(f)$ is the frequency dependent attenuation following power law (α_0, α_1, and *y* are constants). If a pressure $P_0(f)$ is applied at depth *z = 0*, the pressure at any depth *z* is then given by:

$$P(f,z) = P_0(f).MFS(f,z) \quad (2.6)$$

The inverse Fourier transform of *MFS(f, z)* can be used to determine an equivalent time response at any depth. Based on this, the following characteristics can be derived:

- Signal attenuates exponentially with distance and frequency. It is usually considered to be 0.5 dB per MHz per cm in tissues.
- In time domain, the signal response broadens with depth. At shorter distance, response is impulse like and with depth it spreads over time.

- In frequency domain, there is a slight downward shift of peak in the resulting frequency spectrum with depth of penetration when a shaped (e.g., Gaussian) pulse is applied.

2.3 Ultrasound data acquisition system

Commercial ultrasound scanners do not provide access to radio frequency data. In order to circumvent this problem a customized ultrasound data acquisition system (DAQ) was setup. Figure 2.1 shows a block diagram of the system. A metal frame supports the stepper motors that help maneuver retrofit table high frequency transducers. Figure 2.2 shows a snapshot of the system.

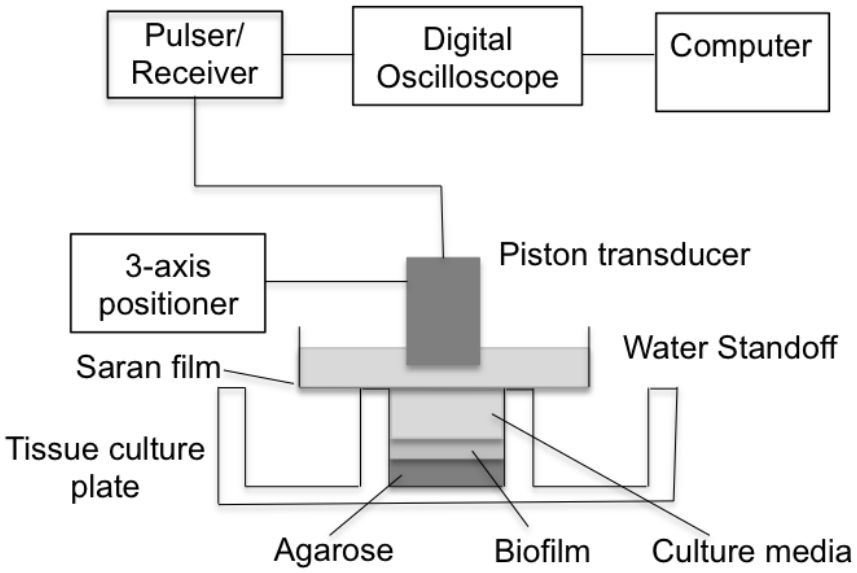

Figure 2.1: Block diagram of ultrasound DAQ system

The system comprises of the following components:

- High Frequency Transducers (Olympus, Waltam MA)
- Panametrics and JSR pulser (JSR, Rochester NY)

- LeCroy Oscilloscope (Chester Ridge NY)
- Velmex Motors (Velmex, Bloomfield NY)
- RITEC Broadband receiver for Amplification (RITEC, Warwick RI)
- Tektronix Function Generator (Tektronix, Beaverton OR)

Figure 2.2: Snapshot of ultrasound DAQ system

Figure 2.3: Retrofit table ultrasound transducers

The Panametrics pulser/receiver was used to generate the trigger signal, which was fed to the ultrasound transducer. The output of the transmit-receive switch was connected to a pre-amplifier to amplify the reflected signal. The signal was then digitized using a LeCroy wave Runner 6051 (Chester Ridge, NY) digital oscilloscope. Channel one of the oscilloscope was used to capture and analyze the reflected RF signal.

A LabView program, controls the overall acquisition process, obtains the waveform data from the oscilloscope, while also communicating with the stepper motor controller in order to translate the transducer to the next collection location. The oscilloscope used was a LeCroy wave Runner 6051 (Chester Ridge, NY) 500MHz Oscilloscope Dual 5 Gs/s. Stepper motors, for the X-Y plane directions, were controlled by a VELMEX VXM Stepping Motor Controller. The stepper motors can travel a maximum of 5.08cm, with a minimum translational step size of 2.5μm. Figure 2.3 and 2.4 shows a snapshot of the ultrasound DAQ and the different kinds of transducers than can be used.

2.3.1 Labview Program

The LabView program is a stand-alone user interface that allows for the customization of scan dimensions, storage location, and analysis features. A graphical user interface (GUI) was used to control the system. Figure 2.4 shows a screen shot of the GUI. There are two pages to the program, the first for scan dimensions and the second for analysis features. When the program is first run, the user is allowed to choose where the final waveform file, log file, and parametric images will be saved. The user also has the option to create a new scan or run a previous scan, using information stored in the log file.

For memory purposes, the waveform file is stored on the host computer while the

waveform is being collected and when finished, the file is moved to the chosen storage location. A log file is also written to the same storage location. This log file contains the starting coordinates of the transducer, the scan type, dimensions, and resolution, and the number of points collected per waveform. Both the log file and the waveform file are written as a text file with comma separated values for ease of use with other programs. During the analysis, the Matlab script within the LabView program, reads the waveform and log files from its permanent location. Beginning on the first page of the program, shown in Fig. 4a, the user can select the type of scan: Positive X, Negative X, Positive Y, Negative Y, or Raster. These dimensions correspond to the positive and negative linear movement of the motors. The raster scan, shown graphically in Figure 2.5, is a two dimension scan that collects data while traveling in the positive x direction, stops collecting data while the motors return to the beginning of the row, moves to the next row down, and again collects data while traveling in the positive x direction. In Figure 2.5, the return trip to the beginning of each row is shown below the initial trip in the positive x direction just for clarity of the diagram, the transducer only moves down to the next row once it has returned to the beginning of the current row. The four text boxes allow the user to input the numerical scan dimensions and resolution. The "Number of Readings" X and Y fields are the number of locations to collect data in the x and y dimensions, respectively. The "Number of Steps" X and Y fields the distance between each read, which is measured in steps. A single step made by the motor translates it 2.5 μm, so this is both the minimum resolution of the motors and the restriction on read locations. For example, the motor is unable to acquire samples every 1.5 μm because that would require the motors to move less than one step, which it cannot do. Also, the motor can only move in multiples of 2.5

μm, so the two smallest resolutions between two read locations in 2.5 μm and 5 μm. Two read locations cannot be 3 μm apart. In some cases, these restrictions make the motors the limiting factor of the imaging system, but sometimes the resolution of the transducer is larger and so the transducer would then be the limiting factor. Once the user is finished with the first page, he or she can continue to the second page. This page contains the processing specifications, various motor control options, and the start button. If the user wants the collected data to be processed, the "Post Process" checkbox must be checked. The output of the post processing depends on the scan type selected. If one dimensional scans are selected, only A-lines and B scans are created but if the raster scan is selected, C scans are also created. The C scan provides a view into the object, which can only be obtained by scanning in two dimensions. In order to look "into" the object for the C scan, a depth value array is needed. The user can input the values at which depth slices are to be taken. The user can chose the depth values from the oscilloscope, determining the locations of interesting features. The buttons "Manual Mode", "Coordinate Mode", and "Reset Motors" change the location of the transducer. The manual mode allows for the user to translate the transducer using the jogging buttons on the motor controller box. This feature is often used to move to a different spot on the material being scanned. The coordinate mode allows for the user to input specific coordinates that the transducer will be moved to. If a time study is being performed and multiple locations are being scanned, the coordinates can be collected from the log file and the motor can be quickly translated to the required locations. When it comes time to scan the multiple spots, the user can input each of the coordinates into the coordinate mode to move the transducer to each spot. The reset mode moves the transducer to the origin of the motors.

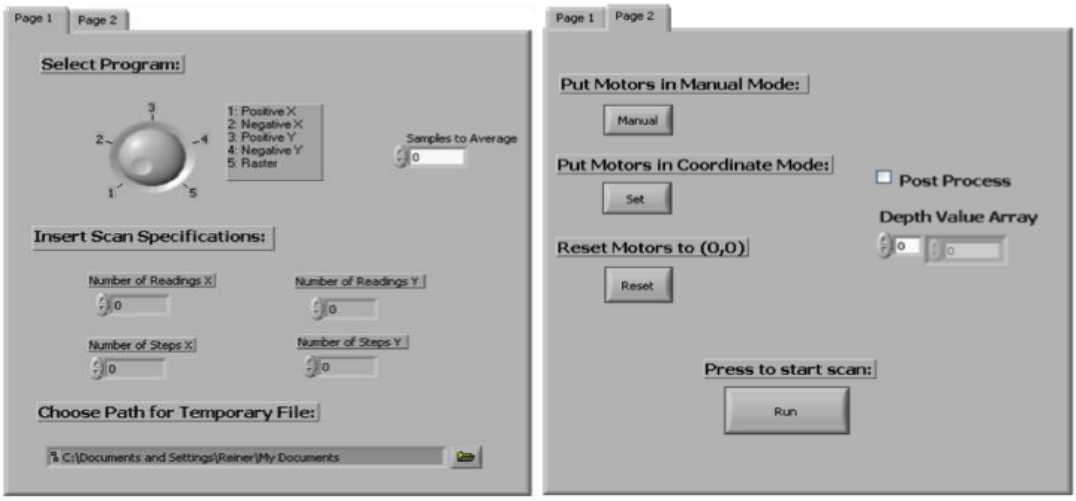

Figure 2.4: Screen shot of LabView GUI

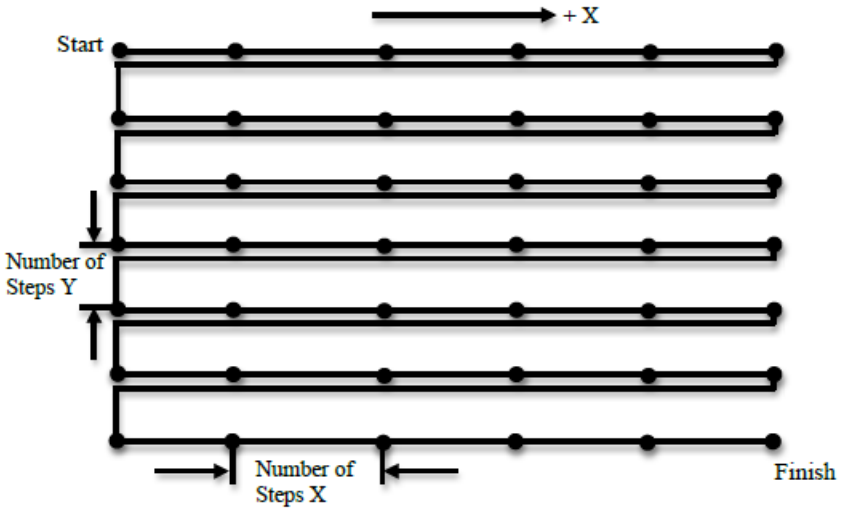

Figure 2.5: Raster scan

The data collected by the oscilloscope is imported into a computer as a text file containing time and corresponding amplitude of the signal. A Matlab (Mathworks, Natick MA) script was written to generate A-scan B-scan C-scan images from the data imported. Figure 2.6 shows the orientation of the three types of images generated from a cube of data. Figure 2.7 (a), (b) and (c) show the A-scan, B-scan and C-scan image of a washer imaged using a 15 MHz transducer with the DAQ system.

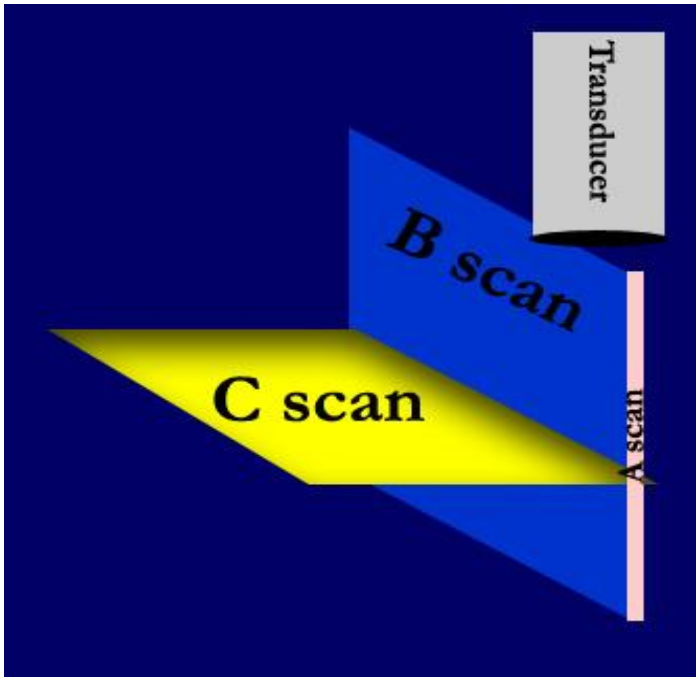

Figure 2.6: Schematic showing orientation of A-scan, B-scan and C-scan images

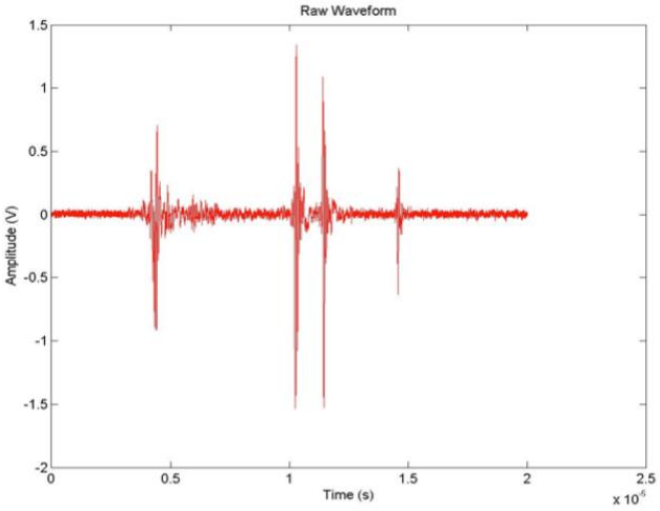

(a)

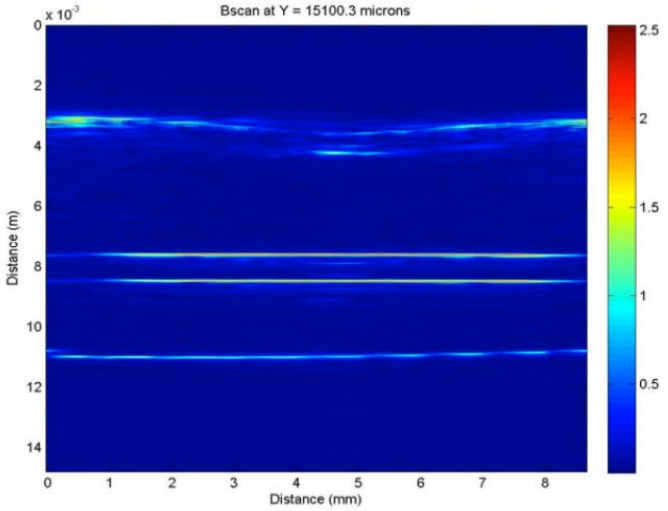

(b)

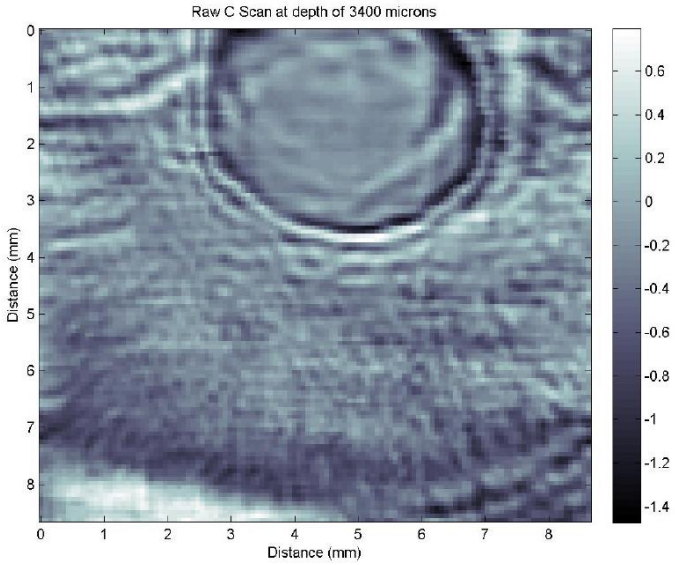

(c)

Figure 2.7(a): A-Scan Plot, (b): B-scan image, (c): C-scan image at depth of 3400**μm**

2.4 Transducer Characterization

An important step in ultrasonic research is characterization of the imaging system, which removes the effects of the system on the data. Characterization also provides transducer-specific quantities that are used in calculations of the interrogated material's parameters, such as the Integrated Backscatter Coefficient which will be described in detail in Chapter 5. The characterization for this research involved determining the pulse length, peak frequency, bandwidth, and minimum spatial resolution of the 15 MHz transducer used in our experiments. Each transducer has a certain focal length, which is found experimentally by using a perfect reflector. The transducer was moved closer or further away from the perfect reflector until a distance was found that maximized the amplitude of the echo. This distance is the focal length and any material that was being scanned should be at the focal length.

The peak frequency and bandwidth can be obtained from the impulse response. In order to collect the impulse response, pulse- echo ultrasound was used to emit the pulse from the transducer and collect the reflected pulse off a perfect reflector. If the transducer was in focus and aligned perpendicular to the reflector, the reflected pulse should be the exact same pulse that the transducer emitted. Figure 2.8 shows the impulse response of a 15MHz transducer. The power spectral density function can be calculated form the Fourier transform of the impulse response using equation 2.7.

$$PSD(\omega) = \frac{1}{2\pi}\left|\int_{-\infty}^{\infty} f(t)e^{i\omega t}dt\right|^2 \qquad (2.7)$$

where ω is the angular frequency (2π times the frequency) and $f(t)$ is the original signal. The minimum lateral resolution of the transducer was calculated by scanning across a thin wire. The wire was suspended in water so that it was at the focal length of the transducer. The transducer was translated from one side of the wire to the other, scanning the entire width.

Pulse- Echo ultrasound was used, so when the transducer was scanning either side of the wire, there was not a surface for the signal to reflect off so no signal was collected. When the transducer was over the wire, a signal was reflected and therefore collected. The largest amplitude signal was collected when the transducer was directly over the wire, but when the transducer was slightly to one side, a proportionally smaller amplitude signal was collected because less of the beam was reflected off the wire. The increase and decrease in reflected signal strength when scanning across a wire is known as the Point Spread Function, and is shown in Fig. 2.8 (a). Figure 2.8 (b) shows the power spectrum of the transducer. The full width at half maximum, FWHM, measurement is the minimum lateral

resolution of the transducer.

The goal of this measurement is to adequately sample the acoustic filed of the transducer with enough spatial resolution. The international Electro-technical Commission Technical Committee 87 criterion for "enough resolution" is for the maximum effective radius of the wire to be b_{max} [22]

$$b_{max} = \frac{\lambda}{4}\left[\left(\frac{l}{2a}\right)^2 + 0.25\right]^{1/2} \tag{2.8}$$

For our experiments b_{max} was calculated to be 83.12μm. The wire used for the experiments had a radius of 75 μm which lies within the criterion for enough resolution.

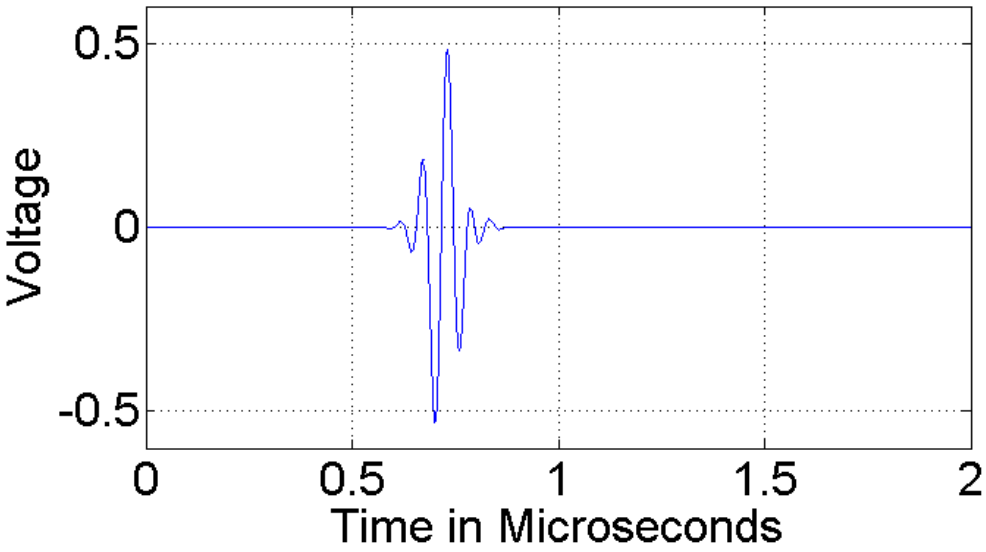

Figure 2.8: Impulse response of 15MHz transducer

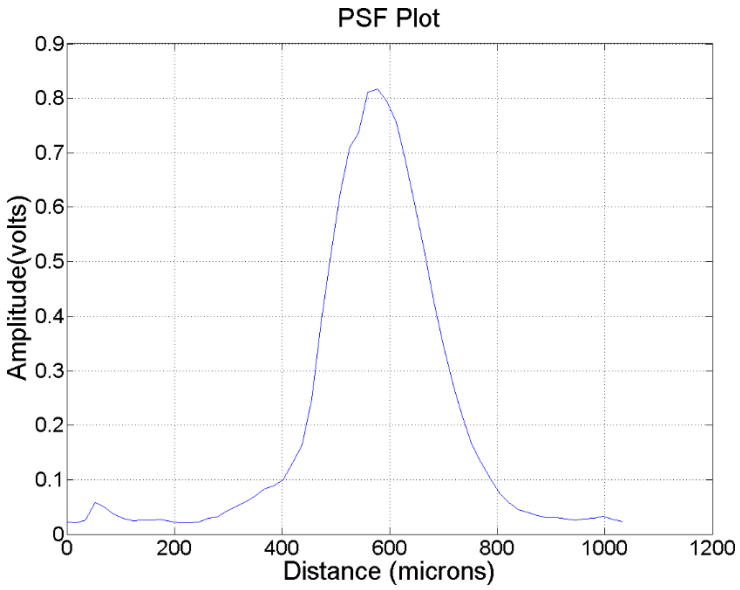

(a)

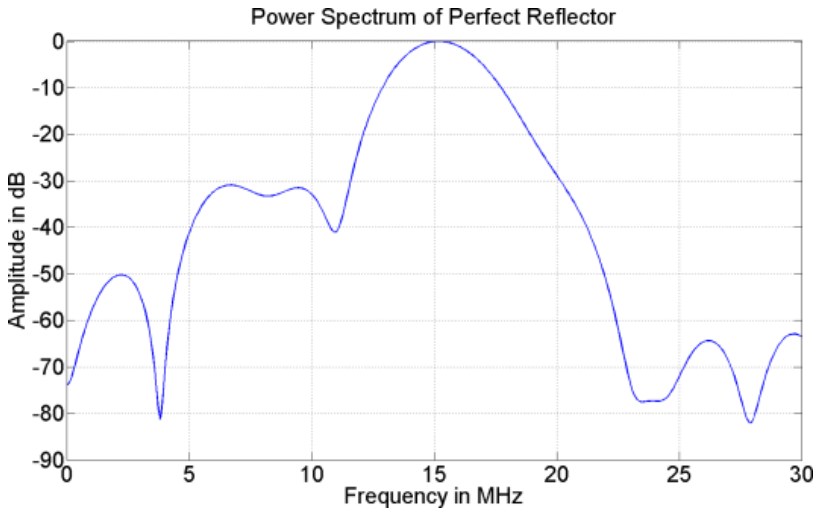

(b)

Figure 2.9 (a): PSF of 15MHz Transducer, (b): Power spectrum of 15MHz transducer

2.5 Biofilm data Acquisition

The ultrasound DAQ system described above was used to collect data from biofilm samples. A single element focused transducer (F#1.5) was fully characterized and used to study the acoustic properties of the biofilm. The transducer had a center frequency of 15MHz and a 50 percent -3dB/echo bandwidth. The lateral resolution of the transducer was calculated using the full width at half maximum (FWHM) of the PSF and was found to be 200μm. National Instrument's LabView environment was used to manage collection and analysis of the ultrasound data.

Samples were placed at the focal plane of the fully characterized 15MHz transducer and raster scans of the sample covering an area of 4000μm^2 were performed. The stepper motors were used to move the transducer with a step size of 100μm laterally.

Chapter 3

3.1 Introduction to Biofilms

Biofilms are aggregates of microorganisms in which cells adhere together on a surface with a self-produced matrix of a substance called extracellular polymeric substance (EPS). Biofilms are differentiated from freely suspended planktonic cells by the secretion of EPS. EPS accounts for 50-90% of total organic carbon in biofilms. Biofilms are very commonly found in natural, hospital and industrial settings. Construction of biofilms begins on a surface by secretion of EPS and is then followed by cell division by the bacteria encased in the biofilms up to a density of growth that can be supported by limited available nutrients. Then the bacteria stop dividing, reduce their metabolic needs and communicate with each other by a process termed "quorum sensing" to facilitate mutual survival of all the individual organisms contained within the biofilm.

Biofilms are known to be resistant to antibiotics and eradication by the immune system and thereby pose a major health problem. Biofilms have demonstrated the ability to persist in 100 to 1000 times the concentrations of antibiotics and biocides that can inhibit planktonic cells [23]. Ward *et al.* [24] showed that the immune system of a vaccinated rabbit had no effect on the growth of bacterial cells in a biofilm growing on an implanted catheter in the rabbit's body. Biofilms have been reported to attach to a wide variety of surfaces including hydrophilic and hydrophobic surfaces. There is immense value in discovering a surface that biofilms do not easily attach to since this would have implications in the development of materials used in catheters, pipes and other applications that are affected by biofilms. Unfortunately such a material has not yet been found and presently there are no available technologies to detect biofilms in vivo, or specifically to detect the maturity or bacterial

composition of a biofilms. Biofilms have been found to be responsible for a wide variety of infections in the body. Some common problems include urinary tract infections, catheter infections, middle ear infections, formation and formation of dental plaque, gingivitis and infections of permanent devices implanted in the body such as artificial joints.

3.2 Acute Otitis Media

The motivation of this research comes from biofilms associated with chronic and recurrent middle ear infections. Molecular evidence that biofilms occur in children with chronic and recurrent middle ear infections, including the strains of bacteria studied in this project, was first described by Post *et al.* and Ehrlich *et al.* [2, 25]. Otitis media is a rampant problem especially in children. Acute otitis media (AOM) is a common type of infection accompanied with symptoms such as fever, ear pain, and temporary loss or reduction in hearing. About 50% of antibiotic prescriptions given to children are for the treatment of AOM. The increasing resistance of bacteria to antibiotics makes it very important not only to diagnose the infection but also to monitor the progression or regression of the infection. The pathogenesis of otitis media involves the attachment of bacteria such as Sp and NTHi to the nasopharynx (NP). The bacteria can live in the surface of the NP for weeks to months without causing harm to the host. Then when an upper respiratory viral infection occurs the bacteria take advantage of the changes in the NP caused by the viral infection to increase in density. From the NP the organisms can gain entry to the middle ear and cause ear infections, to the sinuses and cause sinusitis, to the lungs and cause pneumonia and to the bloodstream and cause sepsis and meningitis. It is unknown whether Sp or NTHi produce biofilms in the NP and if they do whether this facilitates pathogenesis. Moreover, Sp and NTHi often co-exist in the NP and a hypothesis that the bacteria may form a multi-

species biofilms is plausible, testable and potentially of significant value to clinicians who seek methods to prevent Sp and NTHi infections.

In order to study the effects of biofilm-ultrasound interaction it is important to understand the growth cycle of biofilms.

There are five stages to biofilm development

- Initial attachment
- Irreversible attachment
- Maturation I
- Maturation II
- Dispersion

Figure 3.1 [26] shows that microbial cells are initially present in aqueous solution in suspended or "planktonic" state. If these cells find their way near a surface they have a very strong tendency to adhere to the surface. If environmental conditions in the aqueous fluid are favorable for growth (i.e. sufficient substrate and growth nutrients) then the attached cells will grow, divide and form new cells along with matrix of extracellular polymer (EPS), which binds the cells to each other and to the surface (substratum). The aggregate of cells and EPS, together with any trapped inert particles and organic matter is termed a biofilm. Products of cell metabolism and biotransformation are released back into the aqueous phase along with cells, which detach from the biofilm.

There are several important fundamental aspects of biofilm behavior. First we note that when microbial cells leave suspension and attach to a surface they may undergo a change

in their genetic expression. For example new genes are expressed which turn on the synthesis of the EPS matrix. The second very important behavior is that biofilm cells produce organic signaling compounds, which regulate biofilm behavior. This behavior is termed quorum sensing.

It is hypothesized that organic signaling compounds may be released which cause the cells to produce enzymes which dissolve the EPS matrix and detach large numbers of cells into the aqueous phase. Cell-to-cell signaling has recently been demonstrated to play a role in cell attachment and detachment from biofilms.

As the biofilm matures it is likely that many different microbial species will develop and coexist with each other. Finally, the last and likely one of the more significant observations of biofilm behavior is that biofilms, for several reasons are resistant to attack by antimicrobial agents, biocides and the human immune system. Parameters that effect the attachment and detachment of biofilms include texture, roughness or hydrophobicity of the substrate. The pH and temperature of the liquid medium the ells are suspended in also have an effect on the formation of biofilms.

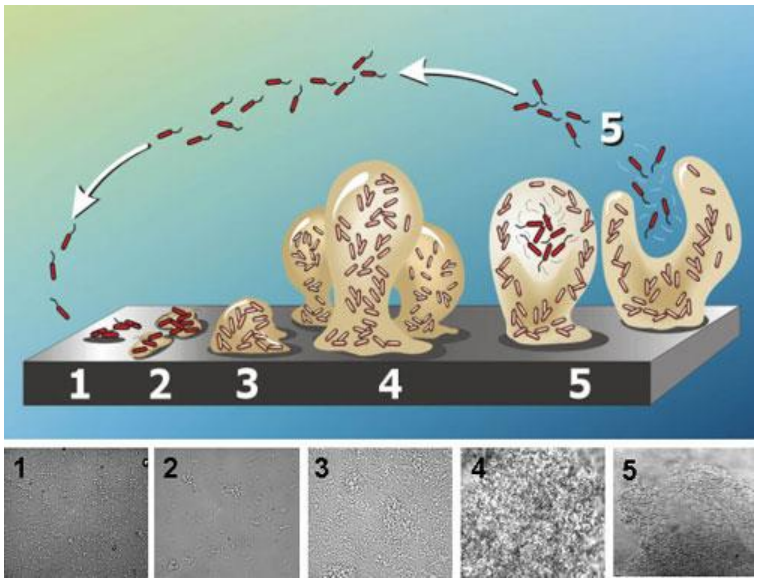

Figure 3.1: Biofilm Growth cycle and corresponding histology [26]

3.3 Biofilm sample preparations

In order to study the interaction of biofilms with ultrasound in an *in vitro* setting, samples were prepared on 6 well sterile tissue culture plates. Two different species of bacteria forming biofilms were cultured in isolation and combination to study the effects of their interaction with ultrasound. *Nontypeable Haemophilus influenzae (NTHi)* and *Streptococcus pneumonia* were chosen since these species are the most common causing infection of the middle ear.

Haemophilus influenzae, formerly called Pfeiffer's bacillus or *Bacillus influenzae*, is a Gram-negative, rod-shaped bacterium first described in 1892 by Richard Pfeiffer during an influenza pandemic. It is present in the nasopharynx of approximately 75 percent of healthy children and adults [27]. Nontypeable *H. influenzae* causes ear infections (otitis media) and sinusitis in children, and is associated with respiratory tract infections (pneumonia) in

infants, children and adults, especially those in developing countries and immunocompromised hosts [28].

S. pneumoniae was isolated in 1881 by Louis Pasteur. The species was then known as pneumococcus due to its role in the disease, pneumonia. It was termed Diplococcus pneumonia in 1926 due to its propensity to exist in pairs of cells, and renamed Streptococcus pneumoniae in 1974. *Streptococcus pneumoniae* is known to cause bacteremia, otitis media, and meningitis in humans, though it is best known for causing pneumonia, a disease of the lower respiratory tract that causes illness and death all over the world. Symptoms of pneumonia include a cough accompanied by greenish or yellow mucous, fever, chills, shortness of breath, and chest pain. The bacteria enter the body most commonly via inhalation of small water droplets and attach to the nasopharynx. Very young children and the elderly are the most prone to pneumonia [29].

The virulence factors of *S. pneumoniae* include a polysaccharide capsule that prevents phagocytosis by the host's immune cells [29], surface proteins that prevent the activation of complement (part of the immune system that helps clear pathogens from the body), and pili that enable *S. pneumoniae* to attach to epithelial cells in the upper respiratory tract [6].

Growth of 24 hour LB86-028 Nontypeable Haemophilus influenzae (NTHi) biofilms on agarose

An inoculum of a reference species of Nontypeable *Haemophilus influenzae* (NTHi), LB 86-028, was aseptically quadrant-streaked for colony isolation onto the surface of a chocolate agar plate and incubated for 24 hours at 37°C in 5% CO_2 and 10% oxygen in a Heracell 150idual gas incubator (ThermoFisher Scientific, Pittsburgh, PA) for 24 hours. Afterwards, a single isolated colony was inoculated into brain heart infusion broth

supplemented to final concentrations of 20μg/ml each for hemin and β-NAD (Sigma, St. Louis, MO) (sBHI) and incubated again for 24 hours under identical conditions. One hundred milliliters of 1% sBHI agar was prepared and 1ml was used to overlay the well bottom of a 6 well sterile tissue culture plate (Corning, Corning, New York) and allowed to solidify. Subsequently, a 1:200 dilution of the overnight culture was made into fresh sBHI broth and eight milliliters of this diluted culture was pipetted into the agarose-overlayed wells of the tissue culture plate. This culture plate was then placed into the incubator and allowed to grow for 24 hours under the same microaerophilic conditions mentioned above.

Growth of 24 hour old Streptococcus pneumoniae 02-001-V3 biofilms on agarose

A 5% sheep's blood agar plate was streaked to obtain isolated colonies of a clinical isolate of *Streptococcus pneumoniae* 02-001-V3, (Sp),obtained from the -80°C repository stocks of the Rochester General Research Institute. The plate was incubated in a Heracell 150i dual gas incubator (Fisher Scientific, Pittsburg, PA) at 37°C in 5% CO_2 and 10% oxygen for 24 hours. A single isolated colony was then inoculated into brain heart infusion broth supplemented to final concentrations of 20μg/ml each for hemin and β-NAD (Sigma, St. Louis, MO) (sBHI) and incubated for 24 hours under identical conditions. One hundred milliliters of 1% sBHI agar was prepared and 1ml was used to overlay the well bottom of a 6 well sterile tissue culture plate (Corning, Corning, New York) and allowed to solidify. Subsequently, a 1:100 dilution of the overnight culture was made into fresh sBHI broth and eight milliliters of this diluted culture was pipetted into the agarose-overlaid wells of the tissue culture plate. This culture plate was then placed into the incubator and allowed to grow for 24 hours under the same microaerophilic conditions mentioned above.

Growth of 24 hour combined LB86-028 NTHi and Streptococcus pneumoniae 02-001-V3 biofilms on agarose

Simultaneous growth of LB86-028 NTHi and *Streptococcus pneumoniae* 02-001-V3, (NTHi+Sp) biofilm was accomplished by mixing equal volumes of respectively 1:200 and 1:100 dilutions of separate 24 hr sBHI cultures of LB86-028 NTHi and *Streptococcus pneumoniae* 02-001-V3 into fresh sBHI, and incubating for 24 hours in a Heracell 150i dual gas incubator (Fisher Scientific, Pittsburg, PA) at 37°C in 5% CO_2 and 10% oxygen. One hundred milliliters of 1% sBHI agar was prepared and 1ml was used to overlay the well bottom of a 6 well sterile tissue culture plate (Corning, Corning, New York) and allowed to solidify. Subsequently, eight milliliters of the combined culture mixture was pipetted into the agarose-overlayed wells of the tissue culture plate. This culture plate was then placed into the incubator and allowed to grow for 24 hours under the same microaerophilic conditions mentioned above.

Growth of 4 day old individual biofilms of LB86-028 and Streptococcus pneumoniae 02-001-V3 and combined LB86-028 /Streptococcus pneumoniae biofilms on agarose

Growth of the individual species and the combined species biofilms on 1% agarose was accomplished by respectively following the procedures outlined above with the exception of the incubation time being increased from 24 hours to 4 days.

Chapter 4

4.1 Challenges in Biofilm studies

There are several challenges in using ultrasound as a modality to study biological materials which do not produce strong echoes. In order to analyze the acoustic properties of biofilms a valid signal needs to be detected. Typically the ultrasound signal reflected from the biofilm is weak and very close to the noise level of the system, this sometimes causes it to be embedded within the noise and become undetectable to the post processing algorithms. The other problem is the axial resolution of the transducer used, which may not be enough to resolve the biofilm and the surface they grow on making it hard to isolate the signal exclusively from the biofilm. Typically there is interference between the signal corresponding to the biofilm and that corresponding to the surface they are growing on. As a result of this the accuracy of all subsequent measurements is hampered. Therefore the two major problems that needed to be addressed for analysis were:

- Isolating the biofilm signal from that corresponding to the substrate
- Improving the signal to noise ratio (SNR)

In order to isolate the biofilm signal from that of the substrate, the biofilms were grown on a layer of agarose thick enough to allow the axial resolution of the system to produce two separate features corresponding to the biofilm and the surface of the bottom of the tissue culture well they grew on. The acoustic impedance of agarose is very closely matched to that of water and the layer of agarose does not produce a detectable echo by itself. The purpose of the layer of agarose is to elevate the biofilm from the bottom surface of the dish well. Figure 4.1 shows the effect of the layer of agarose on the A-scan plot. With the biofilm

signal separated from the surface of the well, all the characterization was performed on the segmented signal corresponding to the biofilm.

In order to improve the SNR which is critical for the accuracy of the analysis two separate approaches independent of each other were considered to denoise the raw RF echo from the biofilm samples. Frequency modulated chirp sequences were designed and used to drive the transducer as opposed to a conventional pulse used for data acquisition. The RF echo pulse received were then compressed to restore axial resolution using a matched filter or a wiener filter. This method has been proven to provide significant improvement in SNR as demonstrated by Venkatraman *et al.* [30]. The possibility of using this method to achieve better SNR in our experimental setup was investigated. Section 4.3 describes the theory behind this method and the reason behind not choosing to use it to improve SNR.

Another completely different approach to denoise RF data is the use of the wavelet transform. Section 4.4 describes the wavelet denoising method and the results of using it on our datasets.

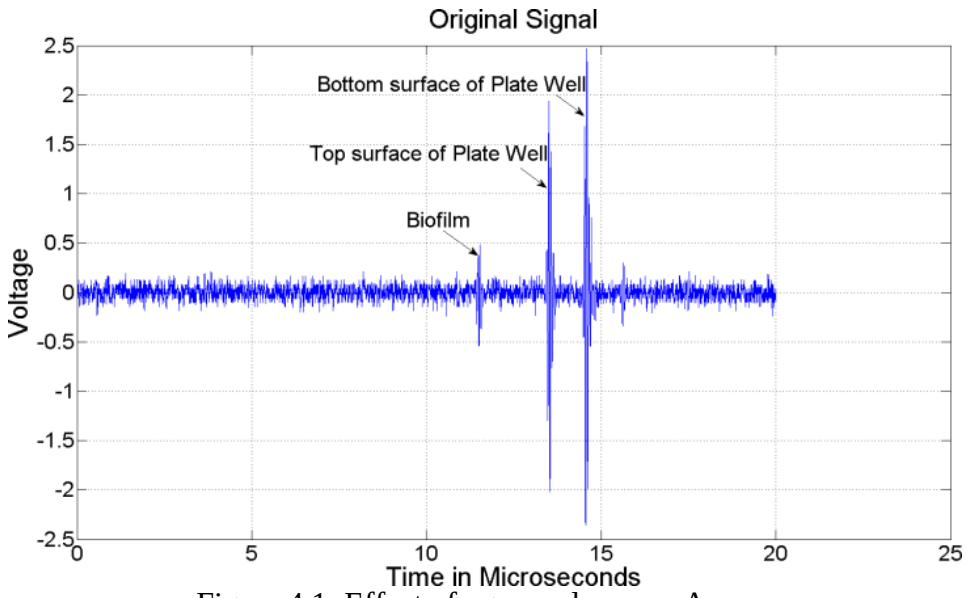

Figure 4.1: Effect of agarose layer on A-scan

4.2 Independent A-line analysis

Another factor that hampers accuracy of the post processing characterization algorithms is the correlation between adjacent A-lines. The 15MHz transducer has a PSF that was experimentally determined to be around 200µm. This lateral resolution of the transducer puts a limit on the number of A-lines within an acquisition that are independent of each other. The RF data acquired consists of reflections from adjacent scan lines which fall within the spatial confines of this limit and therefore hold redundant information. Applying post processing on the entire dataset is also a computationally expensive task. Liu and Zagzebski [16] performed studies to determine the number of independent A-lines by measuring the correlation between adjacent A-lines. The idea is to avoid redundancy in the data. A similar method was used to calculate the number of independent A-lines from a 15MHz transducer. Equation 4.1 was used to determine the correlation between the adjacent A-lines.

$$\rho_{xy} = \frac{\sum(x_i - x)(y_i - y)}{\sqrt{\sum(x_i - x)^2\ (y_i - y)^2}} \tag{4.1}$$

where x_i and y_i are RF echo signal values for A-lines x and y at axial position i and x and y are the sample mean values within the sub region. The correlation coefficients between segments A-lines 1 and 2, 2 and 3, and so on were averaged to get the covariance between adjacent A-lines. The correlation coefficients between segments 1 and 3, 2 and 4, and so on were averaged to get the correlation between every other A-line. The results were then averaged over all B-mode acquisitions in the entire data set to give ρ_m. The following equation was used to calculate the number of independent A-lines using Equation 4.2 [31]

$$N_{eff} = N(1 + \frac{2}{N}\sum_{m=1}^{N-1}((N - m)\rho_m^2)^{-1} \tag{4.2}$$

where N is the total number of A-lines within an ROI, m is the A-line separation in the units of the pitch of the A-line and ρ is the correlation coefficient. The number of independent A-lines was calculated at the focal depth of the 15MHz transducer using the aforementioned equation. We reported 10 independent A-lines within an ROI comprising of 40 A-lines. This was taken into consideration before choosing the A-lines that were subject to the post processing. Independent A-line analysis makes post processing computationally less expensive. In the dataset collected which comprised of 1600 A-lines only 100 A-lines are used for post processing.

4.3 SNR improvement via Coded excitation and pulse compression

Coded excitation and pulse compression was first used in radar to improve SNR [32]. The same fundamental idea has been used in ultrasound imaging to improve SNR. The improvement in SNR is brought about by targeting the sample to be imaged with a

frequency encoded chirp signal which pumps more energy into bands of frequency that usually have low SNR by virtue of its larger time bandwidth product as compared to a conventional pulse. Pulse compression algorithms are used to compress the echo RF signal to produce a signal which has an improved SNR. The technique helps prevent bio-effects as opposed to simply amplifying the waveform used to insonify the target. Designing the frequency encoded chirp is crucial for improvement in SNR. Oelze *et al.* [33] demonstrated a resolution enhancement technique that allows a desired increase in bandwidth as compared to the technique used by Venkatraman *et al.* [30] which allows a 40-50% increase in bandwidth. A technique similar to the one demonstrated in [33] was used for SNR improvement.

4.3.1 Theory

Consider an ultrasonic system with an impulse response, $h(nT, x)$. The randomly scattered object is represented by f(x). The echo measured with the source is given by the following equation.

$$g(n) = \int_{-\infty}^{\infty} h(nT, x) f(x) dx + e(n) \tag{4.3}$$

Where $e(n)$ is the signal independent noise that is a wide sense stationary random process. The impulse response of the system can be defined as the convolution of the impulse response of the transducer and the voltage waveform used to excite the source.

$$h(nT, x) = \sum_{m=-\infty}^{m=\infty} v_1[n-m] h_1(mT, x) = \{v_1 * h_1\}(mT, x) \tag{4.4}$$

where, $v_1[n]$ is the voltage waveform. The impulse response of the imaging system is not unique to a particular pulse-echo impulse response of the transducer. It is possible to design a new impulse response of a system $h_2[nT, x]$ that when convolved with a different voltage waveform $v_2[n]$ is equivalent to $h(nT, x)$.

$$\{v_1 * h_1\}(mT, x) = \{v_2 * h_2\}(mT, x) \tag{4.5}$$

Suppose the voltage waveform used to excite the source with impulse response is given by a frequency-modulated chirp.

$$v_{lin}[n] = exp\left\{i2\pi\left(f_0 nT + \frac{\Delta f}{T_P}(nT)^2\right)\right\} \tag{4.6}$$

A different FM chirp v_{pchirp} can be used to excite the source with impulse response $h_1[nT, x]$ such that:

$$v_{pchirp} * h_1(nT, x) = v_{lin} * h_2(nT, x) \tag{4.7}$$

In frequency domain

$$V_{pchirp} \,.\, H_1(u, x) = V_{lin} \,.\, H_2(u, x) \tag{4.8}$$

$$V_{pchirp} = \frac{V_{lin} \,.\, H_2(u, x)}{H_1(u, x)} \tag{4.9}$$

After transmission the echo received needs to be compressed by the use of appropriate filters to reduce the correlation length of the received echo signals. Based on equation 4.7 it is possible to choose appropriate filters so that they are equal to an alternate impulse response $h_2(nT, x)$. This alternate impulse response can be artificially created such that it is useful to the imaging system. Example: A -3dB bandwidth which is significantly larger than the true impulse response. Pulse compression can be achieved by the following equation

$$g[n] = \sum_{m=-\infty}^{m=\infty} b[m-n]g'[m] \tag{4.10}$$

Where b[n] is some filtering function. If b[n] is chosen such that $b[n] = v_{lin}^{-1}[n]$ then the equation becomes

$$g[n] = \sum_{m=-\infty}^{m=\infty} v_{lin}^{-1}[n]\, g'[m] \tag{4.11}$$

$$= \sum_{m=-\infty}^{m=\infty} v_{lin}^{-1}[n] \int_{m=-\infty}^{m=-\infty} h(mT, x).f(x)\, dx + e[n] \tag{4.12}$$

Where e[n] is the noise. Based on convolution equivalence the equation becomes

$$g[n] = \sum_{m=-\infty}^{m=\infty} v_{lin}^{-1}[m-n] \int_{-\infty}^{\infty} \sum_{l=-\infty}^{l=\infty} v_{pchirp}[m-l]h_1(lT, x).f(x)dx + e[n]$$

$$g[n] = \sum_{m=-\infty}^{m=\infty} v_{lin}^{-1}[m-n] \int_{-\infty}^{\infty} \sum_{l=-\infty}^{l=\infty} v_{lin}[m-l]h_2(lT, x).f(x)dx + e[n] \tag{4.13}$$

$$g[n] = \sum_{m=-\infty}^{m=\infty} K\delta[l-n] \int_{-\infty}^{\infty} h_2(lT, x).f(X)dx + e[n]$$

Where K is the time bandwidth product of $v_{lin}[n]$

The equation proves that the echo depends on the interaction of the impulse response $h_2(nT, x)$ with the scattering object as opposed to $h_1(nT, x)$. The improvement in SNR is demonstrated by the following equations

$$eSNR[n] = 10\, log\left(\frac{E\left\{\left|K\int_{-\infty}^{\infty} h_2(nT, x)f(x)dx\right|^2\right\}}{E\{|e(n)|^2\}}\right) \tag{4.14}$$

$$= 10\, log\left(\frac{K^2\sigma_f^2}{K\sigma_e^2}\int_{-\infty}^{\infty} h_2(nT, x)dx\right)$$

$$= 10\ logK + eSNR'[n]$$

Equation 4.14 shows that the increase in SNR for the pulse compression is larger than the $eSNR'$ by $10\ logK$.

4.3.2 Pulse compression

The received echo needs to be compressed to restore the correlation length of the signal. Compression can be achieved by a matched filter via convolution with a time reversed FM chirp $v_{lin-chirp}[-n]$ using the following equation:

$$f[n] = \sum_{l=-\infty}^{\infty} v_{lin-chirp}[l-n]\ \ g'[n] \tag{4.15}$$

Matched filters are used in high noise environments to minimize noise amplifications. Matched filter decoding yields the highest eSNR at the cost of smaller bandwidth and higher range side lobes. Side lobes are of concern when the signal is being used to produce images because the side lobes give false impressions of structures which can lead to incorrect diagnosis. Since our data is not being used to form images the side lobes are not very critical for the accuracy of post processing. Another filtering approach used to control the range of side lobes and yield better bandwidth is Wiener filtering. Wiener filters are used to address noise problems inherent in de-convolution. A frequency domain representation of a Wiener filter is shown below:

$$\beta_{wiener}(u) = \frac{V_{lin}^{*}(u)}{|V_{lin}(u)|^2 + \gamma_w \overline{eSNR}^{-1}(u)} \tag{4.16}$$

where, $\overline{eSNR(u)} = \frac{|H_2(u)|E\{|F(u)|^2\}}{E\{|N(u)|^2\}}$ and γ_w is a regularization constant.

Wiener filter requires some prior statistical information about the signal to be reconstructed. The noise spectrum can be experimentally obtained.

Pulse compression via Wiener filtering is obtained using the following equation:

$$F_{comp}(u) = \beta_{wiener}(u) \, . G(u)$$

$$f(nT, x) = \boldsymbol{\mathcal{F}}^{-1}(F_{comp}(u)) \quad (4.17)$$

where $F_{comp}(u)$ is the compressed echo and $\boldsymbol{\mathcal{F}}^{-1}$ represent the inverse Fourier transform. The advantage the wiener filter has over matched filtering is the suppression of side lobes. For low noise echo waveforms the first term in the denominator of equation 4.16 dominates the second the filter behaves like an inverse filter. In high noise conditions the magnitude of the second term is higher and the filter behaves like a matched filter. The challenge in implementing a Wiener filter is estimating the FT of the noise free signal and adjusting the regularization constant.

4.3.3 Experimental Implementation

The pre-enhanced chirp signals were generated with Matlab 2012b (Mathworks, Natick, MA) and downloaded to an arbitrary waveform generator (Tektronix AWG600, Beaverton, OR). The signal from the generator was amplified using a 2100L RF power amplifier (ENI, Rochester, NY). The amplified signal was then connected to a diplexer. The received echo signal was displayed on an oscilloscope, which also serves as an analog to digital converter. Figure 4.2 is a diagram of the entire setup.

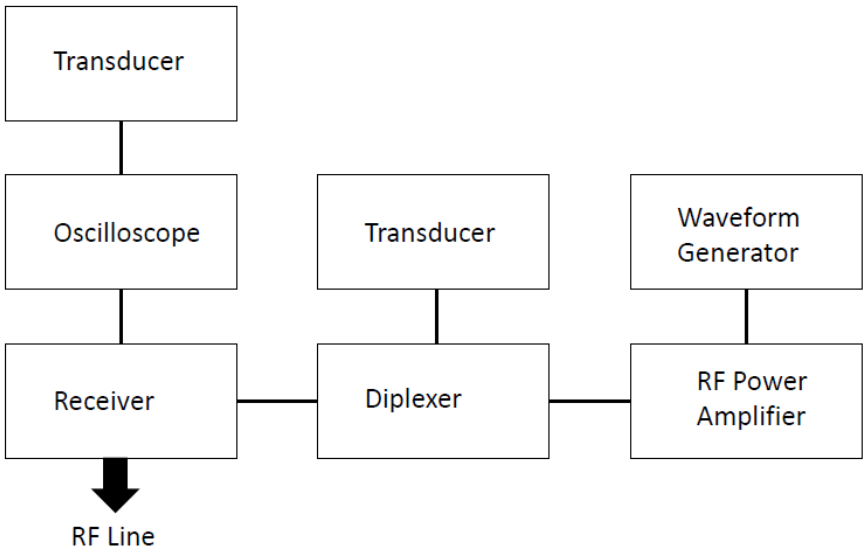

Figure 4.2: Experimental Setup

The pre-enhanced chirp used in experiments was first designed for a 15MHz transducer based on the theory described in the previous section. The pulse compression algorithms could not consistently pick up a signal that corresponded to the biofilm from the echo. The equipment used which includes the pulser/receiver has a frequency response which rolls off in the range of frequencies used to drive the transducer. The close proximity of the biofilm to the bottom of the well also placed a limitation on the temporal length of the chirp sequence further limiting the improvement in SNR which is dependent on the time bandwidth product of the signal. Due to the inability of this approach to consistently recover the echo from the biofilm this method was not used for SNR improvement as a part of the protocol. However, attempts to implement this algorithm using a 3.5MHz transducer were successful on a more consistent basis as compared to the higher frequency. A linear chirp was designed based on equation 4.6 with a center frequency of 3.5MHz and bandwidth of 1MHz. The pre enhanced chirp was designed based on equation 4.9. The impulse response of the 3.5MHz transducer was experimentally obtained and the desired

impulse response with a 100% -3dB bandwidth was designed by placing a Hamming window on the true impulse response and taking the Fourier transform of the result. Figure 4.3 shows the linear chirp that sweeps the frequency range of the transducer. The pre-enhanced chirp shown in Figure 4.4 generated using the function generator drove the 3.5MHz transducer. Figure 4.5 shows the spectrum of the impulse response of the transducer and the modified impulse transducer. The echo after transmission of the pre enhanced chirp is shown in Figure 4.6 and the compressed pulse after matched filtering is shown in Figure 4.7. The wiener filter suppresses the side lobes of the reconstructed signal. Since the data is not being used for imaging but for analysis this improvement does not justify the use of this method and therefore matched filtering was used to bring about the improvement in SNR.

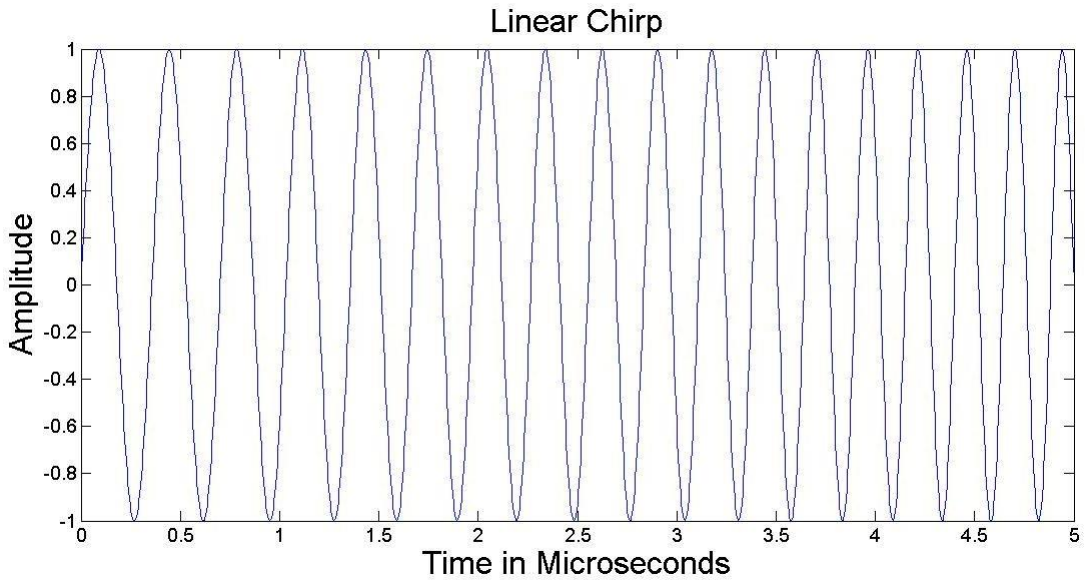

Figure 4.3: Linear Chirp

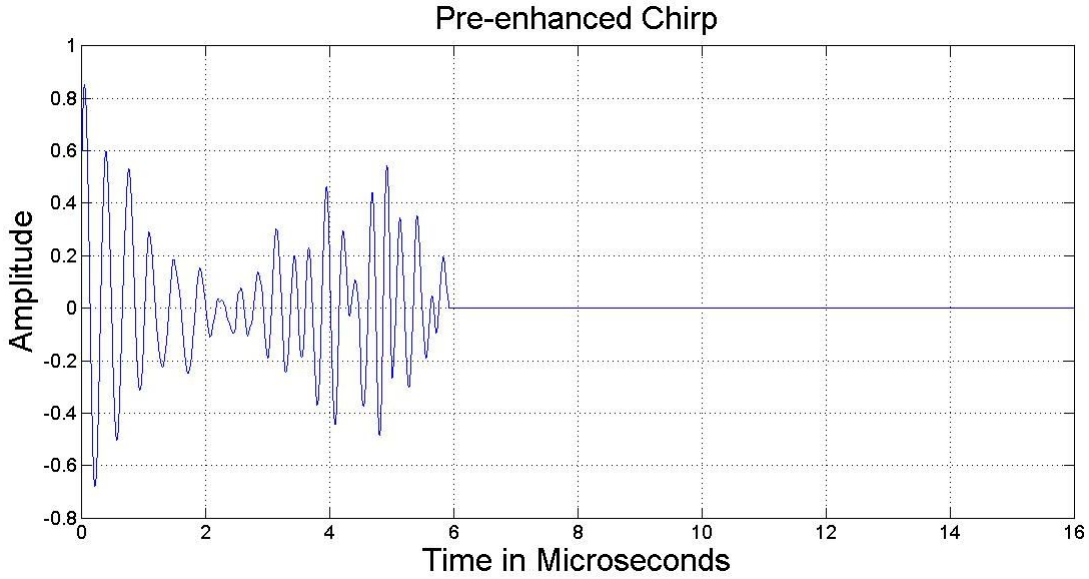

Figure 4.4: Pre-enhanced Chirp

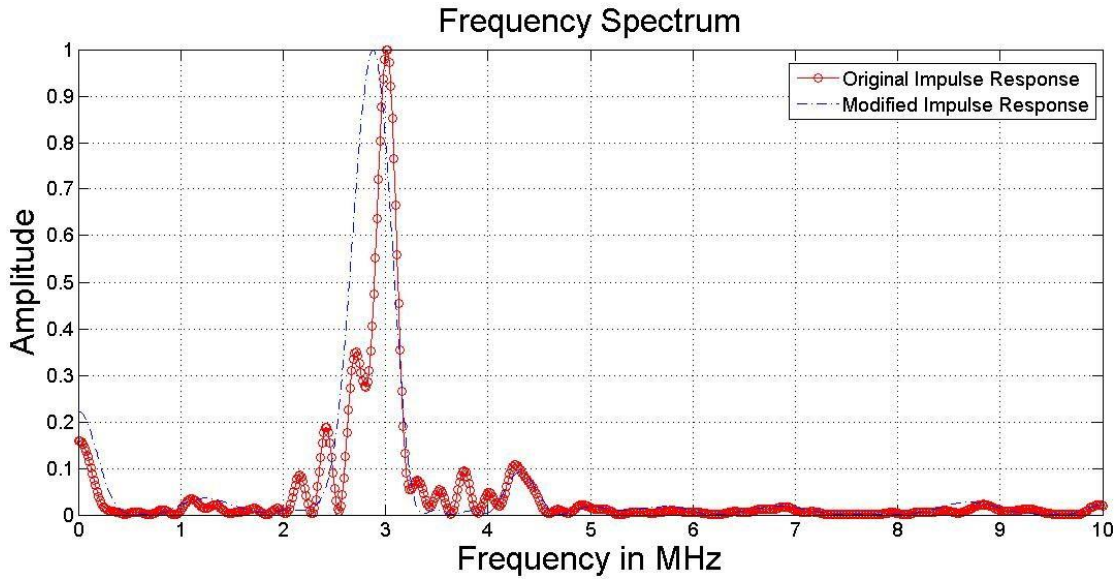

Figure 4.5: Spectrum of Original and Modified Pulse

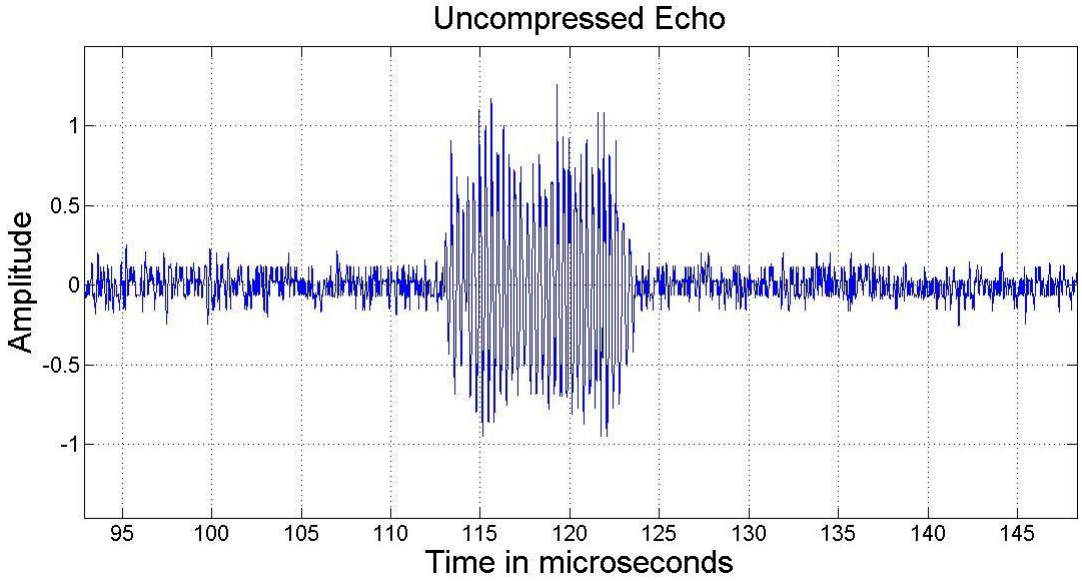

Figure 4.6: Uncompressed echo after transmission of Pre-enhanced chirp

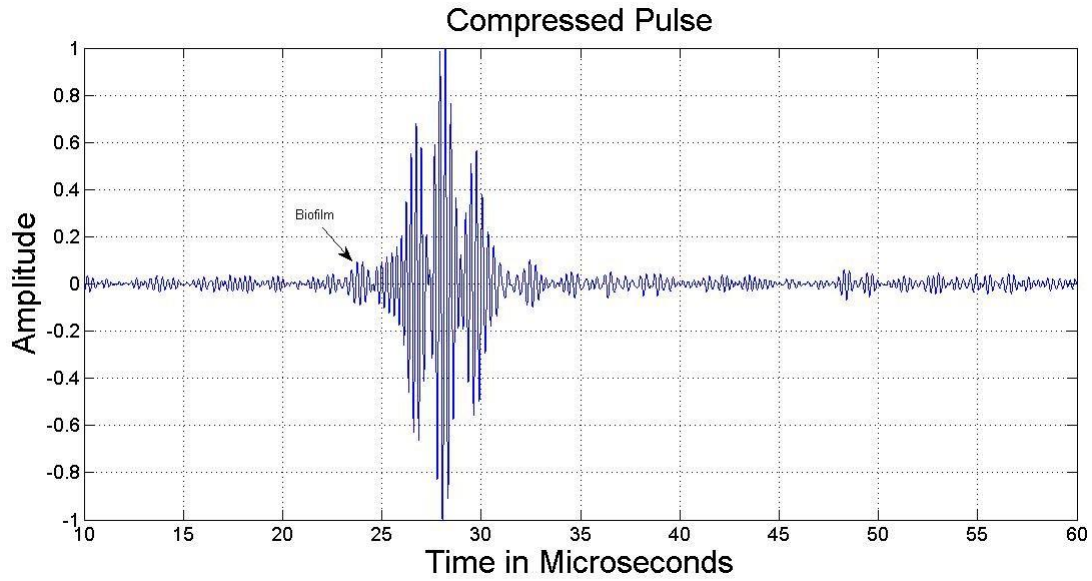

Figure 4.7: Compressed pulse post matched filtering

4.4 SNR improvement via Wavelet based denoising scheme

Due to the inability of the encoded chirp and pulse compression technique to produce a dataset that could be used for characterization, wavelet transform-based denoising was used to bring about an improvement in the SNR.

Fourier transform-based spectral analysis is the dominant analytical tool for frequency domain analysis. However, the Fourier transform cannot provide any information of the spectrum changes with respect to time. The Fourier transform assumes the signal is stationary, but ultrasound signals are always non-stationary. To overcome this deficiency, a modified method, the short time Fourier transform allows to represent the signal in both time and frequency domain through a time windowing function [34]. The Fourier transform is applied to the windowed component of the signal. The window length determines a constant time and frequency resolution. According to Heisenberg's uncertainty principle the exact temporal location of frequency components in the signal cannot be known. Therefore choosing a narrower temporal window results in poor frequency resolution and vice versa. The limiting case of the short term Fourier transform is choosing a window of infinite temporal length where the short term Fourier transform becomes the Fourier transform. The short term Fourier transform only allows a fixed window size, which results in constant time and frequency resolution. The wavelet transform allows variable window sizes provide a more dynamic view of the signal at different time and frequency resolutions.

4.4.1 Wavelet Fundamentals

A continuous-time wavelet transform of *f (t)* is defined as:

$$CWT_{\psi}f(a,b) = |a^{-\frac{1}{2}}| \int_{-\infty}^{\infty} f(t)\psi^{*} \frac{t-b}{a} dt \qquad (4.18)$$

Here a, $b \in R$, $u \neq 0$ are the dilating and translating coefficients, respectively. The asterisk denotes a complex conjugate. This multiplication of $|a^{-\frac{1}{2}}|$ is for energy normalization purposes so that the transformed signal will have the same energy at every scale. The

analysis function $\psi(t)$, the so-called mother wavelet, is scaled by *u*, so a wavelet analysis is often called a time-scale analysis rather than a time-frequency analysis. The wavelet transform decomposes the signal into different scales with different levels of resolution by dilating a single prototype function, the mother wavelet.

4.4.2 Discrete Wavelet Transform

One drawback of the CWT is that the representation of the signal is often redundant, since *a* and *b* are continuous over *R* (the real number). The original signal can be completely reconstructed by a sampled version of $W_f(a,b)$. Typically, we sample $W_f(a,b)$ in dyadic grid, i.e.,

$$a = 2^{-m} \text{ and } b = n\,2^{-m} \tag{4.19}$$

$m, n \in Z$, and Z is the set of positive integers. Substituting (4.19) into (4.18), we have

$$DWT_\psi f(m,n) = \int_{-\infty}^{\infty} f(t)\psi_{m,n}^*(t)dt \tag{4.20}$$

where $\psi_{m,n}^* = 2^{-m}\psi(2^{-m}t - n)$ is called a dilated and translated version of the mother wavelet $\psi(t)$.

The family of dilated mother wavelets of selected *a* and *b* constitutes an orthonormal basis of $L^2(R)$. In addition $W_f(a,b)$ is sampled in dyadic grid; this wavelet transform is also called dyadic-orthonormal wavelet transform. Due to the orthonormal properties, there is no information redundancy in the discrete wavelet transform. In addition, with this choice of *a* and *b*, there exists the multi-resolution analysis (MRA) algorithm, which decompose a signal into scales with different time and frequency resolution. MRA is designed to give

good time resolution and poor frequency resolution at high frequencies and good frequency resolution and poor time resolution at low frequencies.

The fundamental concept involved in MRA is to find the average features and the details of the signal via scalar products with scaling signals and wavelets. In the ultrasound signals typically features of interest are observed as spikes. The spikes are typically of high frequency and we are able to discriminate spikes from other noise sources through the decomposition of MRA into different levels. The differences between different mother wavelet functions (e.g. Haar, Daubechies, Coiflets, Symlet, Biorthogonal and etc.) consist in how these scaling signals and the wavelets are defined. The choice of wavelet determines the final waveform shape. To have a unique reconstructed signal from wavelet transform, we need to select the orthogonal wavelets to perform the transforms.

The wavelet decomposition results in levels of approximated and detailed coefficients. The algorithm of wavelet signal decomposition is illustrated in Figure 4.8. Reconstruction of the signal from the wavelet transform and post processing, the algorithm is shown in Figure 4.9. This multi-resolution analysis enables us to analyze the signal in different frequency bands; therefore, we could observe any transient in time domain as well as in frequency domain.

The relation between the loss-pass and high-pass filter and the scaling function $\psi(t)$ and the wavelet $\phi(t)$ can be stated as:

$$\phi(t) = \sum_k h[k]\phi[2t-k] \tag{4.21}$$

$$\psi(t) = \sum_k g[k]\phi[2t-k] \tag{4.22}$$

where g[k] is the high pass filter and h[k] is the low pass filter. The filtering and the down sampling operation can be expressed as:

$$A^k = \sum_n A^{i-1}(t) \,.\, h[2k - n] \tag{4.23}$$

$$D^j = \sum_n A^{i-1}(t) \,.\, g[2k - n] \tag{4.24}$$

The above procedure is reversed for reconstruction of the signal. The signal at each level is up sampled by two and passed through the synthesis filters $g'[n]$, and $h'[n]$ and then added. The analysis and synthesis filters are identical except for time reversal. Therefore the reconstruction formula for each layer becomes:

$$A^t = \sum_{k=-\infty}^{\infty} (D^{i-1}[k].\, g[-n + 2k] + A^{i-1}[k].\, h[-n + 2k]) \tag{4.25}$$

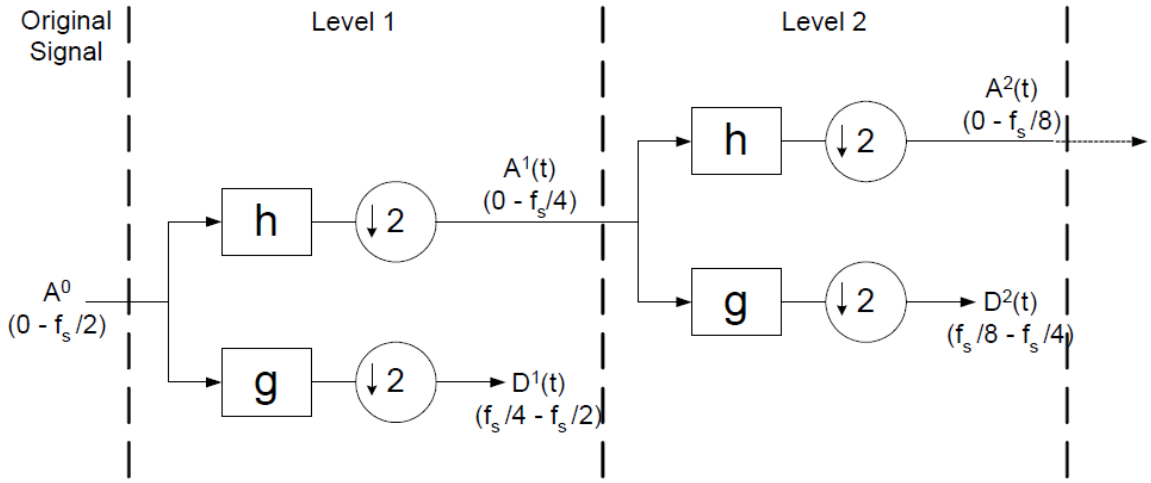

Figure 4.8: Analysis Scheme

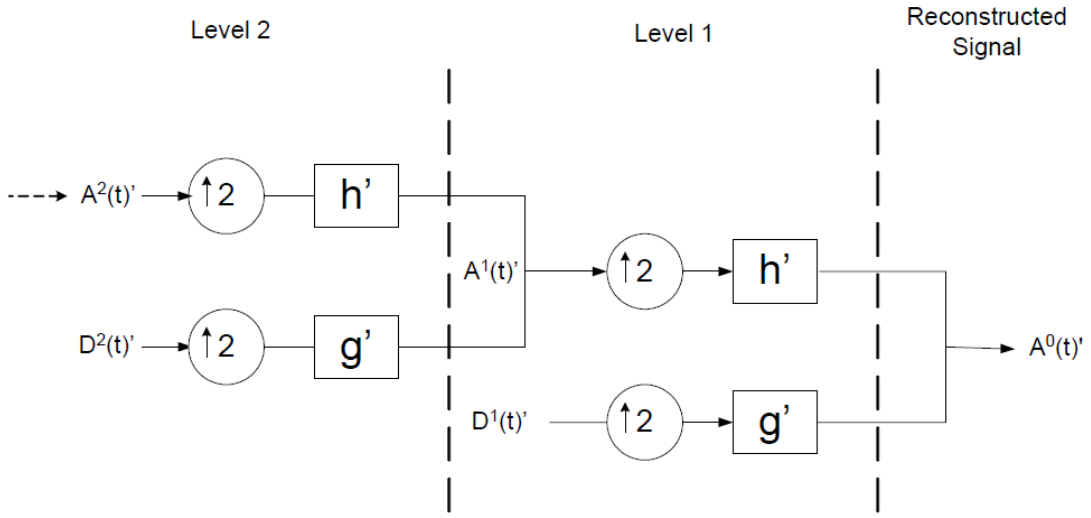

Figure 4.9: Synthesis Scheme

The general wavelet denoising procedure is as follows [35]:

- Apply wavelet transform to the noisy signal to produce the noisy wavelet coefficients to the level.
- Select appropriate threshold limit at each level and threshold method (hard or soft thresholding) to best remove the noises.
- Inverse wavelet transform of the thresholded wavelet coefficients to obtain a denoised signal.

4.4.3 Wavelet denoising of ultrasound signal

Since the ultrasound signal reflected from the biofilm is weak and very close to the noise level of the system, this sometimes causes it to be embedded within the noise and become undetectable to the post processing algorithms. As a result of this the accuracy of all subsequent measurements is hampered. A wavelet decomposition scheme as

described above was utilized to solve this problem. All software was developed in Matlab using the Uvi_Wave toolbox [36].

The idea behind the wavelet-denoising scheme lies in the ability of the algorithm to break the signal to be denoised into several spectral bands with the use of low and high pass filters [37]. The one-dimensional wavelet transform generates a vector of wavelet coefficients representing the signal at different bands of frequencies. The coefficients representing the noise have a lower value as compared to those representing the signal. The advantage of the wavelet scheme is that it is very good at preserving natural features even if they appear to be close to the noise level of the system because it takes advantage of the fact that the noise is randomly distributed and the features are not. The energy of the signal is collected in fewer coefficients as we go down in the levels. Energy is conserved since we used orthogonal filters. Consequently, these coefficients become larger and due to the randomly distributed nature of noise the coefficients must stay evenly distributed and thereby be small in magnitude. It is therefore reasonable to denoise the signal by setting the small coefficients to zero. Preserving the coefficients that represent the signal and replacing the ones that represent noise by zero we can reconstruct the original signal in the temporal domain by using the inverse wavelet transform. Orthogonal symlet filters were used therefore the transform used here preserves energy. Symlet filters were also used because they match the shape of the impulse response of the transducer. The thresholding of coefficients was done on the 6^{th} or the 7^{th} level of decomposition depending on the sampling rate. A threshold of 1.5 was used before inverting the transform. Conditioning the signal using this wavelet scheme improves accuracy of all subsequent processing. Every A-line that was used

for spectral estimations was first denoised using this scheme. Figure 4.10(a) shows the original signal. Figure 4.10(b) the histogram of the coefficients from which it is evident that most of the coefficients centered around zero are low in magnitude and represent noise. The coefficients to the far right in the plot are the ones that represent the signal. Figure 4.10(c) shows the denoised signal with the preserved features. Figure 4.10 (d) shows the detail and approximation plots of the signal at all levels of decomposition. Wavelet denoising increased SNR by 40%. The SNR was calculated using equation 4.26.

$$SNR \cong 10 \log \left(\frac{\sigma_{sig}^2}{\sigma_n^2} - 1 \right) \tag{4.26}$$

where σ_{sig}^2, is the variance of the signal within a window of predefined size and σ_n^2 was the variance of the noise within a window of the same size in a region of the A-line away from the feature. The procedure was repeated over all independent A-lines and the results were averages.

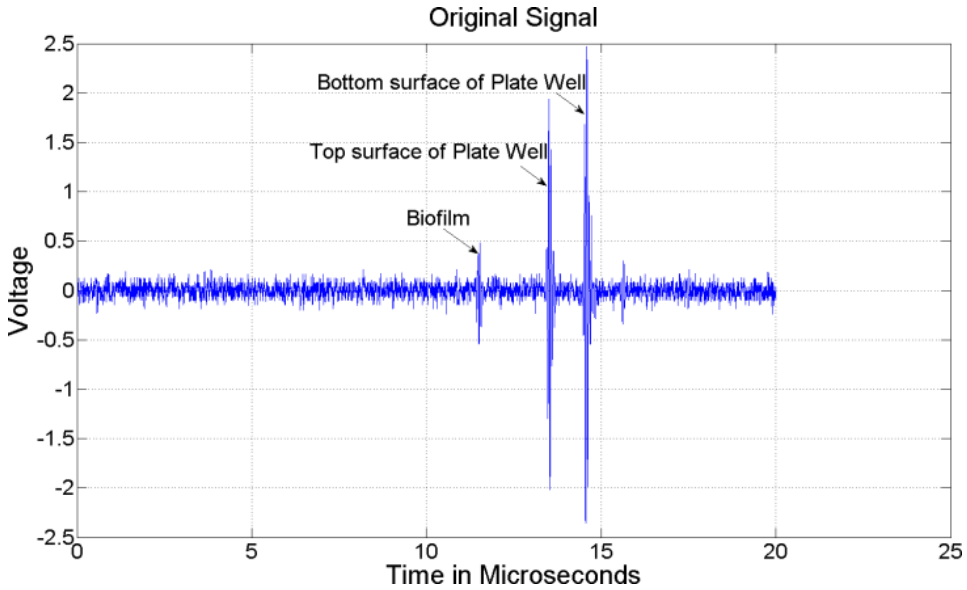

(a)

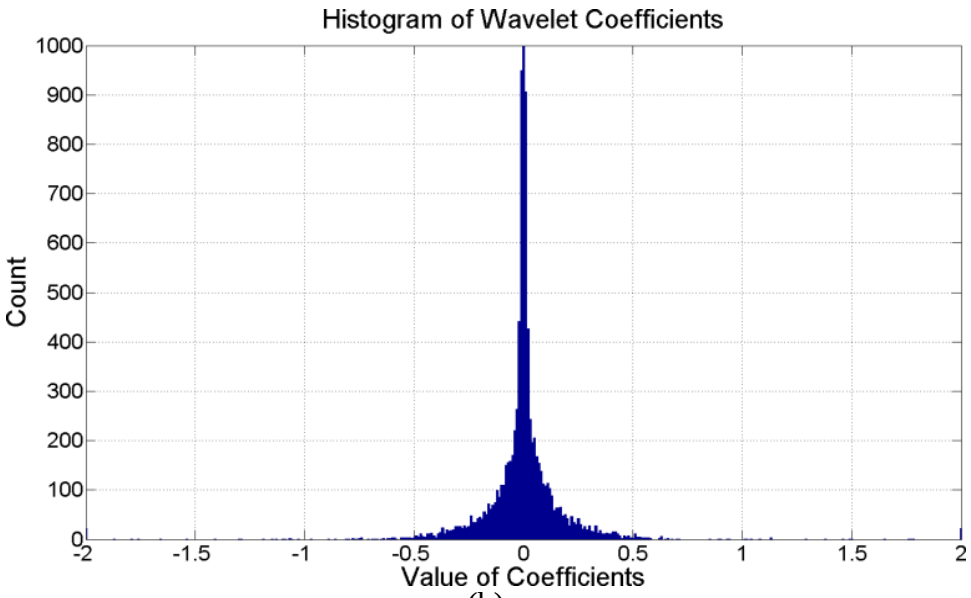
Histogram of Wavelet Coefficients
Count
Value of Coefficients
1000
900
800
700
600
500
400
300
200
100
0
-2
-1.5
-1
-0.5
0
0.5
1
1.5
2

(b)

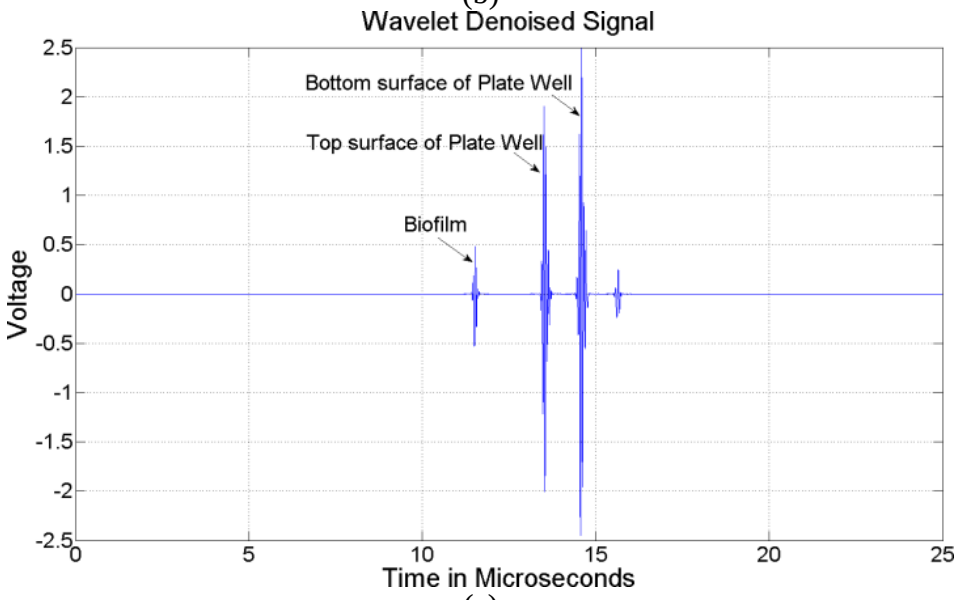
Wavelet Denoised Signal
Bottom surface of Plate Well
Top surface of Plate Well
Biofilm
Voltage
Time in Microseconds
2.5
2
1.5
1
0.5
0
-0.5
-1
-1.5
-2
-2.5
0
5
10
15
20
25

(c)

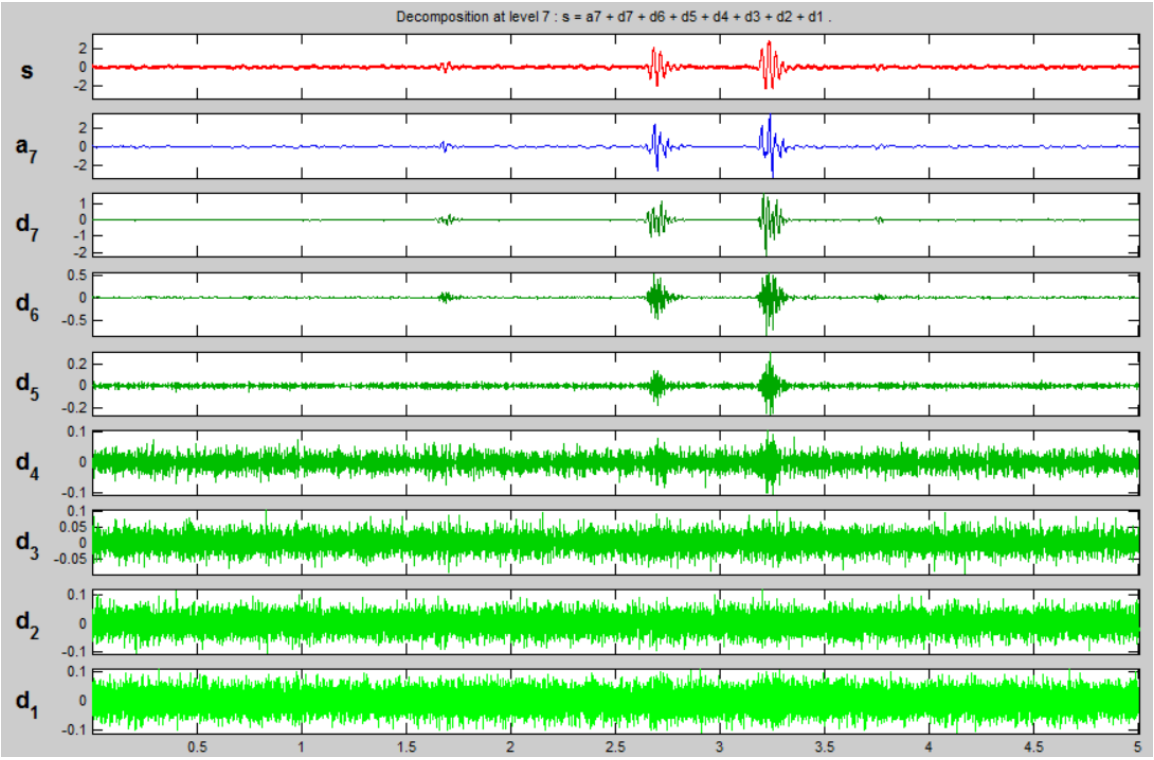

(d).

Figure 4.10: (a) Raw A-line. (b) Histogram of wavelet coefficients showing that low-value coefficients are predominant. (c) Denoised signal identifying returns. (d) Wavelet decomposition showing detail and approximation waveforms

4.5 Conclusion

Since the coded chirp technique could not be implemented at 15MHz, the technique was not used as standard protocol to denoise RF data and was presented as a proof of concept. The wavelet denoising method worked reliably at 15MHz and provided reasonable improvement in SNR and was preferred over the FM chirp technique. The wavelet denoising technique is a post processing technique and the results can be modified without reacquiring data. This is not the case with the chirp excitation technique which requires the data to be acquired in a specific way without which the technique cannot be used to bring about an improvement in the SNR.

Segmentation of the RF signal corresponding to the biofilm and the SNR improvement brought about by the wavelet denoising scheme is critical for the accuracy of the results based on metrics described in Chapter 5. RF lines that have been subjected to the independent A-line analysis and have undergone wavelet denoising are used for subsequent analysis based on the metrics defined in the next chapter.

Chapter 5

5.1 Quantitative Analysis and Characterization

The science of ultrasonic tissue characterization is the untangling of hidden patterns in pulse-echo data to extract more information about tissue function and pathology than that seen in conventional images [38] . The characterization carried out in this thesis was based on the frequency content of the RF data acquired.

Wavelet denoised independent A-lines were selected based on the procedures described in Chapter 4. The preprocessed data were subjected to quantitative analysis on the basis of several metrics that are described in this chapter.

Spectral parameters were used to account for the differences between the three samples. The problem of weak signal strength of biofilms was successfully addressed by virtue of the wavelet decomposition scheme. Two key steps ensured the accuracy of the metrics used to characterize these biofilms. Firstly, the use of agarose as an underlying layer separating the biofilm from the bottom of the plate to avoid overlapping of the returned signal, and then the subsequent denoising of the RF data using a wavelet decomposition technique.

The data imported into Matlab were subject to quantitative analysis on the basis of several metrics that throw light on the underlying trends in the change in data over the period of the time study.

5.1.1 Backscatter Coefficient as a function of frequency

The ultrasonic backscatter coefficient (BSC) is a useful property for characterizing tissues. It is a fundamental material property that can be estimated from backscattered ultrasound signals and can be further parameterized for quantifying tissue properties and classifying

disease. The BSC is defined as the time-averaged scattered intensity in the backward direction per unit solid angle per unit volume normalized by time-averaged incident intensity ($cm^{-1}\ Sr^{-1}$). Therefore, it is a fundamental quantity of a material from which microstructural properties such as shape, size, organization, concentration and impedance mismatch between scatterers and the surrounding media, can be estimated. BSC can be used to estimate both microstructural and acoustical properties of the tissues. Figure 5.1 shows the block diagram for BSC calculation.

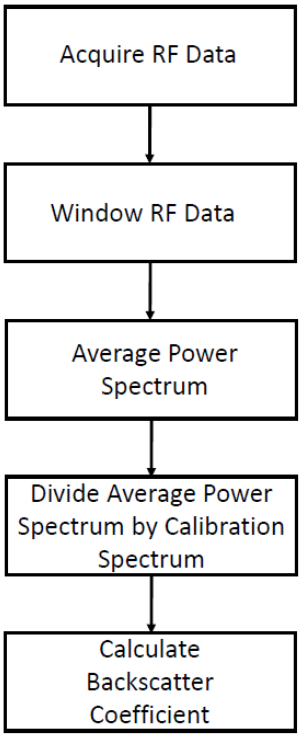

Figure 5.1: Flowchart for estimating BSC

The backscatter coefficient σ_b represents the quantity of acoustic energy backscattered from a volume of biological tissue. Equation 5.1 was used to calculate the backscatter coefficient as a function of frequency [14, 39]:

$$\sigma_b(f) = \frac{1.45\,R^2}{A_0 \Delta Z} W(f) \quad (5.1)$$

where A_0 is the area of the aperture of the transducer, Δz is the axial length of the gated volume, R is the on axis distance between the transducer and the proximal surface of the gated volume, W(f) is the spatial power spectral density of the back scattered signal <S(f)>, divided by that from a reference signal, $S_{ref}(f)$:

$$W(f) = \frac{\langle S(f) \rangle}{S_{ref}(f)} \quad (5.2)$$

5.1.2 Integrated Backscatter Coefficient (IBC)

The backscatter coefficient described in the previous section is calculated as a function of frequency. In order to produce parametric images of the data a coefficient needs to be calculated to represent the scattered intensity.

The integrated backscatter coefficient is used to compensate for attenuation and diffraction effects of ultrasound. It depends on the system parameters like lateral and axial resolution. The integrated backscatter coefficient was calculated according Equation 5.3 [14, 39]:

$$IBC = \int_{f_{min}}^{f_{max}} \frac{\sigma_b(f)}{f_{max} - f_{min}} df \quad (5.3)$$

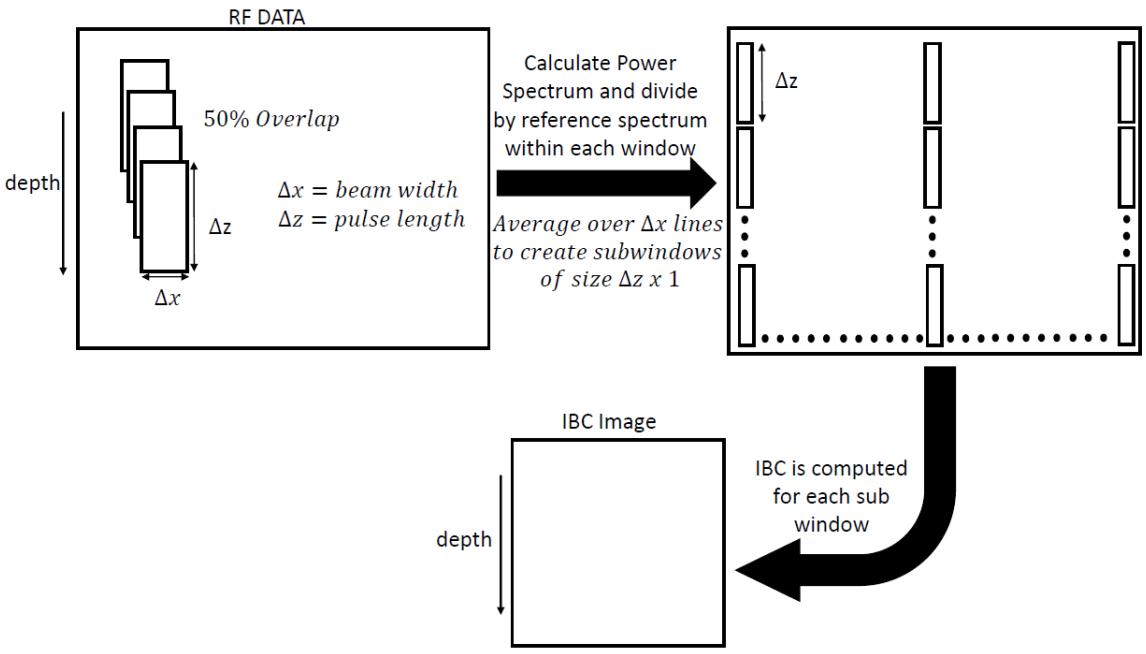

Figure 5.2: Block diagram showing IBC Calculation

Figure 5.2 shows how IBC was calculated. An analytical window was defined with dimensions Δz equal to the pulse length in the axial direction and Δx equal to the beam width in the lateral direction. The power spectrum for each A-line within the window was averaged and normalized by the reference power spectrum to calculate the backscatter coefficient. To compensate for attenuation and diffraction the window was then shifted down with a 50% overlap and the calculation was repeated until the whole height of the sample was covered. The window was then shifted horizontally (laterally) by as many A-lines as can be fitted within the beam width and the calculation was repeated along that column. For example, the 15MHz transducer has a PSF that was experimentally determined to be 200µm. Since A-lines were collected every 100µm it means that 2 lines can be fitted under the full width half maximum of the PSF. This lateral translation was transducer dependent. An M x N matrix was created containing the computed backscatter coefficient

values. This matrix contains sub-matrices with dimensions Δz by 1. The integrated backscatter coefficient was calculated within the – 6 dB bandwidth for each transducer according to Equation 5.3. Liu and Zagzebski showed that a windows size 10 times the wavelength of ultrasound used provides the best estimates of backscatter coefficient [16] . Since the temporal length of the echo was not large enough for a window size as long as suggested by their study, the temporal length equal to the pulse length was used instead. Figure 5.3 (a) and (b) show the B-scan image and corresponding IBC image. It is interesting to note that though both the images look the same the B-mode image is based on the amplitude of the A-line signal while the IBC parametric image is based on IBC which is a frequency dependent metric.

There are other approaches for obtaining the reference power spectrum that have been reported in literature [40-42]. Namely, other solid planar surfaces such as quartz [43, 44], weaker reflectors such as immiscible liquid reflectors and reference phantoms have been used [40, 41, 45, 46]. Although there are other approaches for obtaining the reference spectrum, we used a steel planar reflector because custom electronics with single-element transducers were employed, enabling full control of the transmitted pulse energy and receiver gain settings. However, when system saturation occurs, the approaches using the liquid planar reflector and the reference phantom could be employed.

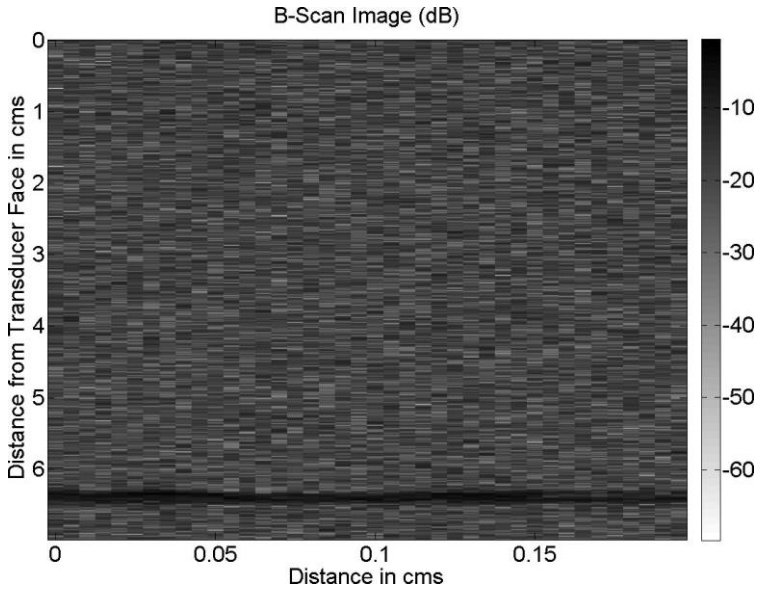

(a)

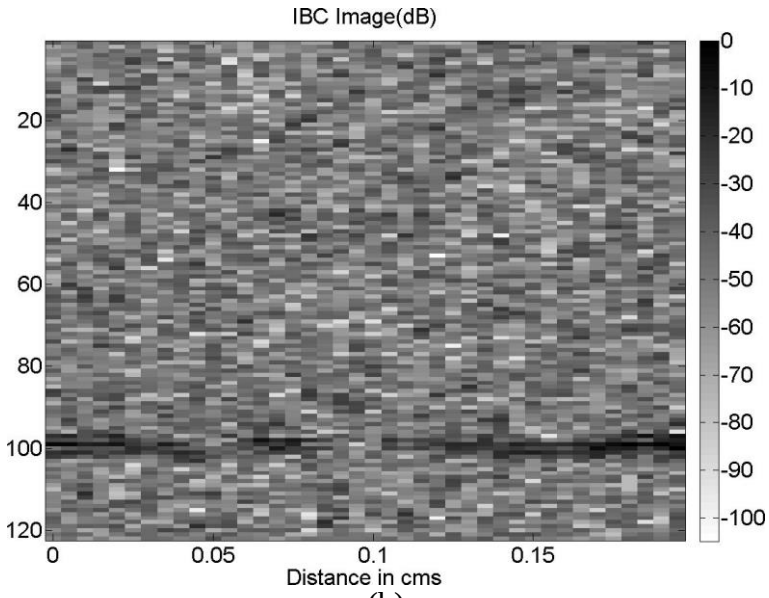

(b)

Figure 5.3 (a): B-scan image identifying the biofilm, (b): Integrated Backscatter Coefficient image highlighting higher scattering regions within the biofilm.

5.1.3 Biofilm/Background Ratio

A region of interest (ROI) was chosen around the location of the biofilm on the IBC image and the mean value in this region was recorded. Another window with size equal to the

ROI was considered in the media region of the image. The mean of this background region was also recorded and these values were used to report the Biofilm/Background ratio. As the acoustic concentration increases the ratio of the IBC in the homogenous scatter region to the IBC in a scatter free region should be indicative of the biofilm microstructure to scatter sound. The degree of this ability can be observed based on this metric.

5.1.4 Peak Frequency Downshift and change in Bandwidth

The raw backscattered signals were imported into Matlab (The Mathworks Inc., Natick, MA) and the one sided Fourier transform was generated to estimate the center frequency of the signal. This was compared to the center frequency of the signal obtained from a perfect reflector and the changes as a function of biofilm maturity were recorded. As biofilms mature they bring about a change in their ability to attenuate ultrasound.

The -3dB and the -6dB bandwidth were recorded from the normalized frequency spectrum of the segmented and denoised biofilm signal. Figure 5.4 shows the original and denoised signal and the corresponding normalized spectra. This change can be tracked by the downshift in frequency and change in bandwidth. A more detailed mathematical derivation that proves this relationship is shown in section 6.3.1 of Chapter 6. This metric gives us a quantitative indication of the ability of tissue to attenuate ultrasound.

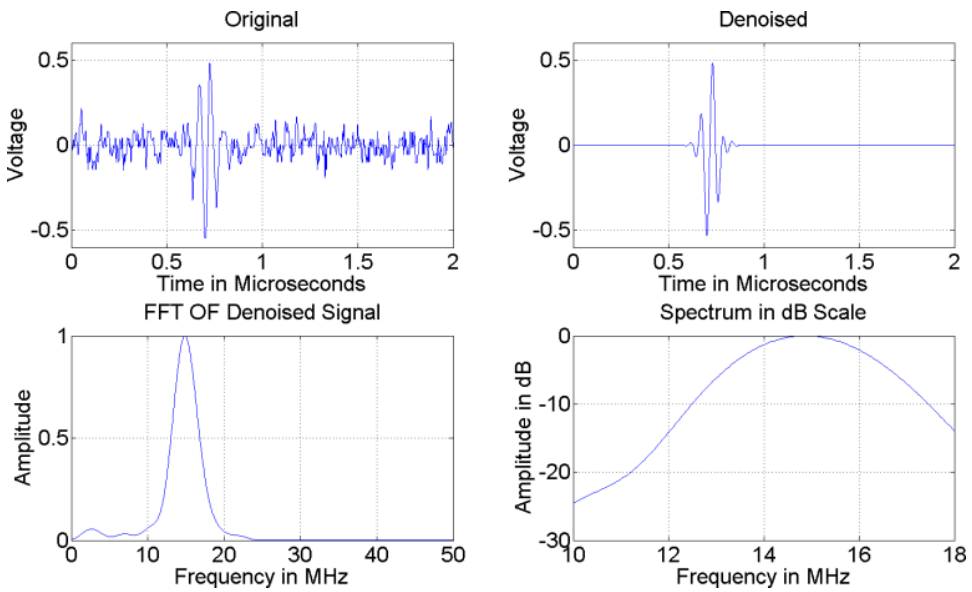

Figure 5.4. Top left panel: Zoom into the raw signal from the biofilm. Top right panel: Corresponding denoised signal. Bottom left panel: Spectrum of the denoised signal. Bottom right panel: Zoom into center peak of denoised spectrum.

5.1.5 Thickness

B-scan images generated from the backscattered signal were used to calculate estimates of the biofilm thickness. Due to limited phase separation between the upper and lower bounds of the biofilm echo an automated approach as shown in Figure 5.5 was used [47]. RF data from A-lines selected based on the routine outlined in the previous section were denoised using the wavelet scheme. The resulting waveform was segmented to isolate the signal corresponding to the biofilm. The absolute value of this signal was converted to the logarithmic scale. A threshold was used to classify samples in the signal as biofilm or noise. This threshold was -20dB below the peak amplitude, which translated to 3 times the standard deviation of the noise based on experimental data. The numbers of samples classified as biofilm were used to calculate the duration of the signal based on the acquisition-sampling rate. A correlation based approach, which involved using the impulse response of the transducer as a correlation window was also attempted. Such correlation

techniques do not produce accurate estimates because the echoes originating from the front and back walls of the biofilm are not discernible. The correlation results are used to detect the location of the two peaks and the absence of these peaks in our data prevented this approach from producing reasonable estimates. Equation 5.4 was used to calculate the thickness of the biofilm, where τ is the thickness of the biofilm, t_2 - t_1 is the timespan in µs of the signal corresponding to the biofilm, c is the speed of sound in the medium assumed to be equal to the speed of sound in water. The two way distance travelled is compensated for by using a factor of $\frac{1}{2}$.

$$\tau = \frac{(t_2 - t_1)c}{2} \tag{5.4}$$

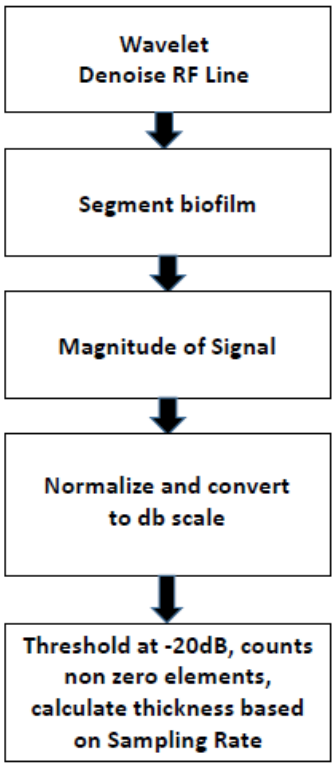

Figure 5.5 Thickness estimation

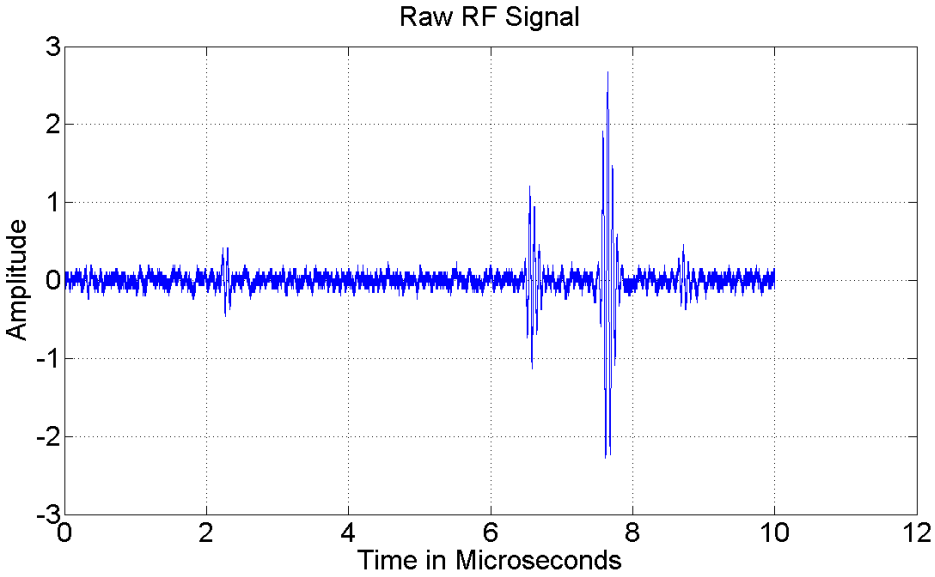
Raw RF Signal
Amplitude
Time in Microseconds
3
2
1
0
-1
-2
-3
0
2
4
6
8
10
12

(a)

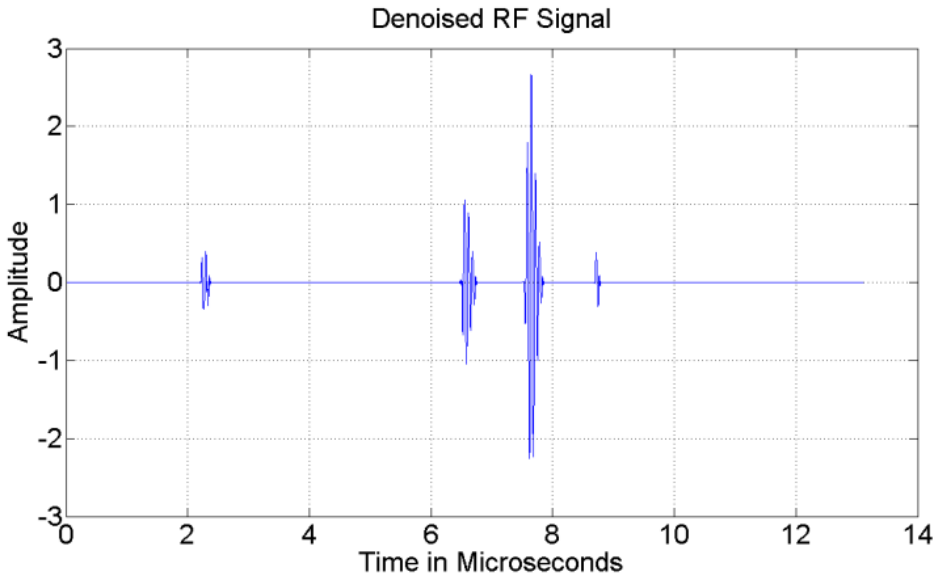
Denoised RF Signal
Amplitude
Time in Microseconds
3
2
1
0
-1
-2
-3
0
2
4
6
8
10
12
14

(b)

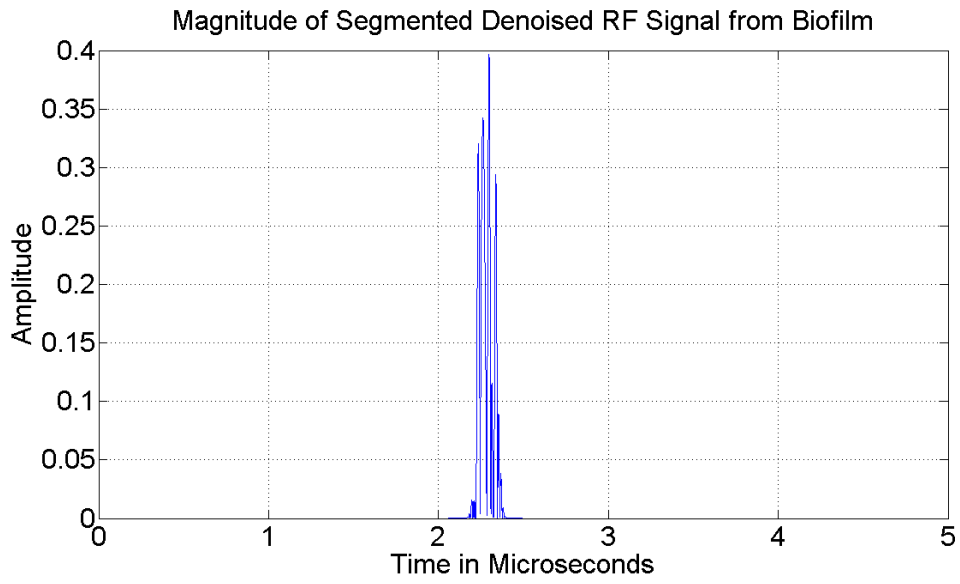

(c)

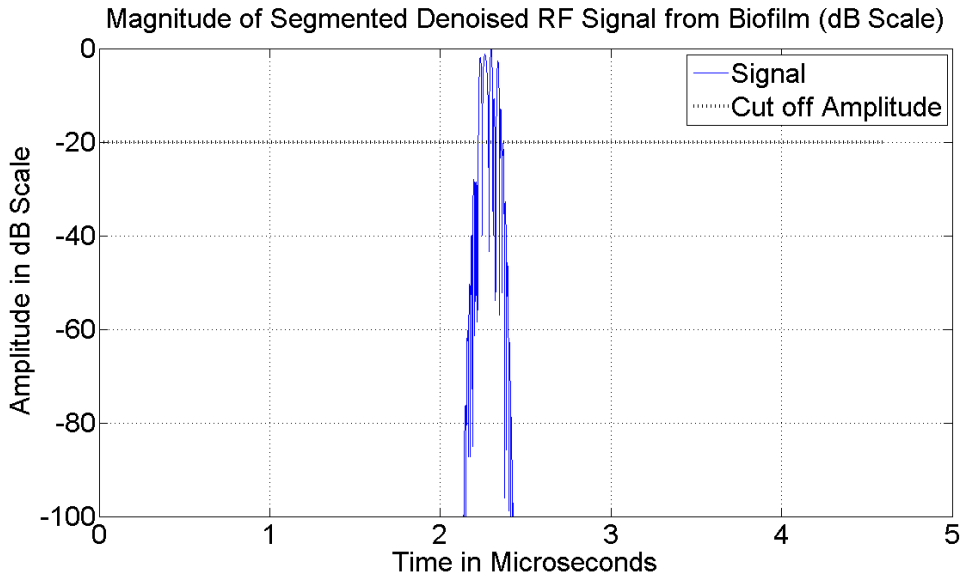

(d)

Figure 5.6: (a) Raw A-line, (b) Denoised A-line, (c) Magnitude of the segmented signal corresponding to the biofilm, (d) Plot of magnitude of signal in dB scale with the -20dB therehold.

5.1.6 Spectral Parameter Estimation

Lizzi *et al.* showed that the frequency response of spherical scatterers of different sizes could be used for characterization based on the slope of the backscattered spectrum after calibration of the transducer [48, 49]. The intercept is related to the acoustic concentration

and the midband fit is related in a statistical sense to integrated backscatter. Quantitative measures of spectral parameters were computed on every A-line within the usable bandwidth of the transducer. The calibrated spectrum (in dB) was analyzed using a linear regression:

$$S(f) = \beta . f + I \tag{5.5}$$

where f is the frequency (MHz), β is the spectral slope (dB/MHz) and I is the spectral intercept and the midband fit M of the spectral linear regression is the value of the linear fit at f_c, the center of the frequency bandwidth employed

$$M = S(f_c) = \beta . f_c + I \tag{5.6}$$

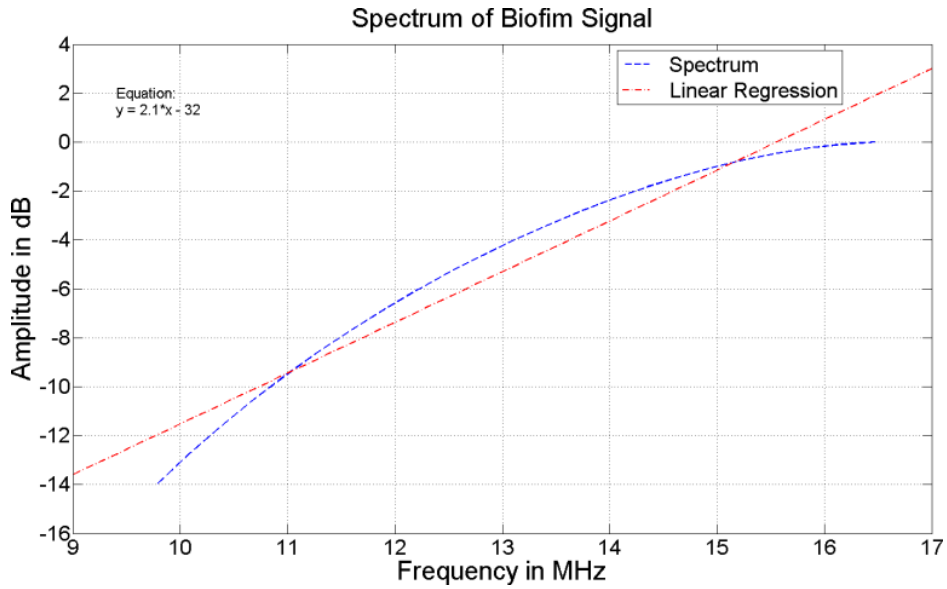

Figure 5.7: Midband fit

5.2 Experimental Protocol

Three experiments conducted over a period of three weeks were performed to image and characterize Nontypeable *Haemophilus influenzae,* (NTHi) biofilms, *Streptococcus pneumoniae* (Sp) biofilms, and a combination of *Haemophilus influenzae* and

Streptococcus pneumoniae (NTHi + Sp) biofilms. After inoculation of microliter plate wells all plates were incubated at 37°C for 2 days before beginning the study. Each separate biofilm of NTHi, Sp and the combined NTHi + Sp was probed over a span of 4 days. The fully characterized 15MHz transducer was used to run raster scans of the sample covering an area of 4000μm^2. The stepper motors were used to move the transducer with a step size of 100μm laterally. For every scan 40 reads in the x- and y-direction translated to 1600 recorded A-lines. One in 4 of these A-lines in both directions was chosen for analysis. Therefore all metrics were calculated based on the 100 A-lines chosen. The full width at half maximum of the PSF plot gives an estimate of the lateral resolution of the system, 200μm in our case. Since our step size is 100μm and we pick every 4th A-line for further analysis, we ensure that the data being analyzed are independent and resolvable by our system. This in conjunction with wavelet denoising further enhances the accuracy of our analysis.

A LabView graphic user interface designed to control the entire system also ran a Matlab script to generate the B-scan images and store the raw data in text files which were used to calculate the aforementioned metrics. All resulting plots shows the change in the metrics considered as a function of biofilm maturity for *Haemophilus influenzae, Streptococcus pneumoniae,* and for the combination of *Haemophilus influenzae* and *Streptococcus pneumoniae*. Results are given as mean ± sem (squared error of mean).

5.3 Results

Results in Figure 5.7 (a), (b) and (c) show the trend within samples as a function of time for the peak frequency, the 3dB bandwidth and the biofilm to background ratio discussed

in Section 4. Results are analyzed using Prism 6, where unpaired t-tests with a 95% confidence interval were performed while comparing between Days 1 and 4 for each species and one way ANOVA tests were used while comparing between the three groups for Days 1 and 4 separately.

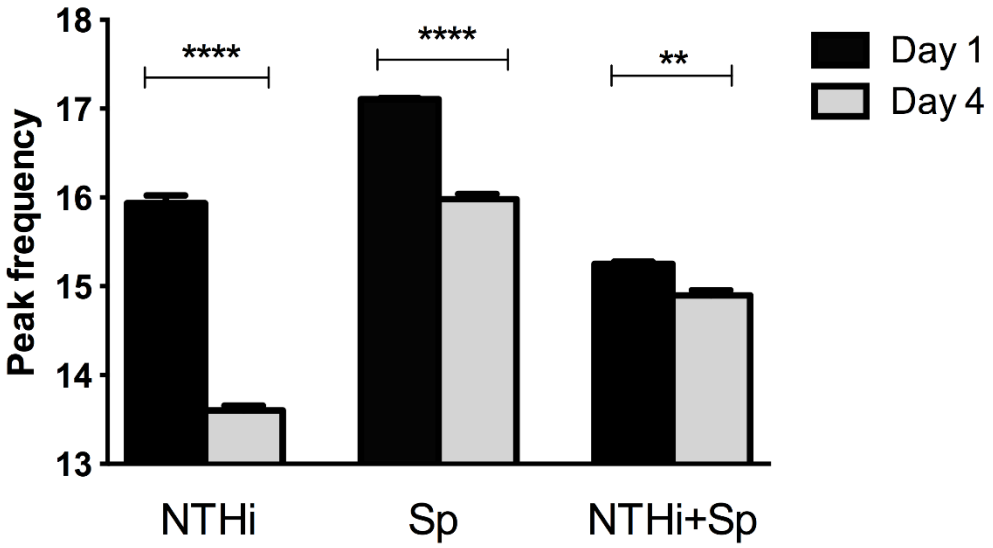

(a)

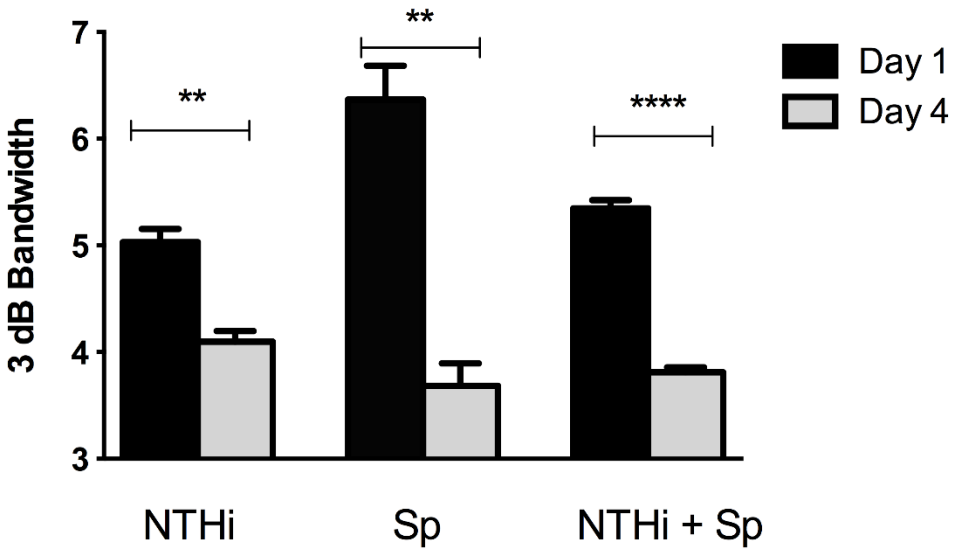

(b)

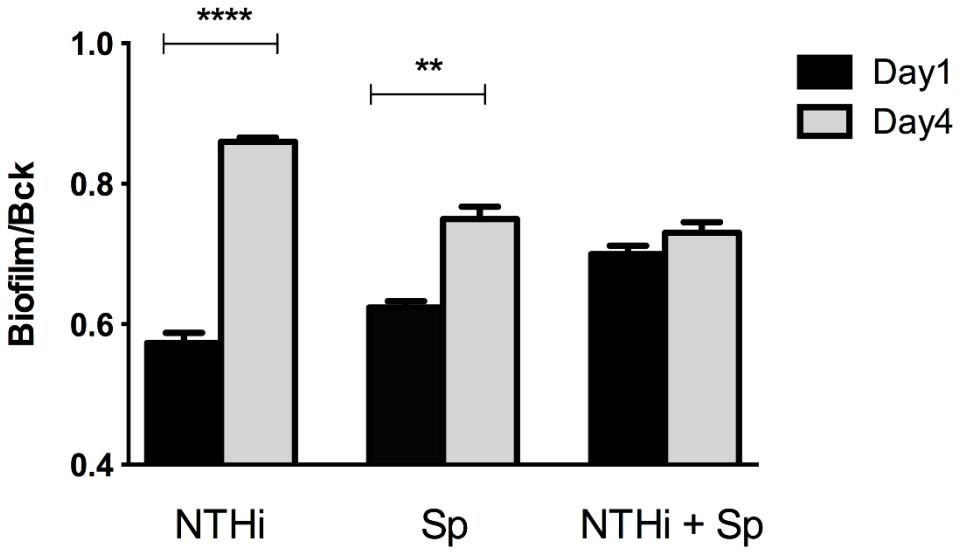

(c)

Figure 5.8: Results of unpaired t-test on trends within samples as a function of maturity for (a) Peak frequency; (b) 3dB Bandwidth; and (c) Biofilm to background ratio showing the ability of these parameters to differentiate biofilms as they mature.

Figure 5.8(a) shows a significant difference in the peak frequency value ($p<0.0001$) for the biofilms formed by NTHi and Sp as they mature. The combined NTHi + Sp samples are significant at $p=0.006$. Figure 5.8(b) shows a significant difference in -3dB bandwidth value at $p=0.004$ (NTHi) and $p=0.002$ (Sp) as the biofilms mature. The combined biofilms are significant at $p<0.0001$. These two results confirm that attenuation increases as biofilms mature. Figure 5.8(c) shows a significant difference ($p<0.0001$) in the biofilm to background ratio for NTHi, and a significant difference ($p=0.003$) for the Sp biofilms, however there is no significant difference for the combined sample as it matures.

Figures 5.9 (a), (b), and (c) look at the trends in these parameters as biofilms mature comparing samples using a one-way ANOVA test. Figure 5.9(a) shows there is a significant difference ($p<0.0001$) in the peak frequency value when comparing the three

samples to each other, both at day 1 and day 4. Moreover, there is a significant difference ($p<0.0001$) when comparing day 1 vs day 4. Figure 5.9(b) shows a significant difference ($p=0.008$) among samples at day 1; however, there is no significant difference among samples at day 4. It should be noted that when comparing the overall results from day 1 to day 4 there is a significant difference ($p<0.0001$) in reduction of bandwidth. These results confirm an increase in attenuation as the biofilms mature.

Figure 5.9(c) shows a significant difference when comparing samples at day 1 and day 4 ($p=0.0009$). These results point to the feasibility of distinguishing single- and multi-species biofilms using the integrated backscatter coefficient. Moreover, there is a significant difference ($p<0.0001$) when comparing day 1 vs. day 4.

Quantitative backscatter measurements provide a measure of the mean-backscatter cross-section per unit volume, i.e. the effectiveness with which the biofilm scatters energy. This effectiveness increases as the biofilms mature.

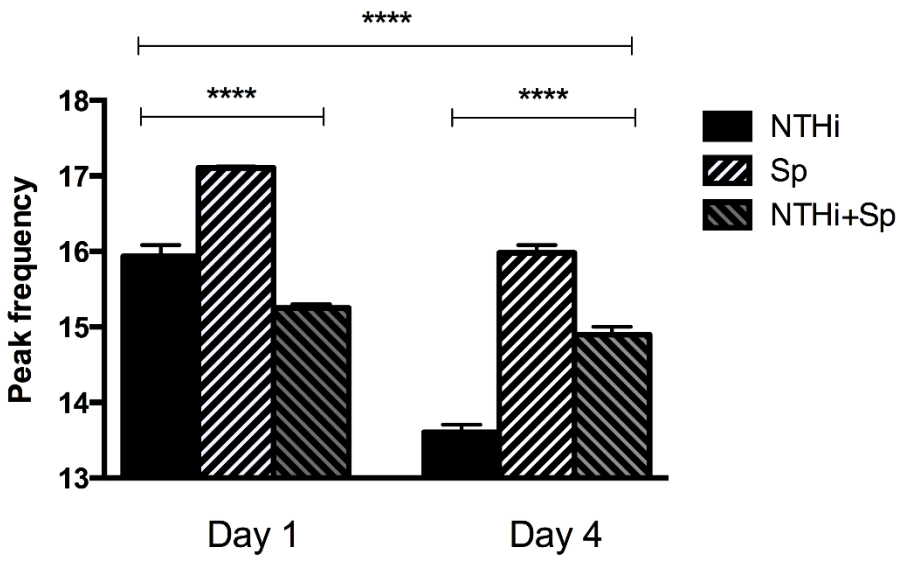

(a)

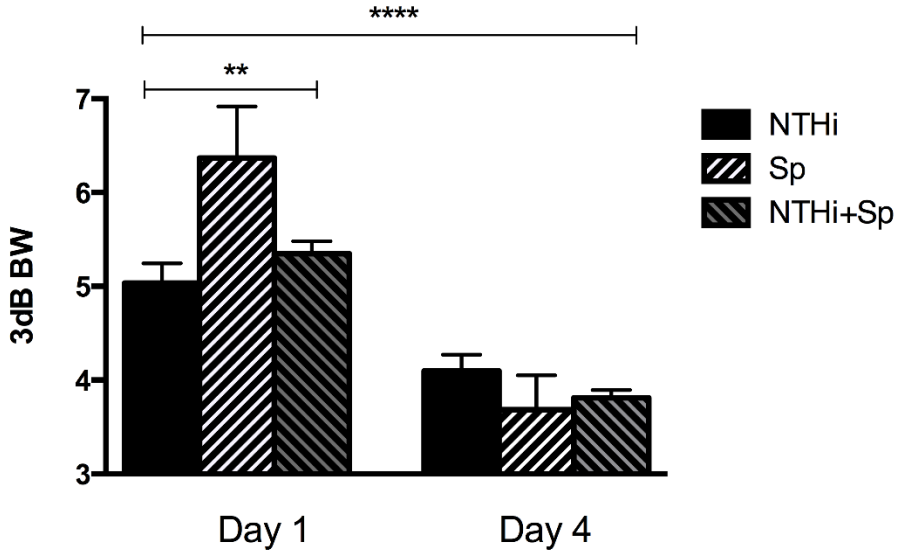

(b)

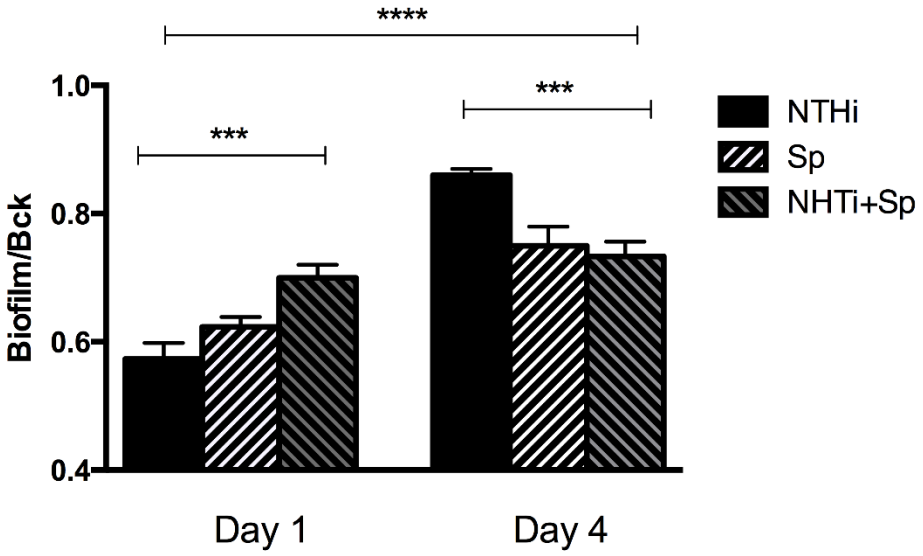

(c)

Figure 5.9: One-way ANOVA results for (a) Peak frequency; (b) 3dB Bandwidth; and (c) Biofilm to background ratio showing the ability of these parameters to differentiate between single- and multi-species biofilms.

Lizzi *et al.* [48, 49] suggest that an increase in size and concentration of scatterers results in an increase in the midband fit and the intercept value. We observe an increase in these

parameters as a function of time as is shown in Figure 5.10. One-way ANOVA tests show there is a significant difference ($p<0.0001$) in intercept and midband fit when comparing day 1 vs. day 4 for all samples.

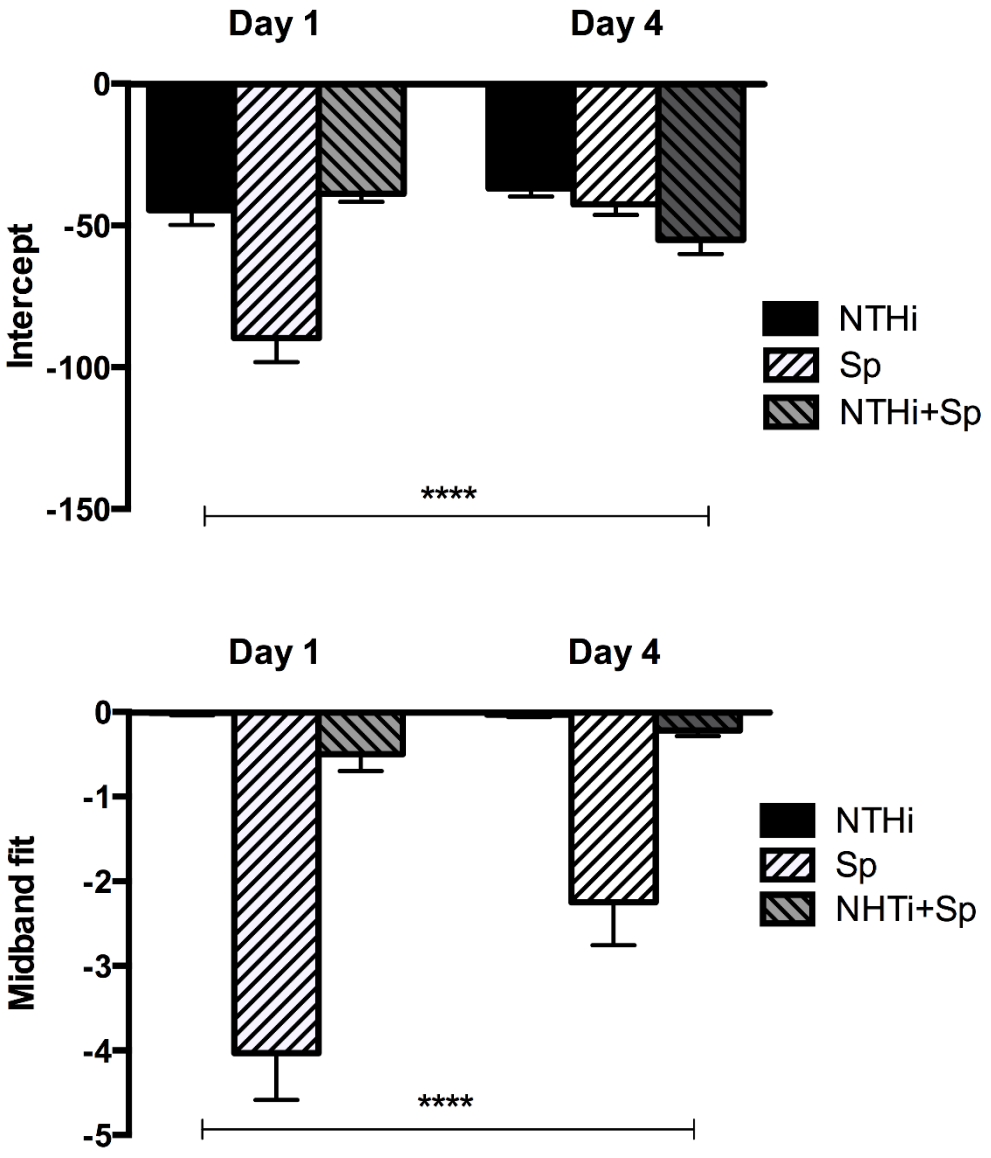

Figure 5.10: One-way ANOVA results for (a) Intercept; and (b) Midband fit; showing the ability of these parameters to differentiate biofilm behavior as a function of time.

5.4 Conclusion

In this study we used a quantitative ultrasonic technique to characterize three samples of biofilm for NTHi, Sp, and NTHi+Sp. Reproducible trends in the data collected were observed that point towards the efficacy of such a technique to not only detect the presence of a biofilm but also differentiate between strains. These results will be described in more detail in Chapter 8.

Chapter 6

Conventional ultrasound imaging can resolve structures from hundreds of micrometers to centimeters in scale. One of the limitations of ultrasound is the inability to resolve sub resolution scatterers (structures smaller than the acoustic wavelength). Since the size of biofilm structures lies in this range, an indirect approach to estimate sizes of sub resolution scatterers is required. The frequency content of the backscattered pulse depends on the size, shape and distribution of the scatterers. Under the assumption of random scattering, specific geometric shape of the individual scatterer and inhomogeneous scattering, mathematical models can be used to describe this dependence. Relating the frequency dependent RF signal to models of tissue microstructure leads to estimates of scatterer properties that can be used as an effective characterization metric. The advantage in using estimates of scatterer properties such as effective scatter size is that the estimated property is uniquely related to physical microstructure of the tissue samples being studied.

6.1 Review of theories developed to study the scattering of sound waves by different structures

Faran's theory [50] gives exact solutions of the scattered field created by simple shapes such as spheres and cylinders. Generalized approaches are used to predict the scattered wave in a weakly scattering inhomogeneous medium. These theories naturally lead to the concept of Form factor modelling of scattered ultrasound waves. Faran's theory gives closed form solutions for the scattered pressure radiated by a uniform sphere or a cylinder from an incident plane wave. Farans's closed form functions allow for good comparison

with scattering from tissues because some constituents of tissues can be seen as a first approximation of spheres and cylinders. Extending these theories to describe weakly scattering inhomogeneous media assumes that the in homogeneities that cause the scattering have tissue property values such as density and compressibility very close to that of the propagating medium. Our biofilm experiments can be approximated as having an inhomogeneous and weakly scattering medium.

For an incident plane wave of unit amplitude, the case of the Born approximation where multiple scattering is ignored, the backscattered pressure wave far from an interrogated volume is a spherical wave defined as

$$p_{bs} = \frac{e^{-ikr}}{r}\varphi(2k) \tag{6.1}$$

Where bs denotes backscattered, k is the propagation constant ($k = \omega/c$) where ω is the angular frequency and c is the speed of sound in the propagating medium. $\varphi(2k)$ is called the angle distribution function as derived by Morse and Ingrad [51]. r is an observation point which is far from the volume.

$$\varphi(2k) = \frac{k^2}{4\pi}\iiint_{V_0} \gamma(r_o)\, e^{-2ikr_0} dv_o \tag{6.2}$$

V_0 represents the scattering volume, and the function $\gamma(r)$ for an observation point r called the relative impedance function is

$$\gamma(r) = \gamma_\kappa(r) - \gamma_\rho(r) \tag{6.3}$$

where

$$\gamma_\kappa(r) = \frac{\kappa(r) - \kappa_0}{\kappa_0} \tag{6.4}$$

And

$$\gamma_\rho(r) = \frac{\rho(r) - \rho_0}{\rho(r)} \tag{6.5}$$

The quantities κ and ρ are the compressibility and the density. For an ensemble of particles the pressure field comprises of a coherent field and an incoherent field. The relationship between the scattered intensity and the scattered pressure field is

$$\rho_o c\langle I\rangle = \langle|p_{bs}|^2\rangle = \langle\left|p_{bs(Coh)}\right|^2\rangle + \langle\left|p_{bs(Incoh)}\right|^2\rangle \tag{6.6}$$

For an ensemble the average backscatter coefficient σ_d also called the average differential cross section by Insana [13] can be calculated. The quantity is defined as the powered scattered into a unit solid angle divided by the product of the incident intensity and the insonified volume at large observational distances. The average scattering intensity is given by

$$\langle I\rangle = \frac{\langle|\varphi(2k)|^2\rangle}{\rho_o c r^2} \tag{6.7}$$

$$\sigma_d = \frac{r^2}{V}\frac{\langle I\rangle}{I_0} \tag{6.8}$$

Where $I_0 = 1/\rho_o c$

Equations 6.2, 6.7 and 6.8 can be combined to express σ_d in terms of the spatial autocorrelation function B_γ of the scattering medium as follows:

$$\sigma_d = \frac{k^4}{16\pi^2 V}\langle\int \gamma(r_1)\, e^{-2ikr_1} dv_o \int \gamma(r_2)\, e^{2ikr_2} dv_o\rangle \tag{6.9}$$

$$= \frac{k^4}{16\pi^2 V}\iint \gamma(r_1)\,\gamma(r_2) e^{-2ik(r_1 - r_2)} dv_o$$

This equation can be reduced by introducing sum and difference variables

$u = \frac{(r_1 - r_2)}{2}$ and $\Delta r = (r_1 - r_2)$ yielding

$$\sigma_d = \frac{k^4}{16\pi^2 V} \int B_\gamma (\Delta r)\, e^{-2ik\Delta r}\, dv_o \tag{6.10}$$

where

$$B_\gamma(\Delta r) = \frac{1}{V} \langle \int \gamma\left(u + \frac{\Delta r}{2}\right) \gamma\left(u - \frac{\Delta r}{2}\right) \rangle\, du \tag{6.11}$$

If we assume that the random process $\gamma(r)$ is weakly stationary, $\langle \gamma(r_1) \rangle$ and $\langle \gamma(r_1 + \Delta r) \rangle$ should not vary with position and $\langle \gamma(r_1)\gamma(r_2) \rangle$ depend only on Δr. As shown before $B_\gamma(\Delta r)$ can be represented as a combination of its coherent and incoherent components.

$$B_\gamma(\Delta r) = \langle \gamma_1 \rangle \langle \gamma_2 \rangle + \langle (\gamma_1 - \langle \gamma_1 \rangle)(\gamma_2 - \langle \gamma_2 \rangle) \rangle \tag{6.12}$$

Where $\gamma_1 = \gamma(r_1)$ and $\gamma_2 = \gamma(r_2)$

$$B_\gamma(\Delta r) = |\langle \gamma \rangle|^2 + C_\gamma(\Delta r) \tag{6.13}$$

Where $C_\gamma(\Delta r)$ is the auto-covariance function that can be expressed as the product of the variance $\langle |\gamma - \langle \gamma \rangle^2| \rangle$ and the correlation coefficient, $b_\gamma(\Delta r)$

$$B_\gamma(\Delta r) = |\gamma^2| + \langle |\gamma - \langle \gamma \rangle^2| \rangle b_\gamma(\Delta r) \tag{6.14}$$

Where $b_\gamma(0) = 1\ and\ b_\gamma(\infty) = 0$. The correlation coefficient depends on the structure of the scattering medium.

Assuming random and isotropic conditions, the coherent component is negligible and σ_d is entirely due to incoherent scattering. Substituting 6.14 into 6.10 yields

$$\sigma_d = \frac{k^4}{16\pi^2 V} \bar{n} \gamma_0^2 \int b_\gamma (\Delta r)\, e^{-2ik\Delta r}\, dv_o \tag{6.15}$$

The above equation is the basis for correlation models for random media. Three dimensional correlation models for different scatterer geometries can be used to derive closed-form frequency dependent functions.

6.2 Form Factors

Models that describe the amplitude of the backscattered intensity due to a single scattering structure or to an ensemble as a function of frequency are called Form Factor functions (FFs).

Form factors are based on the 3D spatial correlation models by assuming some form or shape for the scattering tissue structures. Usually scattering shapes are assumed and in most cases they have a spherical symmetry. Mathematical form factors are related to the shape of the scatterer through the Fourier transform. The Form Factor can be thought of as the Fourier transform of the single scatterer's shape. Commonly used FFs are the Gaussian, the fluid sphere and the spherical shell. The Gaussian form factor as derived by Insana has been used to describe biological materials (Insana et al. 1990b) to represent a spherical scatterer that varies with the surrounding tissues and has a uniform particle radius. It does not assume sharp discontinuities in the impedance but is represented by a gradual change from surrounding tissues. The Gaussian form factor describes an effective radius a_{eff} rather than a definite radius.

Experimental data can be fitted to the Gaussian form factor model to get an estimate of the effective radius. This estimate of the effective radius is a powerful characterization tool that was used to differentiate between different statins of biofilms.

In the Gaussian model the correlation coefficient is given by

$$b_\gamma(\Delta r) = e^{-\Delta r^2/2d^2} \tag{6.16}$$

Where d is a characteristic dimension.

The backscatter coefficient can be calculated by substituting the correlation coefficient in equation 6.15

$$\sigma_d = (\bar{n}k^4 V_s^2 \gamma_0^2/16\pi^2)\, e^{2k^2d^2} \tag{6.17}$$

Where $V_s^2 = (2\pi d^2)^3$

And $\sigma_0 = (\bar{n}k^4 V_s^2 \gamma_0^2/16\pi^2)$

The acoustic intensity form factor is defined as the ratio of the backscatter coefficient of the test material having scatterers with finite size to that of a similar material having point scatterers.

$$F(f, a_{eff}) = \sigma_b/\sigma_0 \tag{6.18}$$

The Gaussian form factor is calculated by substituting σ_b and σ_0 in the above equation

$$F(f, a_{eff}) = exp^{-0.827(ka_{eff})^2} \tag{6.19}$$

where $k = \frac{2\pi f}{c}$, c being the speed of sound in the medium.

Figure 6.1 shows a plot of the Gaussian form factor. The Gaussian form factor model is valid for a range of ka values. The ka range is dependent on the transducer frequency and the scatter size. For a frequency range of around 15MHz the model is capable of predicting effective scatter sizes in the range of 5 to 30 micrometers.

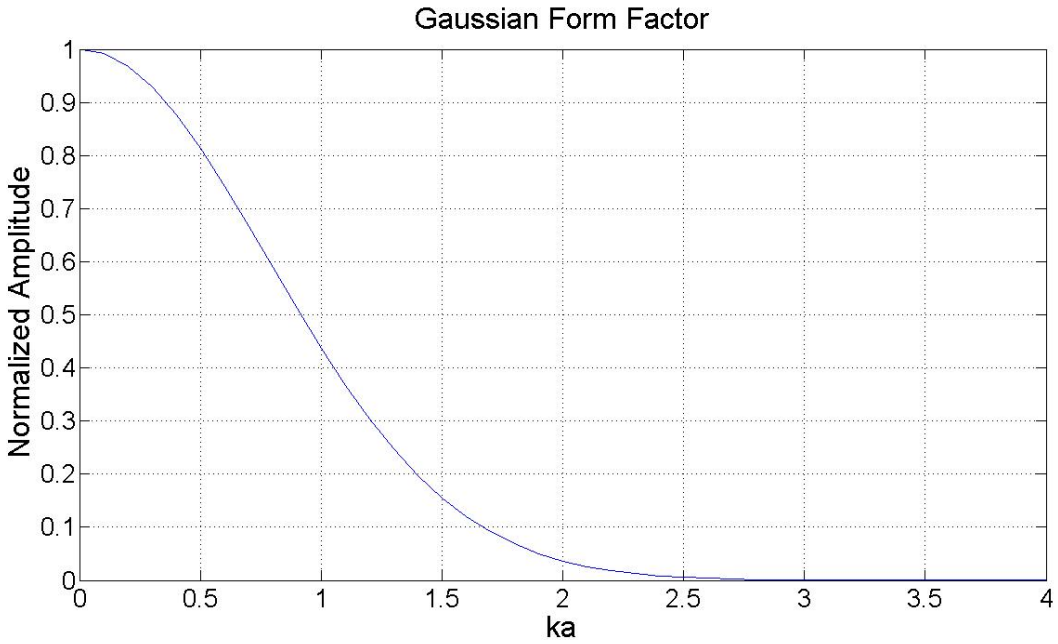

Figure 6.1 Plot of Gaussian Form Factor Model

In order to obtain the size estimates, certain calibrations need to be performed. The transducer frequency response is removed by dividing the RF data by a perfect reflector's reference spectrum. The strategy for estimating the effective scatter size involves standard least square methods.

6.3 Estimation Schemes

The Gaussian transformation and the spectral fit algorithm were considered to estimate the effective scatter radius via a fitting routine that used the biofilm power spectrum and the form factor after appropriate normalization. The Gaussian transformation algorithm makes the assumption that the power spectrum of the biofilm is Gaussian in shape [52]. Estimates of the center frequency and bandwidth of the signal were obtained by fitting a Gaussian to the power spectrum. A similar scheme was used to obtain the center frequency and the bandwidth of the reference spectrum multiplied by the Form factor. The difference in

bandwidths was minimized by varying the effective radius. The spectral fit algorithm on the other hand makes no assumptions about the shape of the backscattered spectrum and fits a curve through the biofilm power spectrum.

6.3.1 Gaussian Transformation Algorithm

Insana *et al.* [13] showed that the reference spectrum is proportional to the echo signal from a rigid plane positioned at the focus multiplied by k_o^4. The expected value of the backscattered voltage $E\left[\left|V_{refl}\right|^2\right]$is given by [53]

$$E\left[\left|V_{refl}\right|^2\right] \alpha\ k_0^4\left|V_{plane}(\omega)\right|^2 F\left(f, a_{eff}\right) \tag{6.20}$$

Where $V_{plane}(\omega)$ is the Fourier transform of the voltage signal returned from a rigid plane. $F\left(f, a_{eff}\right)$ is the form factor related to the scatter geometry. The form factor can be expressed as a power law $e^{-Af^n}$and over a limited frequency range the source and diffraction characteristics can be assumed to be Gaussian.

$k_0^4\left|V_{plane}(\omega)\right|^2 \alpha \exp(-\frac{(f-f_o)^2}{2\sigma_\omega^2})$, then the backscattered voltage is given by

$$E\left[\left|V_{refl}\right|^2\right] \alpha \exp\left(-\frac{(f-f_o)^2}{2\sigma_\omega^2}\right) e^{-Af^n} \tag{6.21}$$

This equation can be approximated to a Gaussian by making the following simplifications

$$E\left[\left|V_{refl}\right|^2\right] \alpha\ \exp\left(-\frac{(f-f_o)^2}{2\sigma_\omega^2}\ -\ Af^n\right)$$

$$\alpha\ \exp\left(-\frac{(f-f_o)^2}{2\sigma_\omega^2}\ -\ A(f_0^n + n(f-f_o)f_0^{n-1} + \frac{n(n-1)(f-f_o)^2 f_0^{n-2}}{2}\right.$$

$$\left. + \cdots\right)$$

$$\alpha\ \exp\left(-\frac{(f-f_o)^2}{2\sigma_\omega^2}\ -\ f(Anf_0^{n-1}) - \frac{An(n-1)(f-f_o)^2 f_0^{n-2}}{2} + \cdots\right)$$

$$\alpha\ \exp\left(-\frac{(f-f_o)^2}{2}\left[\frac{1}{\sigma_\omega^2} +\ An(n-1)f_0^{n-2}\right] -\ f(Anf_0^{n-1}) + \cdots\right)$$

$$\alpha\ \exp\left(-\frac{f^2 - 2ff_0\ +\ f_0^2}{2\sigma_\omega'^2} -\ f(Anf_0^{n-1}) + \cdots\right)$$

$$\alpha\ \exp\left(-\frac{f^2 - 2(f_0\ -\ \sigma_\omega'^2 Anf_0^{n-1})f\ +\ f_0^2}{2\sigma_\omega'^2} + \cdots\right)$$

$$\alpha\ \exp\left(-\frac{f\ -\ f_0')^2}{2\sigma_\omega'^2} - + \cdots\right)$$

where $f_0' =\ f_0 - \sigma_\omega'^2 Anf_0^{n-1}$

and $\sigma_\omega'^2 =\ \left[\frac{1}{\sigma_\omega^2} +\ An(n-1)f_0^{n-2}\right]^{-1}$

This first order approximation shows that the scatter size changes the bandwidth and center frequency of the returned spectrum. In order to estimate the effective scatter size the backscattered spectrum from the biofilm had to be fitted to a Gaussian spectrum. To overcome the low SNR of the backscattered spectrum 10 independent lines acquired were averaged in the log domain. Multiplicative noise is most effectively removed by averaging in the log domain.

$$E\left[\left|V_{refl}\right|^2\right] \cong P_{scat}(\mathrm{f}) =\ \exp\left[\frac{1}{10}\sum_{i=1}^{10}\ln(|V_i|^2)\right] \tag{6.22}$$

Where V_i is the backscattered spectrum. After averaging the resulting spectrum was fit to a Gaussian, also in the log domain to estimate f_0' and $\sigma_\omega'^2$, the center frequency and bandwidth

$$[f_0', \sigma_\omega'^2] = min\left\{mean\left(P_n(f) - P_p(f, f_0', \sigma_\omega'^2) - \bar{P_n}\right)^2\right\} \tag{6.23}$$

Where

$$P_n(f) = ln\left(\frac{P_{scat}(\mathrm{f})}{\max(P_{scat}(\mathrm{f}))}\right) \tag{6.24}$$

$$P_p(f, f_0', \sigma_\omega'^2) = -\frac{(f - f_0')^2}{2\,\sigma_\omega'^2} \tag{6.25}$$

$$\bar{P_n} = mean(P_n(f) - P_p(f, f_0', \sigma_\omega'^2)) \tag{6.26}$$

The center frequency and bandwidth of the reference spectrum was obtained by solving

$$[f_0', \sigma_\omega'^2] \tag{6.27}$$

$$= min\left\{mean\left(\left(\left(\frac{k_0^4\left|V_{plane}(\omega)\right|^2 F(f, a_{eff})}{\max(k_0^4\left|V_{plane}(\omega)\right|^2 F(f, a_{eff}))}\right)\exp\left(-\frac{(f - f_o)^2}{2\sigma_\omega^2}\right)\right)^2\right)\right\}$$

The value of a_{eff} was varied to find the reference bandwidth that minimized its difference with the bandwidth of the backscattered signal.

The Gaussian transformation algorithm did not produce reasonable estimates of the scatter size for the data set used in the experiments conducted due to the high noise content and fluctuations despite the preventive measures taken to overcome this problem.

6.3.2 Spectral Fit Algorithm

The limitation of the Gaussian transformation algorithm was the assumption about the Gaussian shape of the backscattered power spectrum. The algorithm produces inaccurate estimates when the SNR is low. The spectral fit algorithm makes no assumption about the shape of the power spectrum and fits a line through the backscattered power spectrum instead. The spectral fit algorithm which fits experimental data to the theoretical form factor model was used to estimate effective scatter size after preprocessing of the signal. The fitting scheme is described below.

Insana *et al.* [13] showed that the reference spectrum is proportional to the echo signal from a rigid plane positioned at the focus multiplied by k_o^4.

$$P_{ref}\,(f) = k_o^4\,\left|V_{plane}(f)\right|^2 \tag{6.28}$$

where $\left|V_{plane}(f)\right|^2$ is the reference spectrum.

A standard minimization routine was used to fit the preprocessed data. The value of a_{eff} was found by minimizing the error given by

$$Error = \; mean\left[\left(X\left(f, a_{eff}\right) - \; \overline{X}(f, a_{eff}\right)^2\right] \tag{6.29}$$

Where

$$X\left(f, a_{eff}\right) = \ln\left(\frac{P_{scat}(f)}{max\left(P_{scat}(f)\right)}\right) - \; ln\left(\frac{P_{ref}(f)\,F\left(f, a_{eff}\right)}{\max\left(P_{ref}(f)\,F\left(f, a_{eff}\right)\right)}\right) \tag{6.30}$$

$$\bar{X}\left(a_{eff}\right) = \; mean[X\left(f, a_{eff}\right)] \tag{6.31}$$

6.4 Noise reduction techniques

The efficacy of the estimation techniques is closely dependent on the SNR of the backscattered signal. Electronic noise is a primary reason that affects SNR. Electronic

noise can be assumed to be additive, white with zero mean [53]. The addition of electronic noise changes the bandwidth of the scattered signal resulting in a biased estimate of the effective scatter size. The expected spectrum over a set of possible additive noise for a given scatter distribution is given by

$$E_N\left[\left|V_{refl}(f)+N(f)\right|^2\right] = \left|V_{refl}(f)\right|^2 E_N\left[\left|1+\frac{N(f)}{V_{refl}(f)}\right|^2\right] \tag{6.32}$$

$$= \left|V_{refl}(f)\right|^2\left(1+\frac{E_N[|N(f)|^2]}{\left|V_{refl}(f)\right|^2}\right)$$

Where $N(f)$ is the additive noise and $E_N[|N(f)|^2]$ is the expected value with respect to noise statistics. Averaging the spectra in the log domain results in a corrupted spectrum as shown below

$$P_{scat}(\mathrm{f}) = \exp\left[\frac{1}{10}\sum_{i=1}^{10}\ln\left(\left(|V_i(f)|^2\left(1+\frac{E_N[|N(f)|^2]}{\left|V_{refl}(f)\right|^2}\right)\right)\right)\right]$$

$$= \exp\left[\frac{1}{10}\sum_{i=1}^{10}\ln(|V_i(f)|^2) + \ln\left(1+\frac{E_N[|N(f)|^2]}{\left|V_{refl}(f)\right|^2}\right)\right]$$

$$= P_{scat\_ideal}(\mathrm{f})\exp\left[\frac{1}{10}\sum_{i=1}^{10}\ln\left(1+\frac{E_N[|N(f)|^2]}{\left|V_{refl}(f)\right|^2}\right)\right]$$

$$= P_{scat\_ideal}(\mathrm{f})\left(1+\frac{E_N[|N(f)|^2]}{\left|V_{refl}(f)\right|^2}\right)$$

$$\text{Hence, } P_{scat\_ideal}(\mathrm{f}) \cong \frac{P_{scat\_measured}(\mathrm{f})}{\left(1+\frac{E_N[|N(f)|^2]}{\left|V_{refl}(f)\right|^2}\right)} \tag{6.33}$$

The effect of the noise can be reduced by dividing the spectrum of the biofilm by the term

$$1 + E_N[\,|N(f)^2|]/P_{scat}(f) \tag{6.34}$$

A noise term can be determined in an experimental setup by recording data in the absence of a transmitted signal and then taking the mean value over all possible frequencies. Where $N(f)$ is the noise spectrum, $P_{scat}(f)$ is the spectrum of the scattered signal (biofilm), $|V_i|^2$ is the spectrum of a A-line signal.

$$P_{scat} = \frac{\exp\left[\frac{1}{10}\sum_{i=1}^{10}\ln(|V_i|^2)\right]}{1+ E_N[\,|N(f)^2|]/\exp(\frac{1}{25}\sum_{i=1}^{25}\ln(|V_i|^2)} \tag{6.35}$$

The noise spectrum was determined in an experimental setup by recording data in the absence of a transmitted signal. Bigelow and O'Brian showed that accounting for system noise improves the accuracy of the estimate parameters. Choosing the range of frequencies over which the estimation was performed is crucial to the efficacy of the algorithm. The goal is to exclude frequency channels from the calculation that correspond to noise. Frequency channels corresponding to a signal that was 30 dB above the noise floor were chosen for the estimation. Estimates of the effective scatter size were calculated using the described method for three repeats of each of the cases considered.

6.5 Discussion and results

The Gaussian form factor allows us to estimate the effective scatter size as opposed to a real size estimated based on other form factor models. The assumptions made to derive the closed form expressions do not conform to the real shape or size of the scatterers under investigation therefore in isolation the findings do not convey any valuable information about the sub resolution scatterers. However, comparing the parameters estimated via these estimation schemes in a consistent manner allows us to differentiate between the three cases considered in the experiments conducted. It is also important to note that the Form factor models are valid within a certain ka range. Since our experiments were conducted

using a 15MHz transducer this puts a limit on the range of scatter sizes that the model can predict. Biofilms at a cellular level have been reported to be in the order of 10 micrometers and these sizes lie within the range of the Gaussian form factor model for experiments conducted in the range of 15 MHz

The experimental protocol used was similar to the one described in the previous chapter. Results based on the spectral fit model are shown in Figure 6.2 (a) and 6.2(b). It can be seen that the ESS is consistently larger for NTHi than for Sp and NTHi + Sp. Furthermore, the trend shown in these estimates confirms the findings of an increase in the integrated backscatter as a function of maturity.

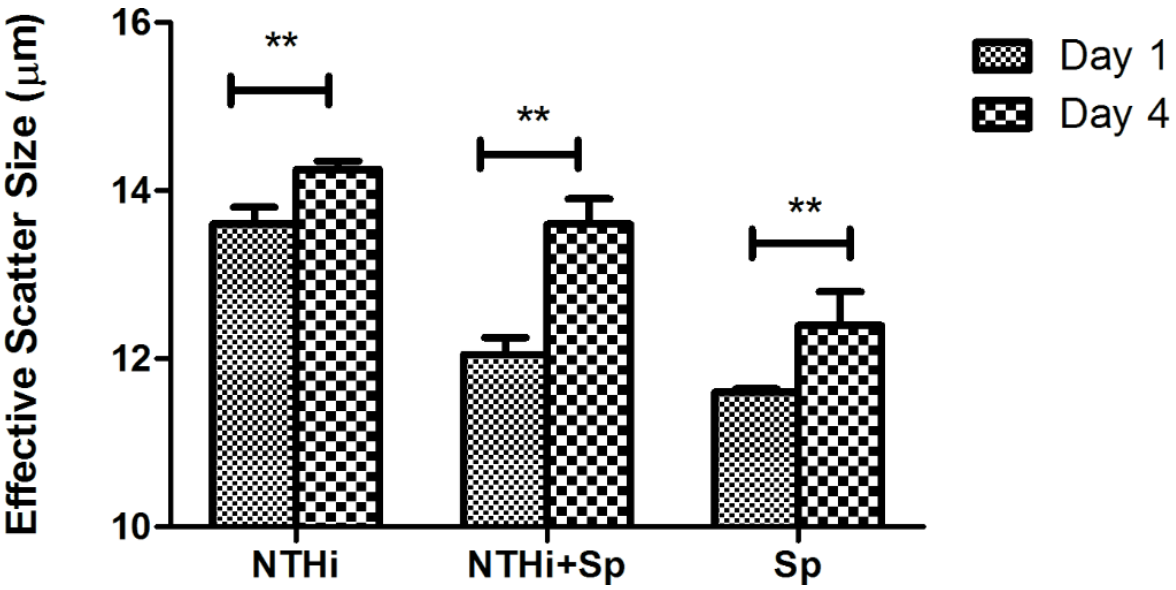

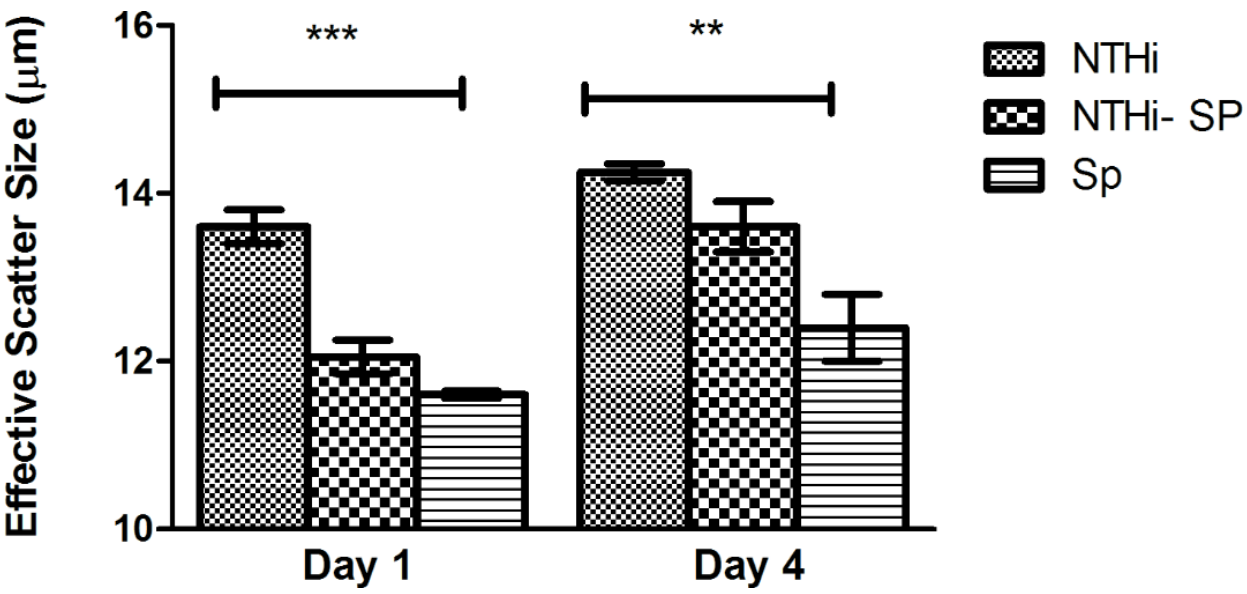

Figure 6.2 (a): Results of unpaired t-test on trends within samples as a function of maturity for ESS, (b) One-way ANOVA results between samples for ESS

The metrics described in this Chapter and Chapter 5 give a quantitative evaluation of the acoustic properties of biofilms. The data collected using a 15MHz transducer does not produce high resolution images of biofilm structure. The smallest structure resolvable at this frequency is around 200 microns. In theory the use of higher frequency can help resolve smaller structures.

An attempt was made to generate high resolution images using an acoustic microscope which uses a 130MHz single element transducer. The purpose of this exercise was to see if images produced using the data collected from this system could be used to qualitatively evaluate the differences between the three cases considered in this study.

Qualitative assessment of the week-old biofilms was achieved by using a PSS-18 scanning acoustic microscope fitted with a 130 MHz single element piston transducer. A 6 mm by 6 mm raster scan with a step size of 20 μm was performed to obtain C-scan images of each

sample. This system allowed us to generate higher resolution images of the biofilms. Figure 5.6 shows that it was impossible to differentiate among single- and multi-species biofilms. These images support the argument that quantitative analysis is necessary to characterize biofilms with the goal in mind to help physicians with a more accurate diagnosis.

Quantitative analysis could not be performed based on acoustic microscopy because the acoustic microscope does not provide access to the RF data.

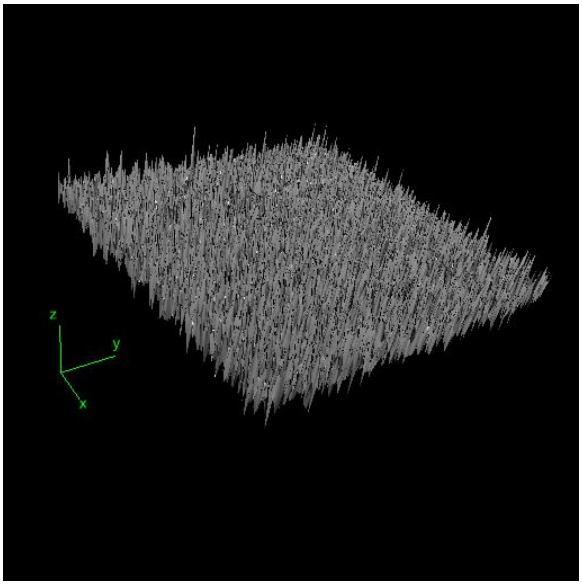

(a)

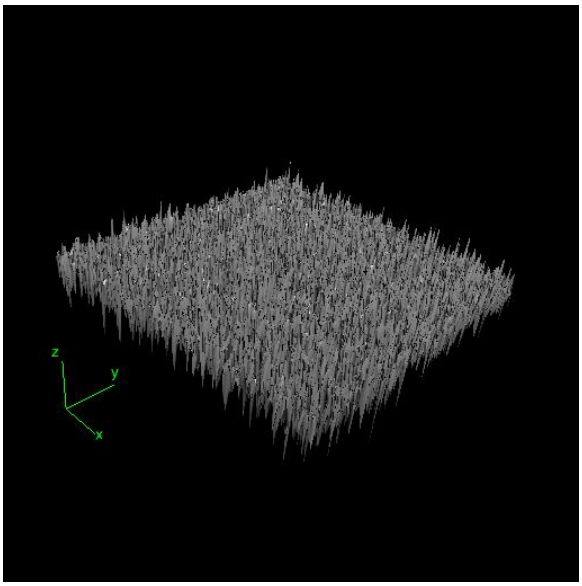

(b)

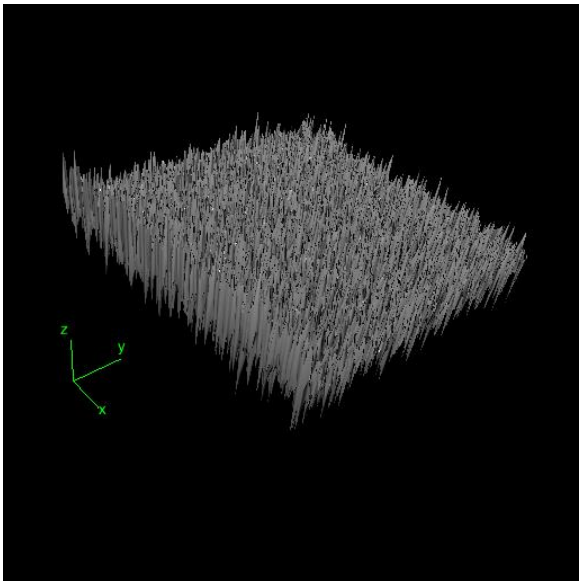

(c)

Figure 6.3: C-scan images of (a) NTHi; (b) Sp; and (c) NTHi + Sp

These results prove that the ultrasound modality is not ideally suited to produce high resolution images that can be used to study the structural properties of biofilm without the

use of mathematical form factor models. The next chapter describes the use of a Confocal Microscope to overcome the limitations of ultrasound imaging.

Chapter 7

7.1 Confocal Microscopy

Confocal laser scanning microscopy (CSLM) is an optical technique widely used for imaging microorganisms. CSLM is a useful tool in studying the growth of biofilms. It is a non-destructive and non-invasive method with the capability to provide time-resolved three dimensional images of biofilms.

Gennip *et al.* [18]demonstrated the use of CSLM to visualize biofilm development *in vivo* following intraperitoneal inoculation of mice with bacteria growing on hollow silicone tubes, as well as to examine the interaction between these bacteria and the host innate immune response.

Although the use of CSLM for biofilm studies is quite common and wide spread it is mostly used for qualitative visual evaluation. Quantitative evaluation of these high-resolution data can uncover trends in biofilm growth, which may prove to be crucial in the detection and recognition of different strains. There have been attempts in the past to develop an automated quantitative approach to characterizing biofilm growth based on confocal data. Heydron *et al.* [19] developed the computer program COMSTAT to automate the characterization process based on quantitative metrics. Mueller *et al.* [54] developed PHLIP(Phobia Laser Scanning Microscopy Imaging Processor), which has functionality similar to COMSTAT. Each of these programs import three-dimensional stacks of images, pre-process them, and make measurements based on quantitative metrics designed to highlight properties of biofilm growth as a function of time. The existing code

base which is freely available to researchers was used and modified to do quantitative evaluation of the three cases considered in this study. The software developed was used to study the biofilm species previously studied using high frequency ultrasound. To the best of our knowledge there is no published data that evaluate the species of biofilms used in this study. Since a large percentage of infections are caused by these species our results were a first attempt at archiving the structural properties of these biofilms and corroborating the trends discovered with independent ultrasound-based experiments.

Quantitative ultrasound analyses described in previous chapters do not provide structural information of biofilms due to the limitation in resolution at the wavelength of the ultrasound used. As demonstrated in previous chapters numerous metrics were developed and used to differentiate between the three cases in this study. None of these metrics give us any real information about the underlying structure of the biofilms. In other words the quantitative analyses lack the ability to differentiate between the species based on the structural orientation at the cellular level. In order to corroborate our ultrasound-based findings, confocal microscopy was used to independently to verify trends observed previously.

7.2 Working of a Confocal Laser Scanning Microscope

It is important to understand the working of a confocal microscope to appreciate the improvement in quantitative analysis of biofilms that it allows. Figure 7.1 [55] shows a schematic that demonstrates how confocal microscopy produces high-resolution images. Panel 1 shows that the image of a cell in the target volume produces an image at a certain focal distance. Another cell will produce an image at a different focal distance. Panel 2

shows that light from a source can be focused onto a certain cell in the target volume and a pinhole could be used to capture the image from that cell and its vicinity alone and block light from any other cell in the target volume. Panel three demonstrates that a light source confocal with the cell and the pinhole could be used to illuminate the cell of interest alone and block light from any other location in the target volume. This process ensures that the image produced is of the highest resolution. If the entire target volume was imaged by changing the focal distance of the source and the pin hole accordingly in theory it would be possible to collect high resolution data which could then be reconstructed to produce a high resolution three-dimensional stack of images. A beam splitter can be used to deflect the light from the cell towards a detector that records the light and converts it into an electrical signal proportional to the intensity of the light.

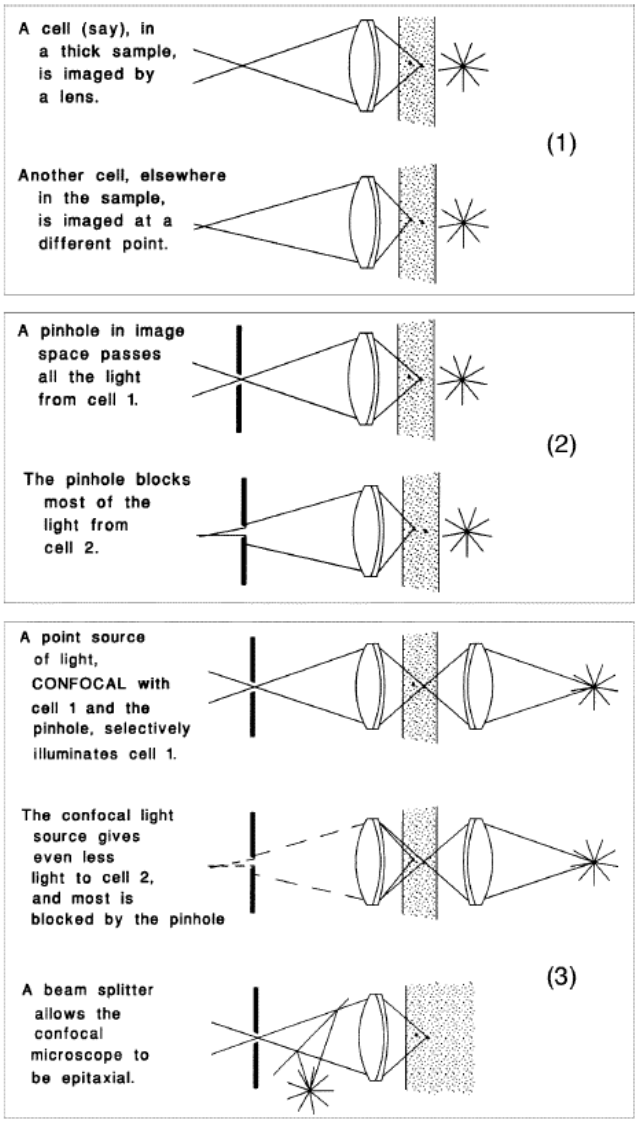

Figure 7.1. Confocal Microscopy. [55]

This is the basic fundamental idea behind confocal microscopy. The scanning process ensures that no energy reaches the detector from areas not in the beam, and so the contrast is not spoiled by unwanted background photons. The advantage of confocal microscopy is that it is capable of producing a three-dimensional stack of high-resolution data. This allows us to reconstruct the structure of the biofilm attached to the substrate. Periodic confocal images show the progression of the biofilm with time and the three-dimensional

stacks of data were subjected to a quantitative analysis to study changes in biofilm properties.

CSLM uses a monochromatic source of light, which has a much lower wavelength as compared to ultrasound. This ensures much higher resolution compared to ultrasound imaging and enables us to study the structure of biofilms, which was not possible with ultrasound studies.

7.3 Experimental Protocol

In order to validate the ultrasound findings, a similar experimental protocol (N=3) was followed to investigate the characteristics of the biofilm producing species of bacteria under study. The images were collected on a Leica TCS SP5 II AOBS Filter-free Tunable Spectral Confocal Research Microscope with Resonant Scanner and Hybrid Detectors (Leica Microsystems Inc., 1700 Leider Lane, Buffalo Grove, IL) attached to a Leica DMI6000 Fully Automated Microscope using Leica LAS system software mounted with a 40X 0.7NA 3.3 mm water objective. All cultures were stained with green biofilm stain (FilmTracer FM 1-43, Invitrogen Carlsbad CA). 16 bit images were acquired at a step size of between 0.5µm to 1 µm. The voxel length and width varied between 0.38µm to 0.52µm.

7.4 Three-dimensional quantitative analysis

Three dimensional stack of images are imported via the confocal microscope imaging software LEICA LAS LITE. Before any of these data can be analyzed the stacks go through some preprocessing to ensure the accuracy of subsequent algorithms. Preprocessing comprises of the following steps

- Thresholding – This converts the images in every stack from a gray level image to a binary image based on a user defined value per acquisition. A user defined value worked better than automated thresholding algorithms because it is hard to recreate the acquisition parameters during experiments. This step is also referred to as pixel classification where each of the pixels are either corresponding to the biofilm structure or the background.
- Connected Volume filtration – The purpose of this step is to eliminate pixels in the 3D stack that are not connected to the substratum. This gets rid of free floating particles in the media and ensures that our data are in compliance with the definition of the biofilm which requires the biomass to be attached to the substratum. The algorithm considers the substratum that is chosen by the user as the starting point and then moves up the slices to implement connected volume filtration. Defining the layer that is the substratum is crucial to the accuracy of this process. The image acquisition is performed in a fashion that records slices of images within a predefined window chosen by the user. The user visually verifies that the entire 3D volume of the biofilm is contained within this window. Within this window the substratum can be identified by locating the slice that is densely populated, preceded by a slice that is significantly devoid of any features and followed by a slice that is visually similar to the substratum while moving from the lower slices in an upward direction.

Once the data have been pre-processed the following metrics were used to characterize the data:

- *Biovolume coverage*:

After the segmentation algorithm weeds out free floating pixels in the foreground the biofilm volume can be calculated by multiplying the number of pixels in the whole stack with the voxel size. The biovolume divided by the total available volume in the image stack is the biovolume metric, which is indicative of the percentage coverage of the biofilm in the volumetric dataset.

- *Thickness distribution*:

This function locates the highest point (µm) above each (*x*,*y*) pixel in the bottom layer containing biovolume coverage. Hence, thickness is defined as the maximum thickness over a given location, ignoring pores and voids inside the biofilm. The thickness distribution can be used to calculate a range of variables, including biofilm roughness and mean biofilm thickness.

- *Maximum thickness*:

This is the maximum thickness corresponding to the highest point (µm) located amongst all the pixels in the image.

- Roughness coefficient: This is a measure of how much the thickness of the biofilm varies and is an indicator of biofilm heterogeneity. The roughness coefficient can be calculated based on the following equation [56].

$$R_a^* = \frac{1}{N}\sum_{i=1}^{N}\frac{\left|L_{fi} - \overline{L_f}\right|}{\overline{L_f}} \qquad (1)$$

  - L_{fi}- ith individual thickness
  - $\overline{L_f}$ – Mean Thickness of biofilm in all stacks
  - N− Number of thickness measurement

A small value of roughness coefficient signifies a smoother and more uniform biofilm. Biofilms with more mature colonies are usually not as uniform and therefore report higher roughness coefficient values.

Figure 7.2 shows the proposed approach for quantitative evaluation of the structure of biofilms.

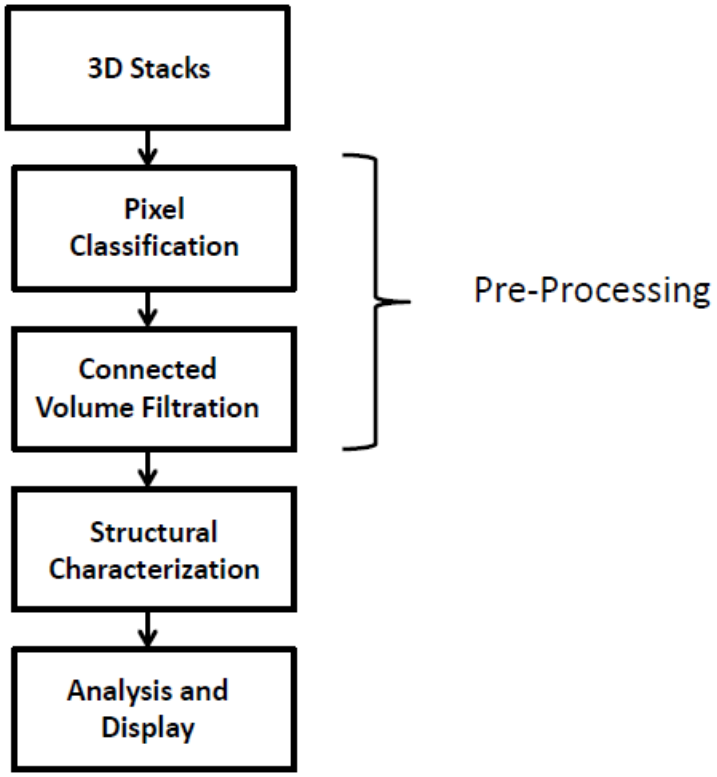

Figure 7.2: Proposed approach

7.5 Results

Scans of the biofilm cultures were conducted on Days 1 and 4 after inoculation. Three independent repeats of longitudinal studies for each case, namely, Nontypeable *Haemophilus influenzae* (NTHi) biofilms, *Streptococcus pneumoniae* (Sp) biofilms, and a

co-cultured *Haemophilus influenzae* and *Streptococcus pneumoniae* (NTHi+Sp) biofilms were considered. Figures 7.3, 7.4 and 7.5 show a confocal image of NTHi, NTHi+Sp and Sp one day after inoculation. Figures 7.6, 7.7 and 7.8 show the thickness distribution of the three cases considered in the study. The color bars indicate thickness in micrometers and the image dimensions are 1024x1024 pixels.

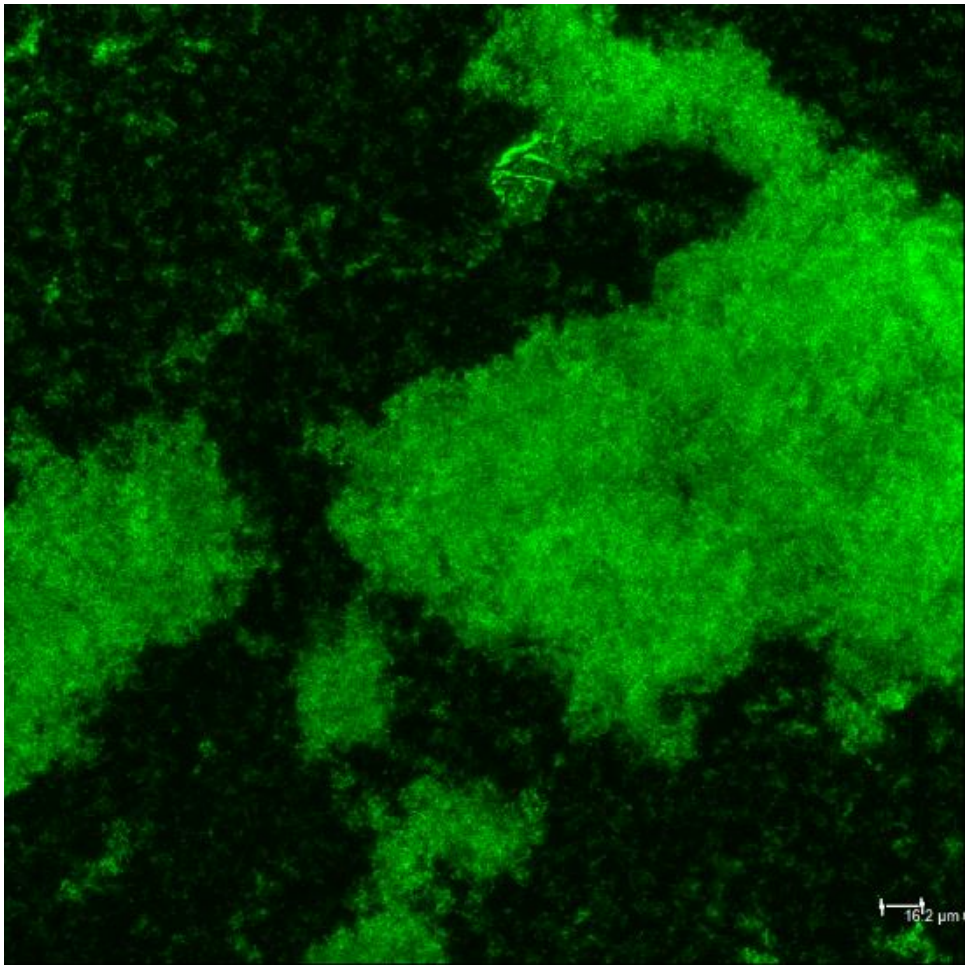

Figure7.3: Confocal image of NTHi one day after inoculation (Scale bar = 16.2µm)

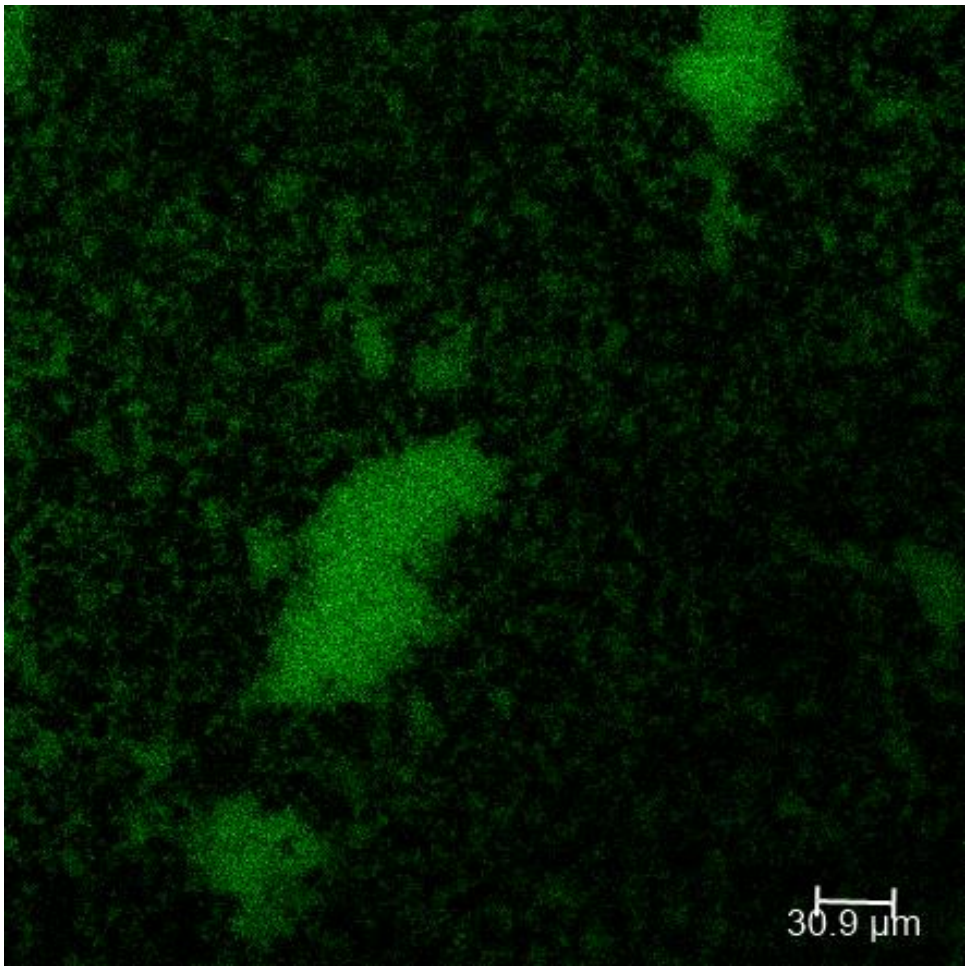

Figure 7.4: Confocal image of NTHi-Sp one day after inoculation (Scale bar = 30.9µm)

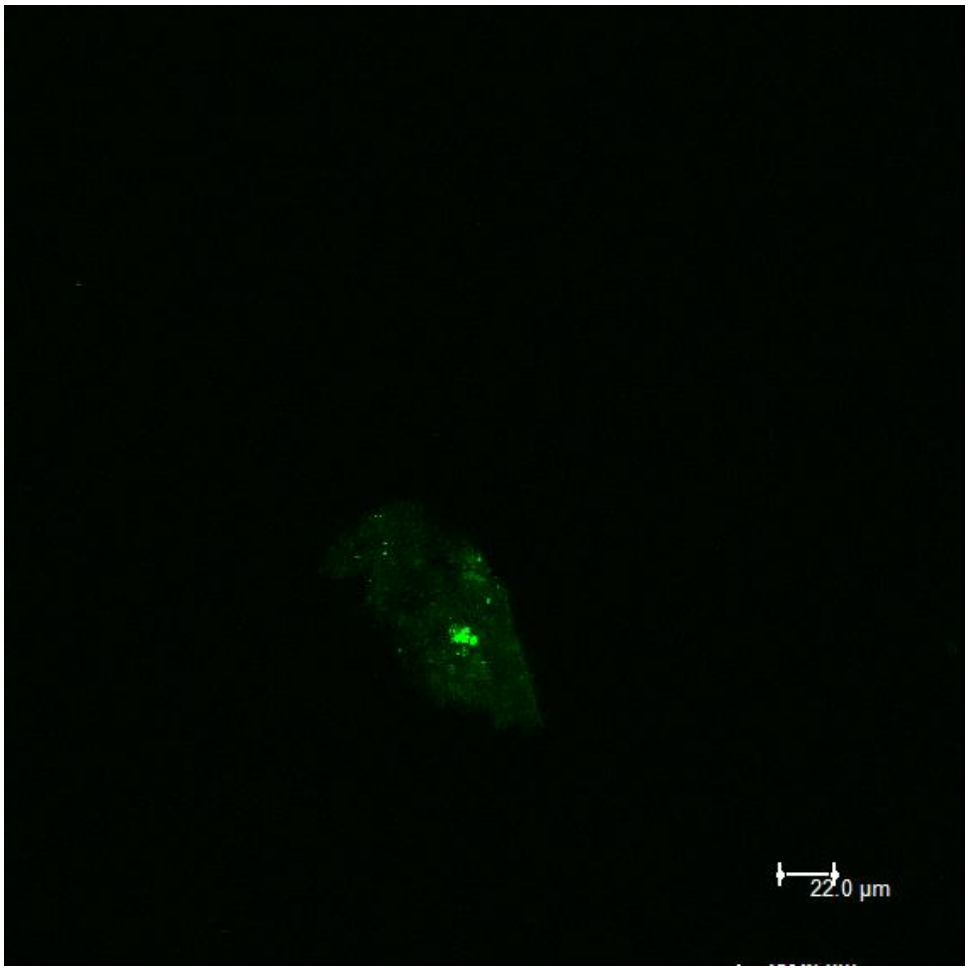

Figure 7.5: Confocal image of Sp one day after inoculation (Scale bar = 22.0µm)

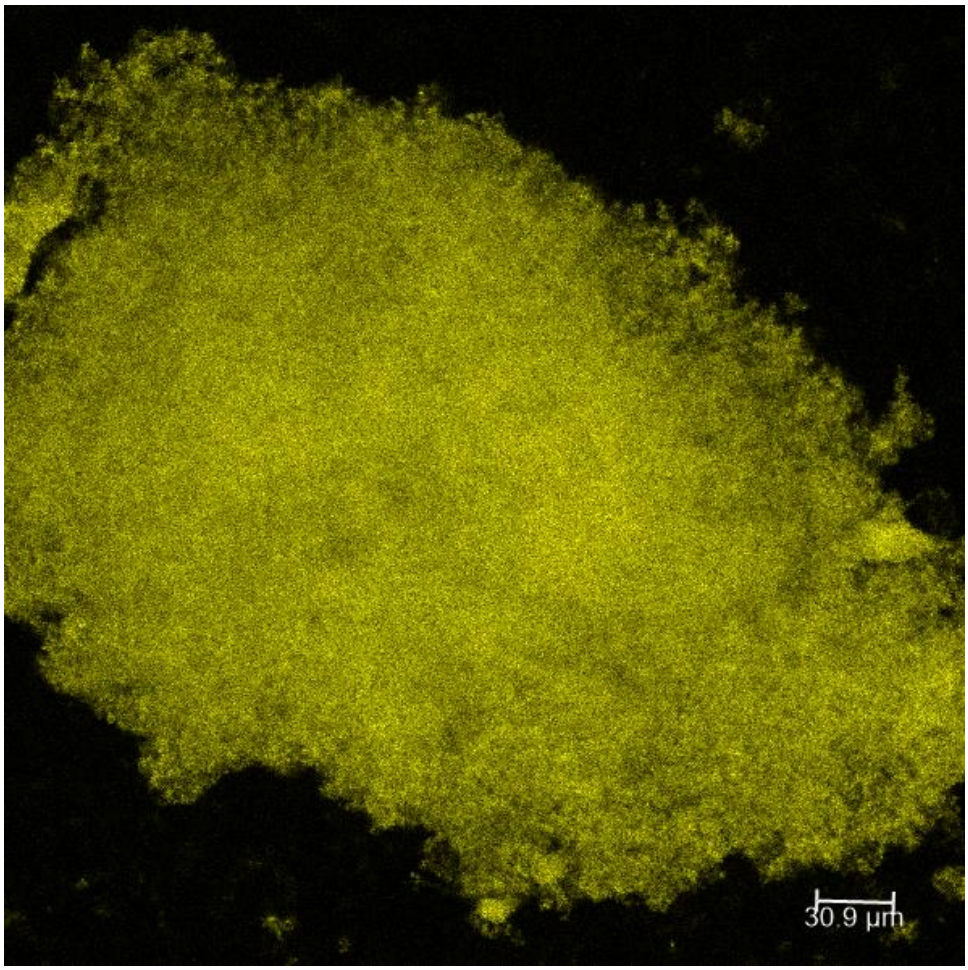

Figure 7.6: Confocal image of NTHi 4 days after inoculation (Scale bar = 30.9µm)

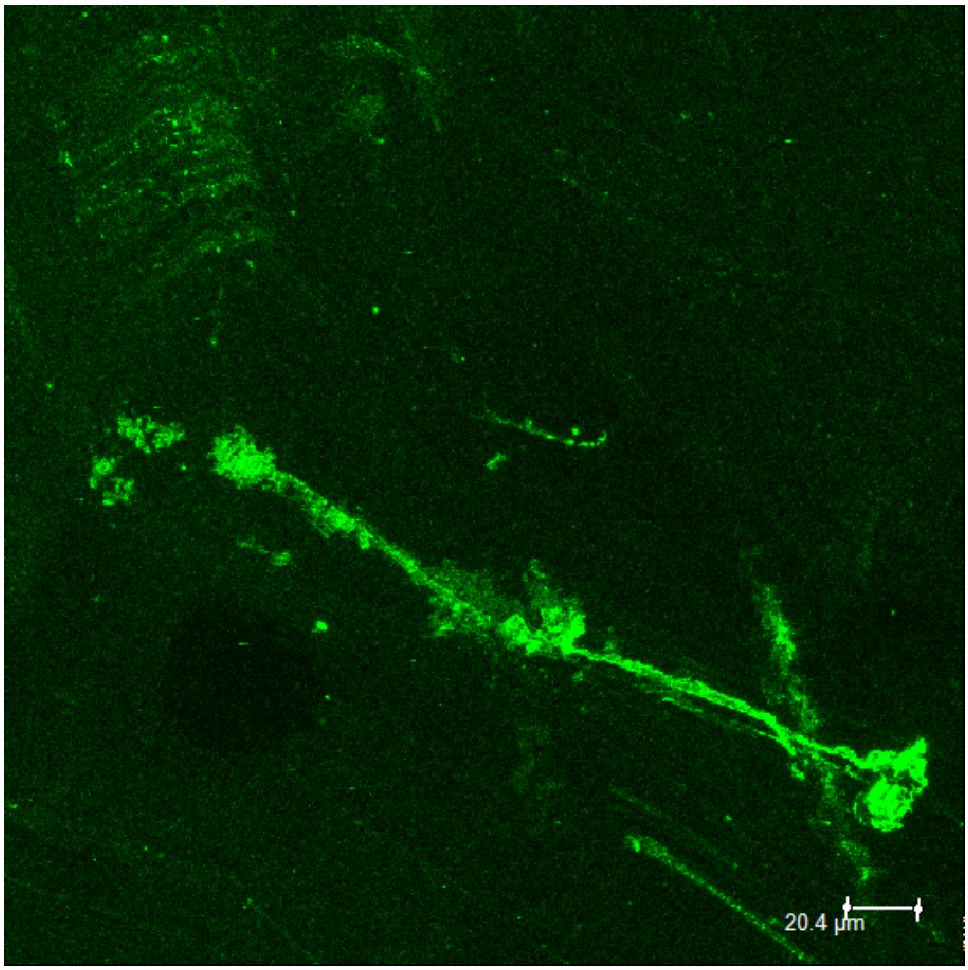

Figure 7.7: Confocal image of NTHi+Sp 4 days after inoculation (Scale bar = 20.4µm)

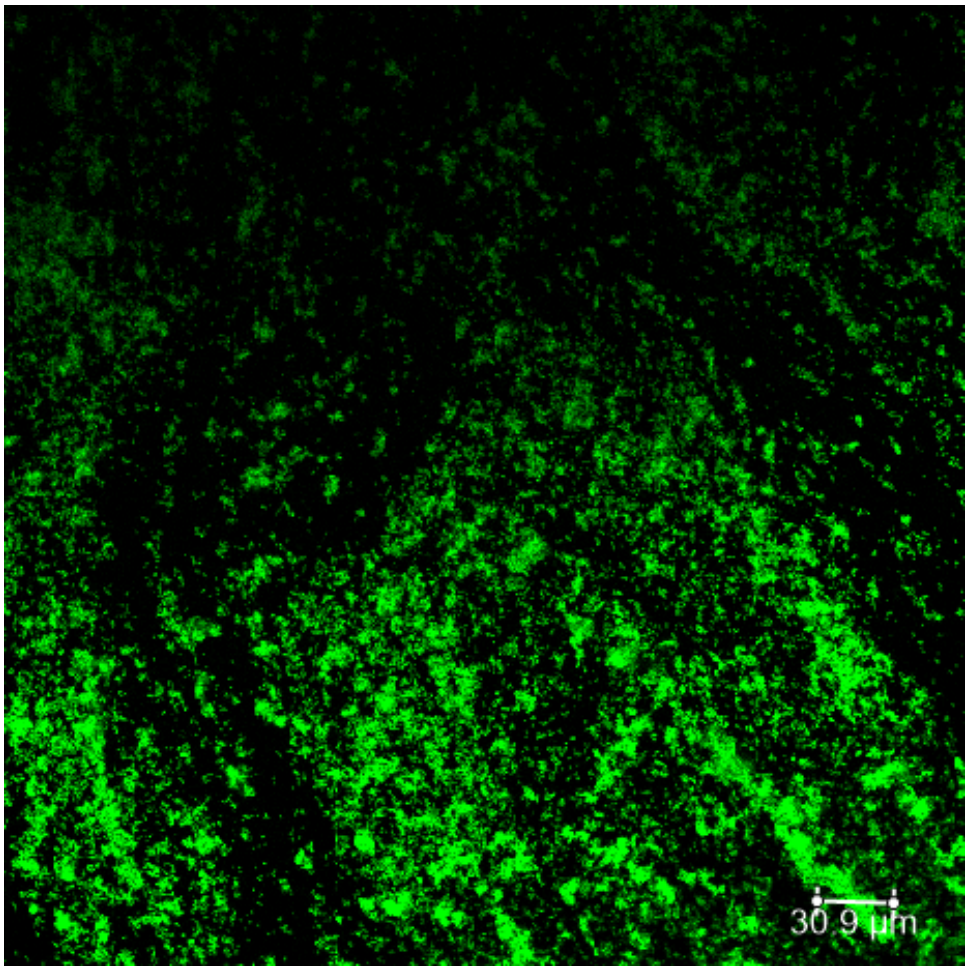

Figure 7.8: Confocal image of Sp 4 days after inoculation (Scale bar = 30.9µm)

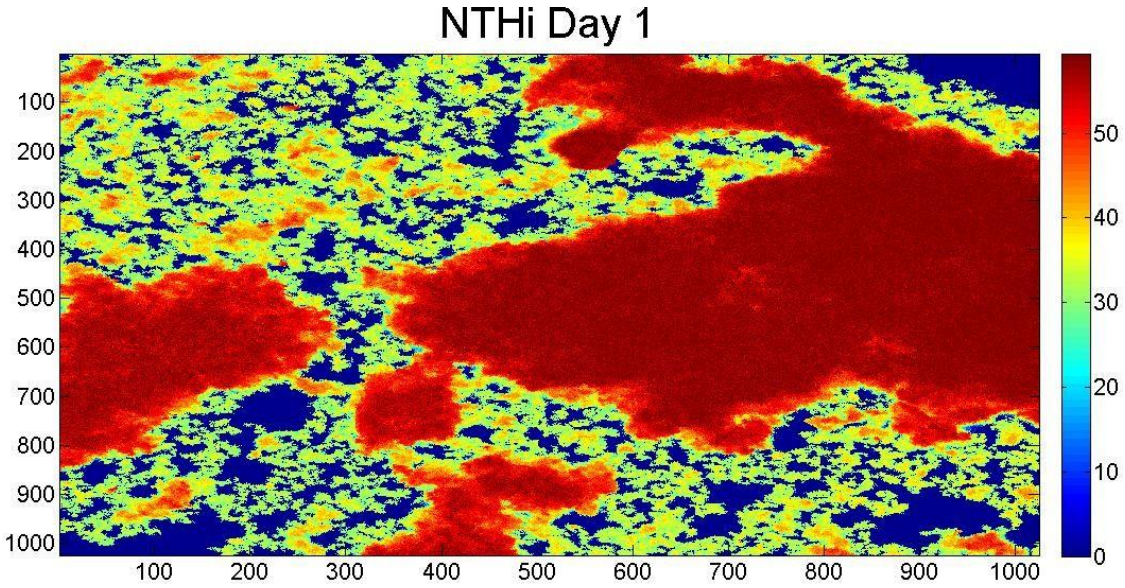

Figure 7.9: Thickness distribution map of NTHi one day after inoculation (Color bar indicates thickness in µm, X and Y axis shows pixel number)

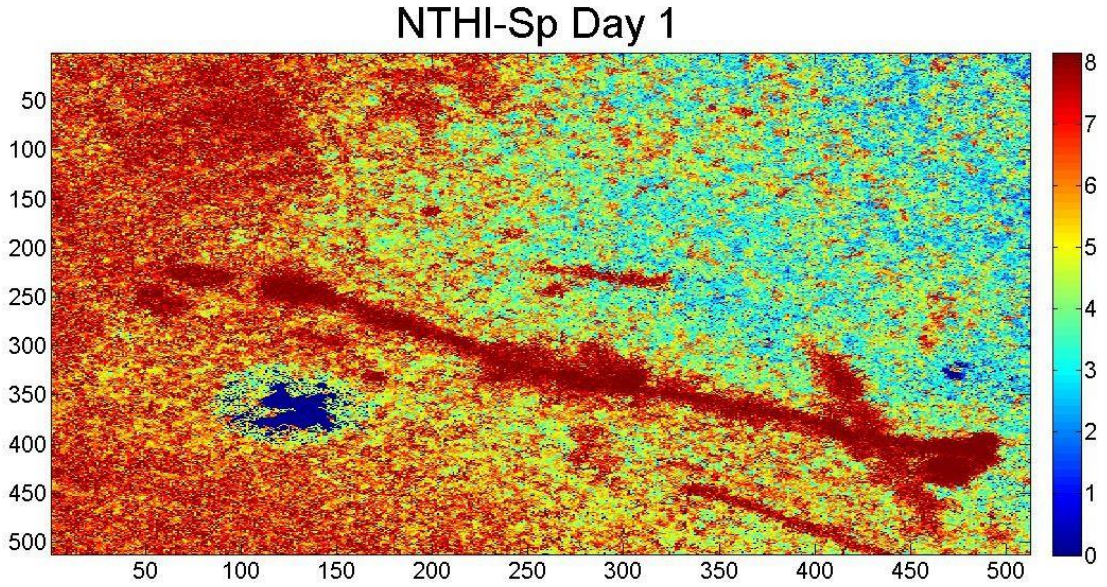

Figure 7.10: Thickness distribution map of NTHi+Sp one day after inoculation (Color bar indicates thickness in µm, X and Y axis shows pixel number)

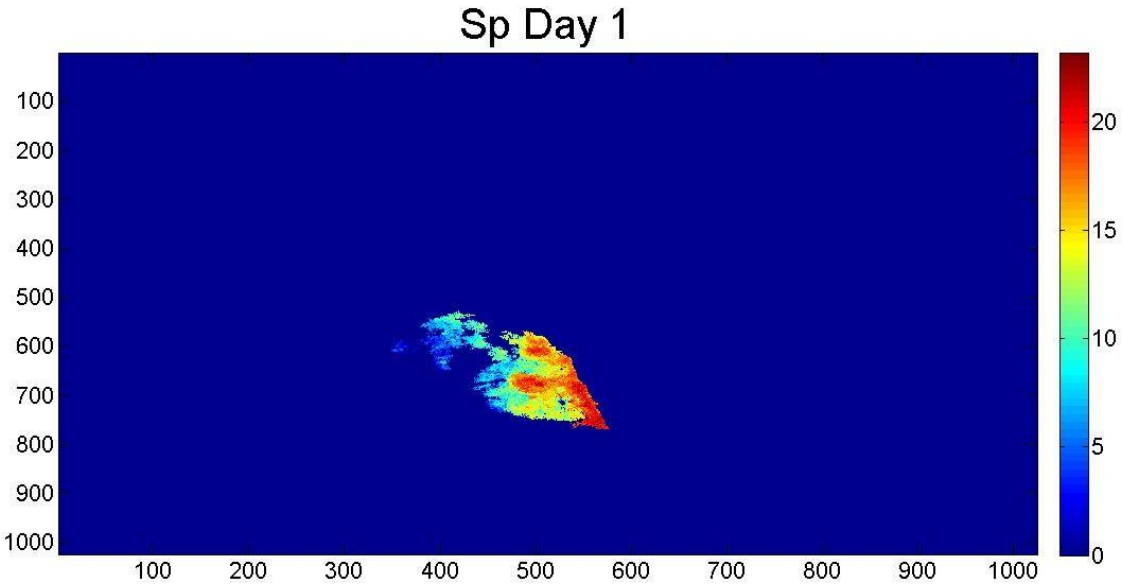

Figure 7.11: Thickness distribution map of Sp one day after inoculation (Color bar indicates thickness in μm, X and Y axis shows pixel number)

Values of the metrics described were mapped as a function of time. Results are analyzed using Prism 6^{TM}, where unpaired t-tests with a 95% confidence interval were performed to determine whether the means of the metrics considered are significantly different between Days 1 and 4 for each strain. One-way ANOVA tests were performed to determine significantly different results amongst the three cases considered on Days 1 and 4. Absence of significance bars indicate that the results for those respective cases were not significant. Figures 7.12, 7.13, 7.14 and 7.15 show the results plotted for the three cases considered in the experiment. Figure 7.12 shows that NTHi produces the thickest biofilm in comparison to the other two cases. Also, there is a significant increase in the thickness of all the cases considered on Day 4 compared to Day 1. It is

interesting to note that the thickness of NTHi +Sp is significantly lesser than NTHi alone. Figure 7.13 shows the Biovolume coverage for the three cases considered. Here also NTHi reports the highest value signifying widespread growth although again the combination of NTHi and Sp have a significantly lower value. The trend observed using this metric is similar to the one observed using the Average thickness. In both Figure 7.12 and Figure 7.13 Sp reports the lowest value indicative of a smaller or weaker biofilm formation. Figure 7.14 shows the change in Roughness Coefficient. Here, the trends observed are in alignment with Biovolume and Average thickness where NTHi forms the most heterogeneous biofilm followed by NTHi+Sp and Sp. In Figure 7.15 (a) which shows the area of the biofilm at the substratum we see that there is not much change for all three cases individually between Day 1 and Day 4. However the area at the substratum is significantly different between the three cases on the same days as shown in Figure 7.15 (b). This signifies that micro colonies at the substratum remain relatively unchanged and is therefore indicative of growth in the upward direction. The next section describes these results in the context of the ultrasound experiments.

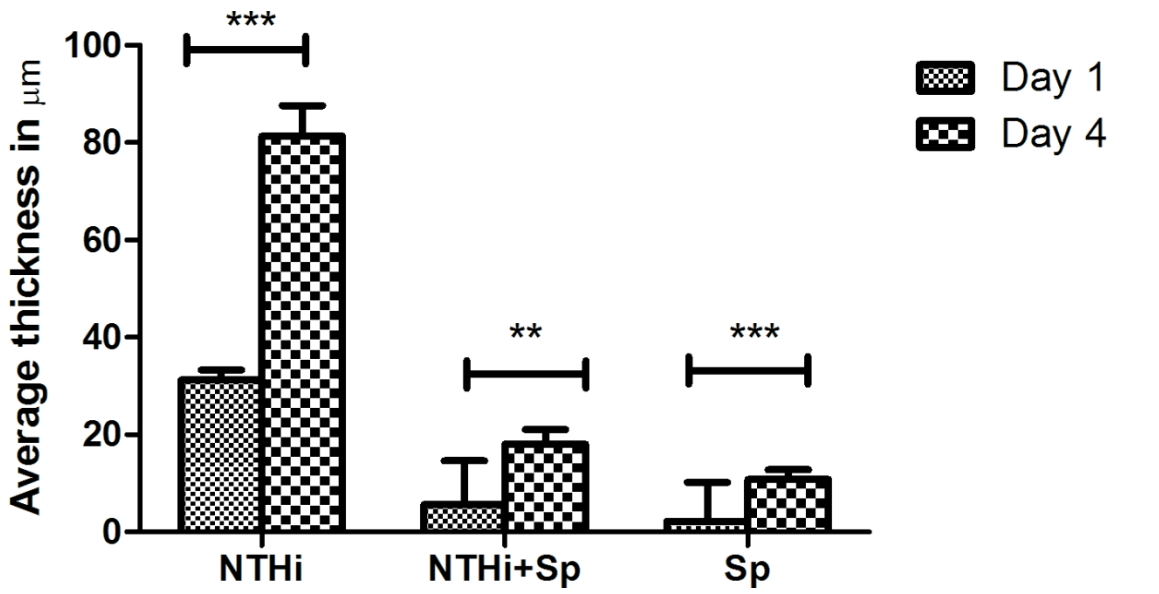

a.

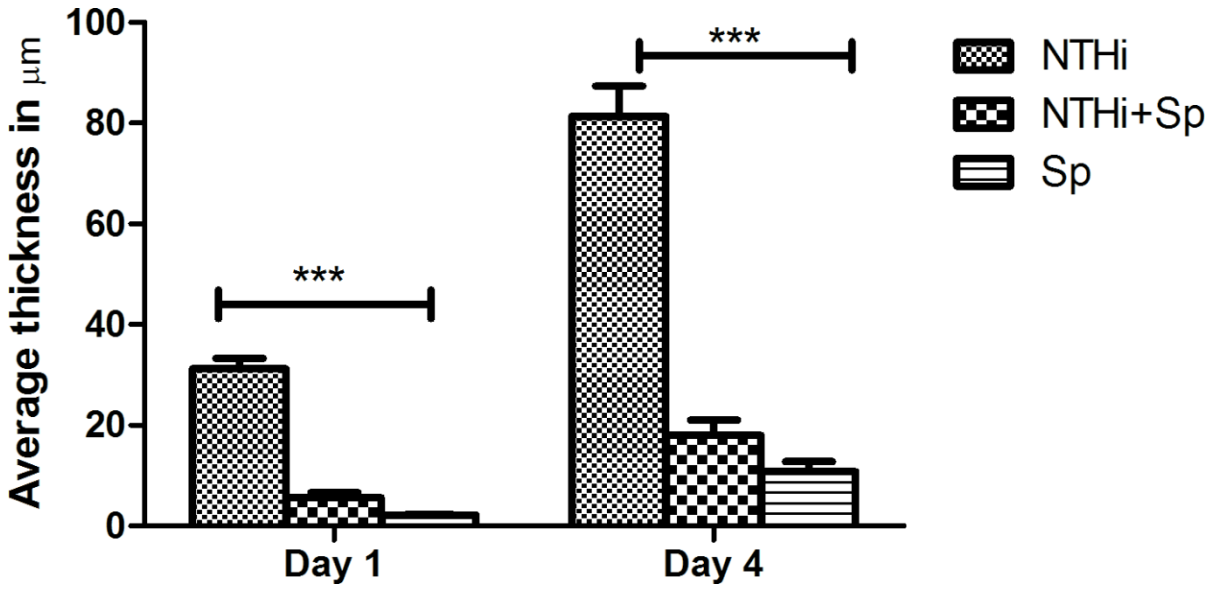

b.

Figure 7.12 (a) t-test results for Average thickness based on confocal data at $p<0.001$ for NTHi, $p<0.001$ for NTHi+Sp and $p<0.009$ for Sp. 10 (b) One way ANOVA test results for Average thickness across species for each day, values significant at $p<0.002$ for Day 1 and $p<0.001$ for Day 4.

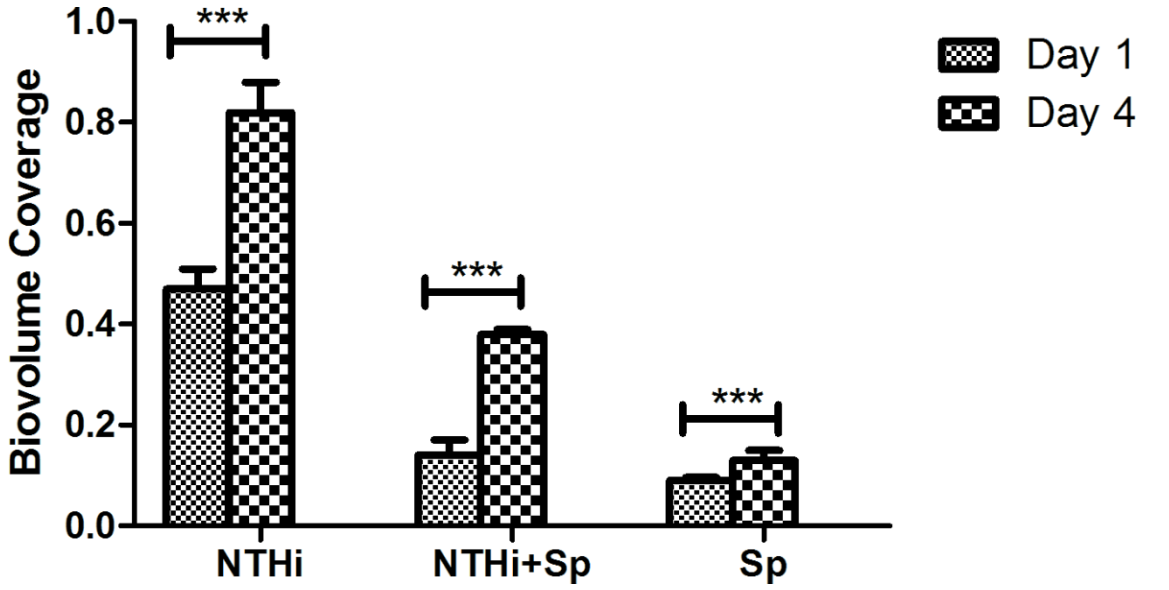

a.

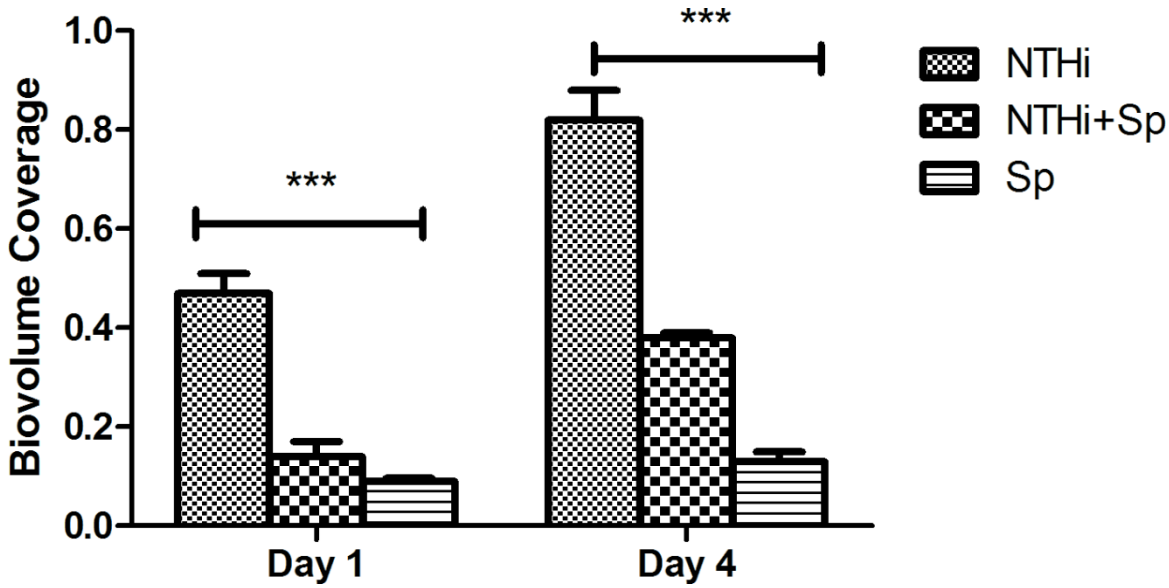

b.

Figure 7.13 (a) t-test results for Biovolume coverage based on confocal data at $p<0.001$ for NTHi, $p<0.001$ for NTHi+Sp and $p<0.006$ for Sp. 10 (b) One way ANOVA test results for Biovolume coverage across species for each day, values significant at $p<0.002$ for Day 1 and $p<0.002$ for Day 4.

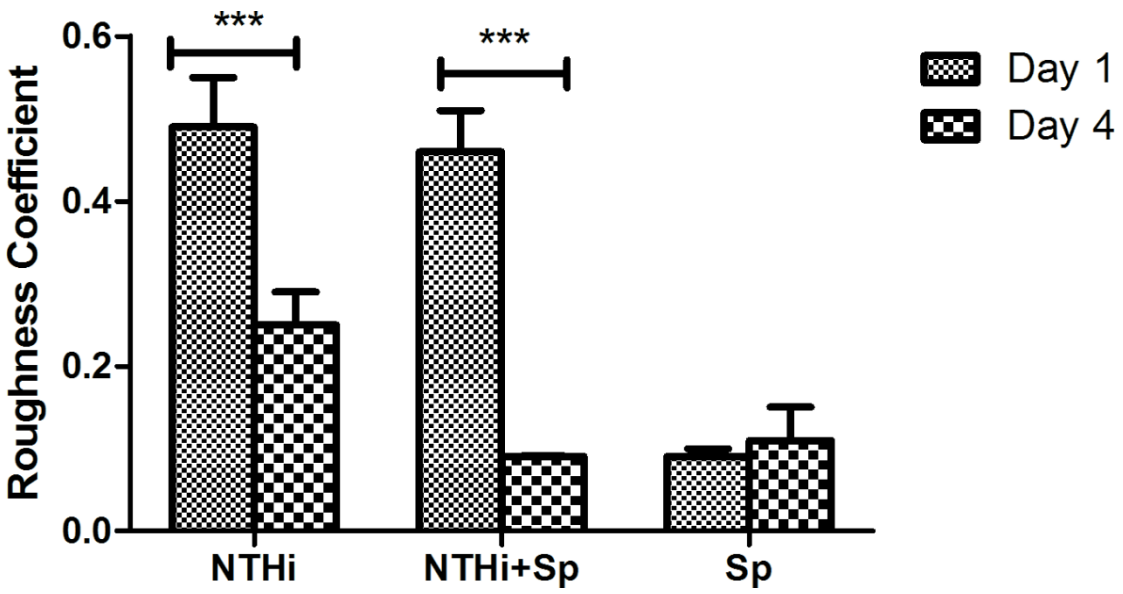

a.

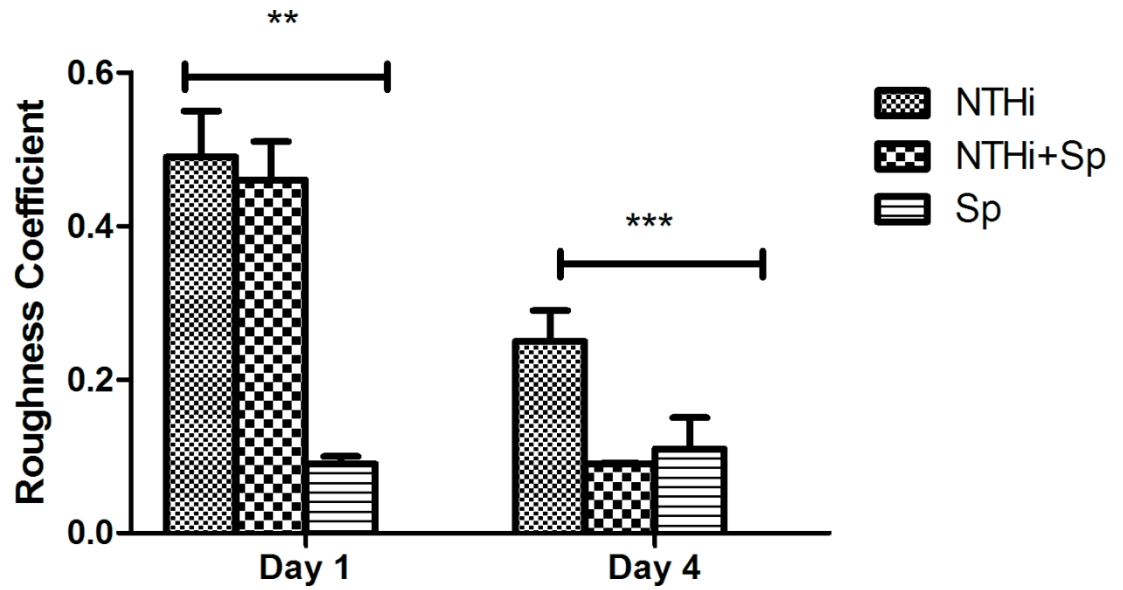

b.

Figure 7.14 (a) t-test results for Roughness coefficient based on confocal data at $p<0.001$ for NTHi, $p<0.001$ for NTHi+Sp and $p<0.009$ for Sp. 10 (b) One way ANOVA test results for Roughness coefficient across species for each day, values significant at $p<0.001$ for Day 1 and $p<0.001$ for Day 4.

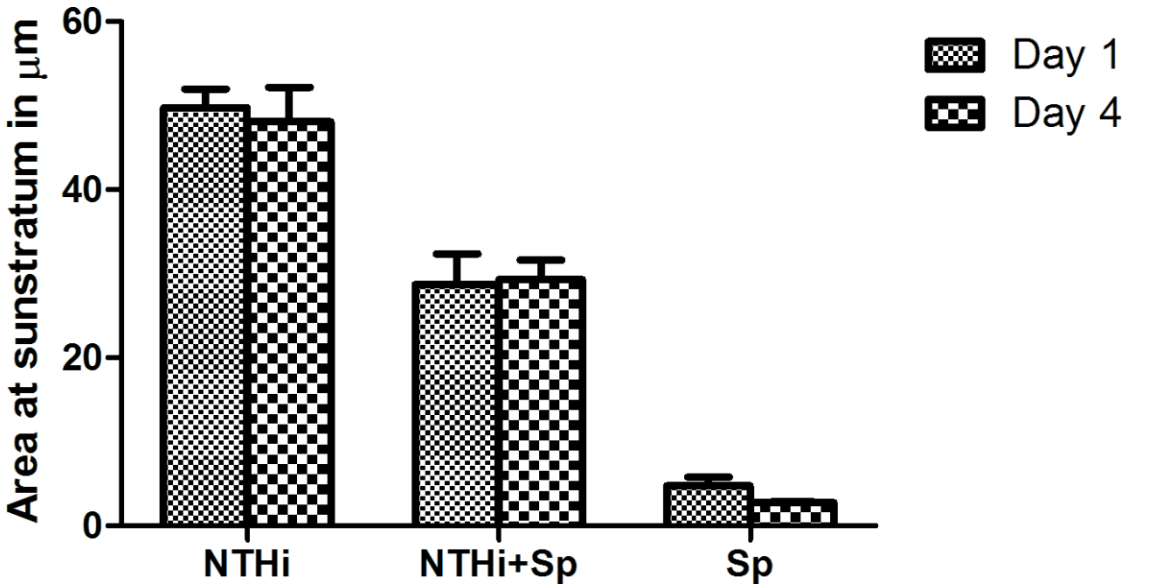

a.

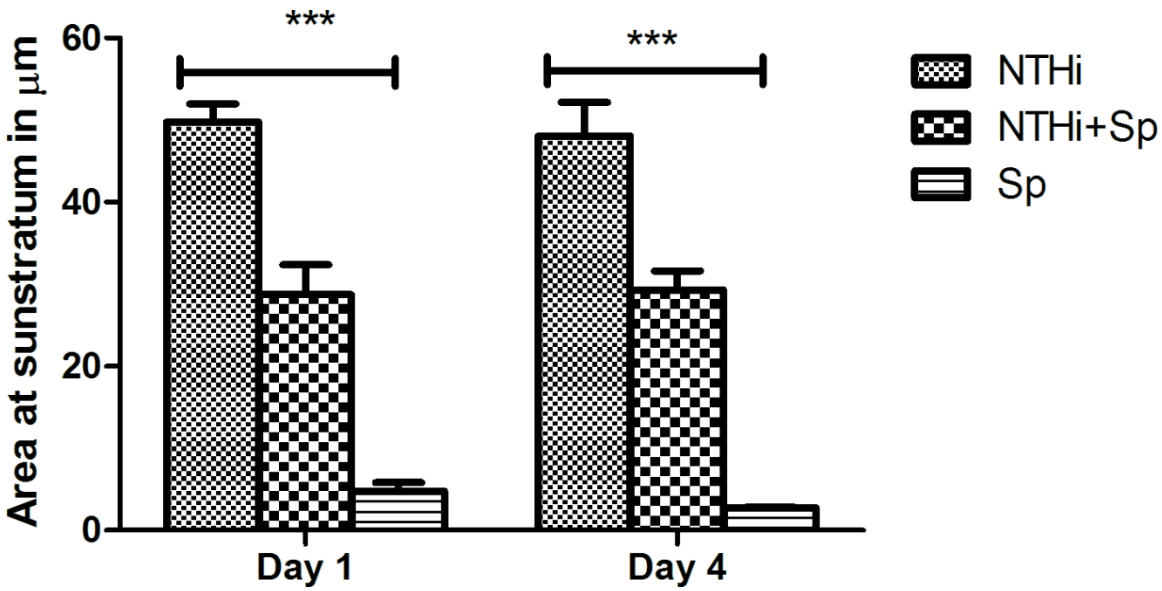

b.

Figure 7.15 (a) t-test results for Area at substratum based on confocal data for NTHi, NTHi+Sp ans Sp 10 (b) One way ANOVA test results for Area at substratum across species for each day, values significant at $p<0.002$ for Day 1 and $p<0.002$ for Day 4.

CHAPTER 8

8.1 Comparison of Results based on Confocal Microscopy and Ultrasound

It is important to present results of the confocal experiments in the context of our ultrasound experiments. To summarize, ultrasound data analyses were performed on 100 independent A-lines, where each A-line consists of 50002 data points. Results are given as mean$\pm$sem ($\alpha = 0.05$) for three repeats of each case under consideration (N = 3). The results for the two independent modalities are compared based on the following parameters.

- *Thickness*

Results from the two independent imaging modalities conducted confirm that as biofilms mature they grow thicker and denser regardless of the specie although the rate of growth varies among the species. Table 1 shows the thickness measurements for the three cases considered based on ultrasound and confocal data. Since the two experiments are independent of each other no quantitative comparison of the results was performed. The results from both modalities show NTHi to produce the thickest biofilm followed by NTHi+Sp and Sp. It is important to note that the table shows thickness estimates of different biofilms cultured over different times for the two experiments and hence a direct quantitative comparison would not be appropriate.

Table 1: Comparison of thickness estimates based on ultrasound and confocal data

	Ultrasound based thickness		Confocal Microscopy Thickness	
	Day 1	Day 4	Day 1	Day 4
NTHi	19.21±1.69	91.54±6.99	31.81± 1.69	81.81± 6.19
NTHi-Sp	12.34±2.11	56.33±4.21	5.00± 1.40	18.12± 2.88
Sp	16.97±1.18	45.58±3.96	2.11 ±0.09	10.81± 1.19

These results also point towards the suppressive nature of Sp which impedes the growth of a biofilm in a co-culture. Weimer *et al.* [10] also reported this observation in their clinical study. Xu *et al.* in [57] also show that in a co-culture NTHi predominates over Sp. In an *in vitro* study of competition, Sp always overpowered NTHi by attacking it with hydrogen peroxide and stripping off the surface molecules it needs for survival [58]. These results present a strong correlation in the trends observed using data from the two independent modalities.

- *Attenuation*

Ultrasound propagation in soft tissues is frequency dependent. High frequencies are attenuated more than lower frequencies. Due to the frequency dependent attenuation, the spectrum of a backscattered broadband ultrasound pulse experiences a downshift in its center frequency and a reduction in the bandwidth. These spectral modifications are related to the attenuation characteristics in the tissue.

When compared to the reference spectrum from a perfect reflector a downshift in center frequency for all experimental samples was observed. Figure 8.1 (a) and 8.2 (b) based on ultrasound experiments show this trend in frequency downshift indicating that as biofilms grow thicker and denser attenuation increases.

Figures 8.1 (c) and 8.1 (d) based on ultrasound experiments show a reduction in 3dB bandwidth across species and across days when compared to the spectrum from a perfect reflector. Once again, these trends are indicative of increasing attenuation as a function of maturity. The changes in the spectral parameters observed are confirmed by the confocal experiments. Figures 8.1 (e) and 8.1 (f) based on confocal experiments show biovolume coverage across species and days demonstrating that NTHi produced the thicker, denser biofilm followed by NTHi+Sp and Sp. The two independent modalities demonstrate similar trends.

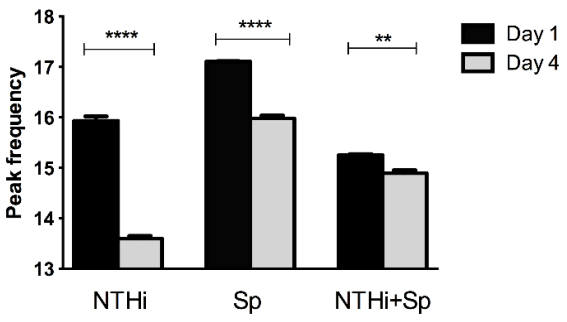

(a)

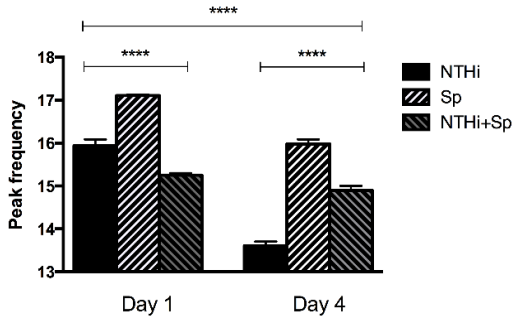

(b)

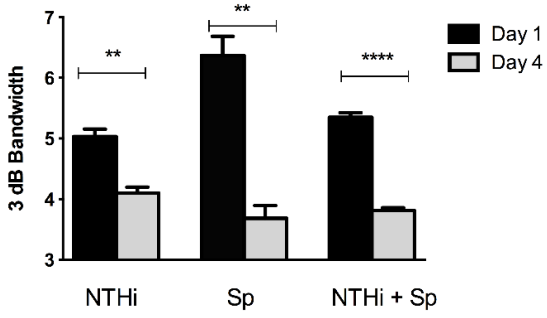

(b)

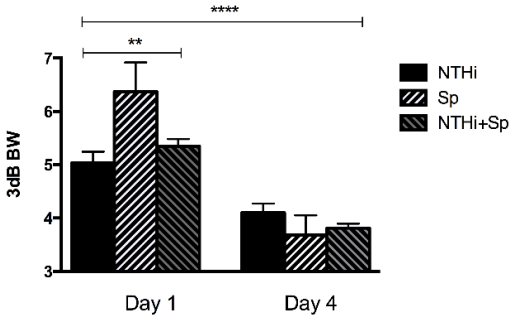

(d)

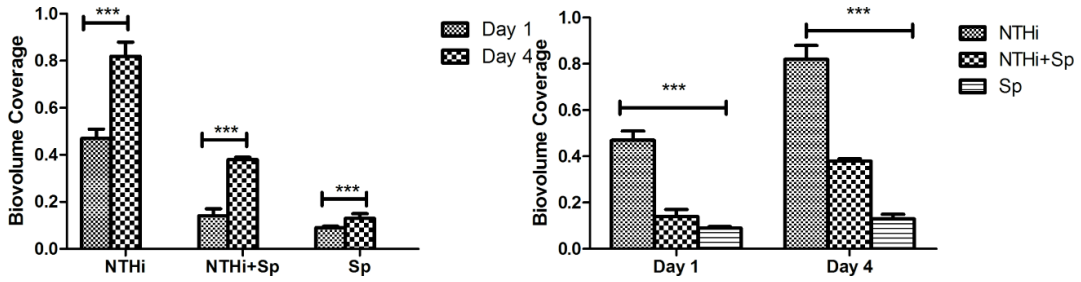

(e) (f)

Figure 8.1 (a) and (b) Changes in Peak Frequency (Ultrasound), (c) and (d) Changes in 3Db bandwidth (Ultrasound), (e) and (f) Changes in Bio-Volume Coverage (Confocal Miroscopy)

- *Scattering*

Quantitative backscatter measurements provide a measure of the mean-backscatter cross-section per unit volume, i.e. the effectiveness with which the biofilm scatters energy. Results based on the integrated backscatter measurements and the estimates of the effective scatter size show that this effectiveness increases as the biofilm mature.

Figures 8.2 (a) and (b) show the changes in the Biofilm/Bck metric based on IBC to be significantly different. The plots shows that this metric increases as the biofilm matures and is indicative of an increase of backscattered energy.

The effective scatterer size (ESS) was estimated by using a Gaussian autocorrelation function to describe scatterers in the biofilm. However, the validity of such a Gaussian model to describe bacterial aggregates should consider the fact that the size of these aggregates may evolve with time. Therefore, results after implementing the model discussed in Chapter 6 are shown in Figure 8.2 (c) and (d). It can be seen that the ESS is consistently larger for NTHi than for Sp and NTHi + Sp. Furthermore, the trend shown in these estimates confirms the findings of an increase in the integrated backscatter as a function of maturity. The ESS reported lies within the range of values that the chosen model

can predict.

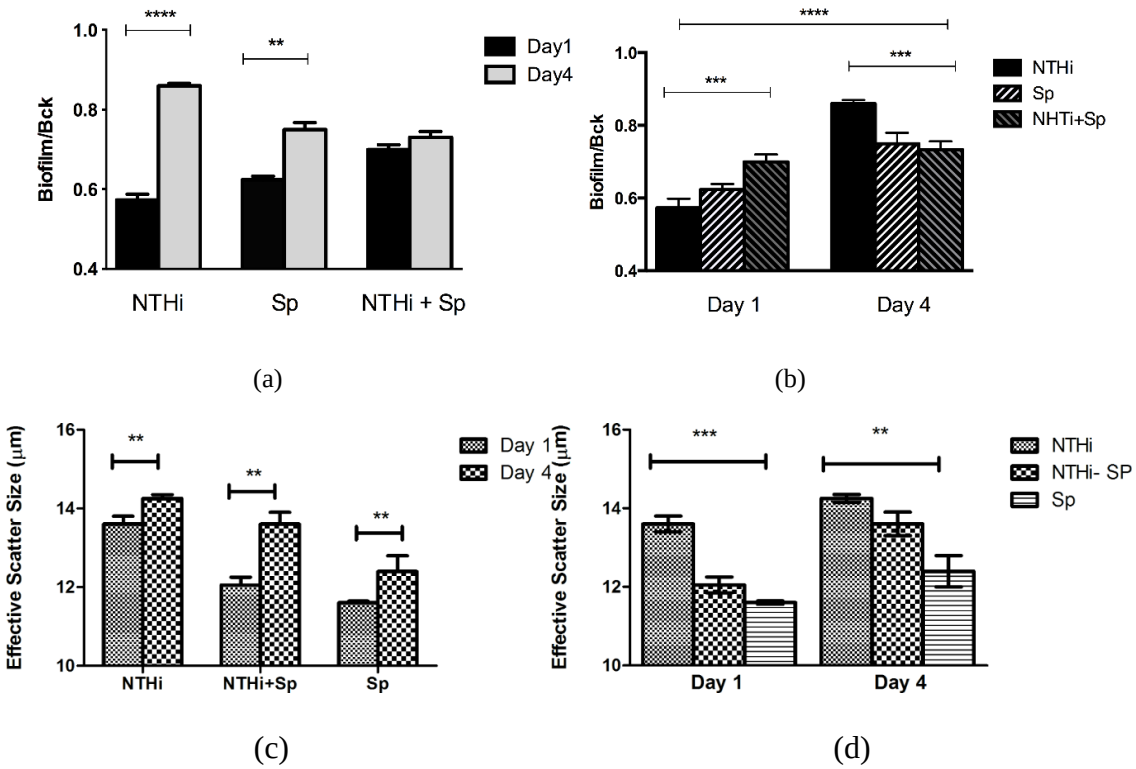

Figure 8.2 (a) and (b) Changes in Biofilm/Bck ratio (Ultrasound), (d) and (e) Changes in Effective Scatter Size (Ultrasound)

8.2 Conclusion and Discussion

These trends demonstrate that the results reported by ultrasound-based experiments are in agreement with those reported by the confocal experiments. The purpose of this comparison is to prove that ultrasound analysis is a viable modality for biofilm characterization. Despite the superior resolution of data provided by confocal microscopy this modality cannot be used in a clinical setting in real time. If ultrasound can give us reasonable information to characterize and differentiate between species of biofilms

despite its limitations, then a clinically relevant system can be developed to characterize biofilms. Ultrasound is a cost effective way of identifying bacterial species that cause infections. There are other challenges that would need to be addressed to perform this analysis in an in vivo environment that are outside the scope of this dissertation. However, the results of this study conclusively prove that ultrasound has the potential to characterize biofilms in the clinic.

8.3 Recommendations for extension of work

Our results demonstrate the capability of the ultrasound modality in the detection and identification of biofilm. One of the problems with implementing this in a clinical setting is the lack of access to the RF data in commercial scanners. This problem can be overcome by using advanced circuits to allow access to the RF data or by creating a prototype of a clinical probe attached to an acquisition system similar to the one used in this study. These techniques would not only be able to detect the biofilm but also quantify the presence in the form of various parameters as described here. In the future several other species of bacteria known to cause infection can be subjected to a similar analysis in order to archive a database of known parameters that could be unique to the different species.

Presently the use of a single element piston transducer causes the data acquisition time to be long. Commercially available ultrasound systems that use phased or linear arrays can be used for data acquisition. Some commercial scanners like the Ultrasonix SonixTouch Research system have access to various ultrasound imaging parameters so one can alter sequences, processing and other features for particular research applications. Additional software plug-ins can be developed in Matlab, Visual C++, communicate and synchronize with peripherals connected to the system. The use of linear or phased arrays can

tremendously reduce the acquisition time and all post- processing can be instantaneous after optimizing the software to generate results within the frame rate of the imaging system.

In a clinical environment these studies need to be performed *in vivo* and this presents many unique challenges. In order to scan the middle ear the ultrasound pulse needs a viable transmission path and greater depth of penetration. The attenuation will be significantly larger and will have to be appropriately compensated. SNR improvement and increasing depth of penetration will be important and the FM Chirp technique investigated in this study may prove to be beneficial at a lower frequency. Seth *et al.* have used a ultrasound probe to acquire RF echoes from the tympanic membrane to qualitatively characterize middle ear effusions [15]. A similar device could be used to acquire RF echoes from the tympanic membrane and quantitative techniques described in this dissertation can be used to provide a more comprehensive quantitative characterization of middle ear effusions. One disadvantage of such a device is the need to fill the ear canal with water which maybe a hindrance in young children.

An experimental protocol similar to the one used in my thesis work can be used to study the growth of biofilms grown on a monolayer of epithelial cells. The characterization metrics described in this thesis can be used to see the differences between the samples with and without the epithelial cells. This would also be an intermediate experiment between *in vitro* and *in vivo* analysis. In [59] Starner *et al.* show that NTHi forms biofilms in airway epithelia. Insights from Starner's study could be used to culture biofilms on epithelial cells for *ex vivo* analysis. In [60] Kania *et al.* characterize mucosal biofilms on human adenoid tissues. The possibility of growing biofilms on adenoids or tonsils can also be investigated

for *ex vivo* analysis. It would be interesting to study the RF echoes under these different environment to see if there is any change in the frequency content of the data.

As an intermediate step between *ex vivo* and *in vivo* analysis biofilm formation can be studied *in situ* utilizing a human infant mannequin applicable to simulation of middle ear infections developed by Dr. Michael Pichichero, Director of the Rochester General Hospital Research Institute. This mannequin was designed to train physicians to extract fluid from the middle ear cavity for analysis in a lab. Biofilm formation in the middle ear cavity of the mannequin can be attempted and an imaging protocol needs to be developed to acquire data using a modified data acquisition system. This mannequin has the average dimensions of a human infant head Figure 8.1(a). An artificial tympanic cavity, shown in Figure 8.1(b), can be inserted and positioned in the correct anatomical location, Figure 8.1(c). Attempts to acquire data from a mannequin should provide valuable insights into the problems of *in vivo* implementation. Data acquired can be subjected to a similar analysis as presented in this thesis.

a.

b.

c.

Figure 8.3. (a) Top view of phantom. (b) Tympanic cavity. (c) Inserting the tympanic cavity.

References

[1] R. G. Eagon, "Pseudomonas natriegens, a marine bacterium with a generation time of less than 10 minutes," *J Bacteriol,* vol. 83, pp. 736-7, Apr 1962.

[2] G. D. Ehrlich, R. Veeh, X. Wang, J. W. Costerton, J. D. Hayes, F. Z. Hu*, et al.*, "Mucosal biofilm formation on middle-ear mucosa in the chinchilla model of otitis media," *JAMA,* vol. 287, pp. 1710-5, Apr 3 2002.

[3] J. E. Bookwalter, J. A. Jurcisek, S. D. Gray-Owen, S. Fernandez, G. McGillivary, and L. O. Bakaletz, "A carcinoembryonic antigen-related cell adhesion molecule 1 homologue plays a pivotal role in nontypeable Haemophilus influenzae colonization of the chinchilla nasopharynx via the outer membrane protein P5-homologous adhesin," *Infect Immun,* vol. 76, pp. 48-55, Jan 2008.

[4] L. O. Bakaletz, "Bacterial biofilms in the upper airway - evidence for role in pathology and implications for treatment of otitis media," *Paediatr Respir Rev,* vol. 13, pp. 154-9, Sep 2012.

[5] J. R. Casey, D. G. Adlowitz, and M. E. Pichichero, "New patterns in the otopathogens causing acute otitis media six to eight years after introduction of pneumococcal conjugate vaccine," *Pediatr Infect Dis J,* vol. 29, pp. 304-9, Apr 2010.

[6] J. A. Jurcisek, J. E. Bookwalter, B. D. Baker, S. Fernandez, L. A. Novotny, R. S. Munson, Jr.*, et al.*, "The PilA protein of non-typeable Haemophilus influenzae plays a role in biofilm formation, adherence to epithelial cells and colonization of the mammalian upper respiratory tract," *Mol Microbiol,* vol. 65, pp. 1288-99, Sep 2007.

[7] E. J. Munoz-Elias, J. Marcano, and A. Camilli, "Isolation of Streptococcus pneumoniae biofilm mutants and their characterization during nasopharyngeal colonization," *Infect Immun,* vol. 76, pp. 5049-61, Nov 2008.

[8] W. Hong, K. Mason, J. Jurcisek, L. Novotny, L. O. Bakaletz, and W. E. Swords, "Phosphorylcholine decreases early inflammation and promotes the establishment of stable biofilm communities of nontypeable Haemophilus influenzae strain 86-028NP in a chinchilla model of otitis media," *Infect Immun,* vol. 75, pp. 958-65, Feb 2007.

[9] J. Jurcisek, L. Greiner, H. Watanabe, A. Zaleski, M. A. Apicella, and L. O. Bakaletz, "Role of sialic acid and complex carbohydrate biosynthesis in biofilm formation by nontypeable Haemophilus influenzae in the chinchilla middle ear," *Infect Immun,* vol. 73, pp. 3210-8, Jun 2005.

[10] K. E. Weimer, C. E. Armbruster, R. A. Juneau, W. Hong, B. Pang, and W. E. Swords, "Coinfection with Haemophilus influenzae promotes pneumococcal biofilm formation during experimental otitis media and impedes the progression of pneumococcal disease," *J Infect Dis,* vol. 202, pp. 1068-75, Oct 1 2010.

[11] H. Shemesh, D. E. Goertz, L. W. van der Sluis, N. de Jong, M. K. Wu, and P. R. Wesselink, "High frequency ultrasound imaging of a single-species biofilm," *J Dent,* vol. 35, pp. 673-8, Aug 2007.

[12] R. C. Waag, P. P. Lee, H. W. Persson, E. A. Schenk, and R. Gramiak, "Frequency-dependent angle scattering of ultrasound by liver," *J Acoust Soc Am,* vol. 72, pp. 343-52, Aug 1982.

[13] M. F. Insana, R. F. Wagner, D. G. Brown, and T. J. Hall, "Describing small-scale structure in random media using pulse-echo ultrasound," *J Acoust Soc Am,* vol. 87, pp. 179-92, Jan 1990.

[14] R. Libgot-Calle, F. Ossant, Y. Gruel, P. Lermusiaux, and F. Patat, "High frequency ultrasound device to investigate the acoustic properties of whole blood during coagulation," *Ultrasound Med Biol,* vol. 34, pp. 252-64, Feb 2008.

[15] R. Seth, C. M. Discolo, G. M. Palczewska, J. J. Lewandowski, and P. R. Krakovitz, "Ultrasound characterization of middle ear effusion," *Am J Otolaryngol,* vol. 34, pp. 44-50, Jan-Feb 2013.

[16] W. Liu and J. A. Zagzebski, "Trade-offs in data acquisition and processing parameters for backscatter and scatterer size estimations," *IEEE Trans Ultrason Ferroelectr Freq Control,* vol. 57, pp. 340-52, 2010.

[17] E. Kujundzic, A. C. Fonseca, E. A. Evans, M. Peterson, A. R. Greenberg, and M. Hernandez, "Ultrasonic monitoring of early-stage biofilm growth on polymeric surfaces," *J Microbiol Methods,* vol. 68, pp. 458-67, Mar 2007.

[18] M. van Gennip, L. D. Christensen, M. Alhede, K. Qvortrup, P. O. Jensen, N. Hoiby*, et al.*, "Interactions between polymorphonuclear leukocytes and Pseudomonas aeruginosa biofilms on silicone implants in vivo," *Infect Immun,* vol. 80, pp. 2601-7, Aug 2012.

[19] A. Heydorn, B. K. Ersboll, M. Hentzer, M. R. Parsek, M. Givskov, and S. Molin, "Experimental reproducibility in flow-chamber biofilms," *Microbiology,* vol. 146 (Pt 10), pp. 2409-15, Oct 2000.

[20] Macovski, *Basic Ultrasound Imaging*: Prentice-Hall, 1983.

[21] T. L. Szabo, *Diagnostic Imaging, Inside Out*: Elsevier, pp. 216-220 2004.

[22] T. L. Szabo, *Diagnostic Ultrasound Imaging: Inside out*: Elsevier, pp. 442-445 2004.

[23] M. El-Azizi, S. Rao, T. Kanchanapoom, and N. Khardori, "In vitro activity of vancomycin, quinupristin/dalfopristin, and linezolid against intact and disrupted biofilms of staphylococci," *Ann Clin Microbiol Antimicrob,* vol. 4, p. 2, 2005.

[24] O. M. Ward KH, Lam K, Costerton JW, "Mechanisms of persistent infection associated with peritoneal implants," *J Med Microbiol,* vol. 36, pp. 406-413, 1992.

[25] J. C. Post, "Direct evidence of bacterial biofilms in otitis media," *Laryngoscope,* vol. 111, pp. 2083-94, Dec 2001.

[26] N. G. Cogan and J. P. Keener, "The role of the biofilm matrix in structural development," *Math Med Biol,* vol. 21, pp. 147-66, Jun 2004.

[27] K. Todar, *Online textbook of Bacteriology* vol. 10.

[28] A. R. Foxwell, J. M. Kyd, and A. W. Cripps, "Nontypeable Haemophilus influenzae: pathogenesis and prevention," *Microbiol Mol Biol Rev,* vol. 62, pp. 294-308, Jun 1998.

[29] K. Todar, *Streptococcus pneumoniae: Pneumococcal Disease*, 2003.

[30] S. Venkatraman and N. A. Rao, "Combining pulse compression and adaptive drive signal design to inverse filter the transducer system response and improve resolution in medical ultrasound," *Med Biol Eng Comput,* vol. 34, pp. 318-20, Jul 1996.

[31] M. O'Donnell and S. D. Silverstein, "Optimum displacement for compound image generation in medical ultrasound," *IEEE Trans Ultrason Ferroelectr Freq Control,* vol. 35, pp. 470-6, 1988.

[32] S. W. M. Cook C.E, "The early history of pulse compression radar," *IEEE Trans Aerospace and Electronic Systems,* vol. 24, pp. 825-833, 1988.

[33] M. L. Oelze, "Bandwidth and resolution enhancement through pulse compression," *IEEE Trans Ultrason Ferroelectr Freq Control,* vol. 54, pp. 768-81, Apr 2007.

[34] B. Boashash and M. Mesbah, "A time-frequency approach for newborn seizure detection," *IEEE Eng Med Biol Mag,* vol. 20, pp. 54-64, Sep-Oct 2001.

[35] P. S. Addison, *The illustrated Wavelet Transform Handbook*: Instittue of Physics, 2002.

[36] M. Prelcic N, O, "An Interactive software for a Hypertext Course in Wavelets," *Proc. IEEE 24 Digital Signal Processing Workshop,* pp. 105-108, 1996.

[37] A. Jensen, la Cour-Harbo, A., *Ripples in Mathematics, The discrete Wavelet Transform.*: Springer, 2001.

[38] J. M. Thijssen, "Ultrasonic tissue characterisation and echographic imaging," *Phys Med Biol,* vol. 34, pp. 1667-74, Nov 1989.

[39] M. F. Insana and T. J. Hall, "Parametric ultrasound imaging from backscatter coefficient measurements: image formation and interpretation," *Ultrason Imaging,* vol. 12, pp. 245-67, Oct 1990.

[40] T. J. Hall, E. L. Madsen, F. Dong, I. R. Medina, and G. R. Frank, "Low-reflection-coefficient liquid interfaces for system characterization," *Ultrasound Med Biol,* vol. 27, pp. 1003-10, Jul 2001.

[41] M. M. McCormick, E. L. Madsen, M. E. Deaner, and T. Varghese, "Absolute backscatter coefficient estimates of tissue-mimicking phantoms in the 5-50 MHz frequency range," *J Acoust Soc Am,* vol. 130, pp. 737-43, Aug 2011.

[42] L. X. Yao, J. A. Zagzebski, and E. L. Madsen, "Backscatter coefficient measurements using a reference phantom to extract depth-dependent instrumentation factors," *Ultrason Imaging,* vol. 12, pp. 58-70, Jan 1990.

[43] M. C. Kolios, G. J. Czarnota, M. Lee, J. W. Hunt, and M. D. Sherar, "Ultrasonic spectral parameter characterization of apoptosis," *Ultrasound Med Biol,* vol. 28, pp. 589-97, May 2002.

[44] R. M. Vlad, S. Brand, A. Giles, M. C. Kolios, and G. J. Czarnota, "Quantitative ultrasound characterization of responses to radiotherapy in cancer mouse models," *Clin Cancer Res,* vol. 15, pp. 2067-75, Mar 15 2009.

[45] M. Gudur, R. R. Rao, Y. S. Hsiao, A. W. Peterson, C. X. Deng, and J. P. Stegemann, "Noninvasive, quantitative, spatiotemporal characterization of mineralization in three-dimensional collagen hydrogels using high-resolution spectral ultrasound imaging," *Tissue Eng Part C Methods,* vol. 18, pp. 935-46, Dec 2012.

[46] M. F. Insana, T. J. Hall, and L. T. Cook, "Backscatter coefficient estimation using array transducers," *IEEE Trans Ultrason Ferroelectr Freq Control,* vol. 41, pp. 714-23, 1994.

[47] K. Vaidya, R. Osgood, D. Ren, M. E. Pichichero, and M. Helguera, "Ultrasound Imaging and Characterization of Biofilms Based on Wavelet De-noised Radiofrequency Data," *Ultrasound Med Biol,* Dec 19 2013.

[48] F. L. Lizzi, M. Astor, E. J. Feleppa, M. Shao, and A. Kalisz, "Statistical framework for ultrasonic spectral parameter imaging," *Ultrasound Med Biol,* vol. 23, pp. 1371-82, 1997.

[49] F. L. Lizzi, M. Greenebaum, E. J. Feleppa, M. Elbaum, and D. J. Coleman, "Theoretical framework for spectrum analysis in ultrasonic tissue characterization," *J Acoust Soc Am,* vol. 73, pp. 1366-73, Apr 1983.

[50] F. J.J, "Sound scattering by solid cylinders and spheres," *J Acoust Soc Am,* vol. 23, pp. 405-418, 1951.

[51] I. K. U. Morse P.M, *Theoretical Acoustics, Chapter 8*: McGraw Hill, 1968.

[52] K. A. Wear, "A Gaussian framework for modeling effects of frequency-dependent attenuation, frequency-dependent scattering, and gating," *IEEE Trans Ultrason Ferroelectr Freq Control,* vol. 49, pp. 1572-82, Nov 2002.

[53] T. A. Bigelow and W. D. O'Brien, "Evaluation of the spectral fit algorithm as functions of frequency range and deltakaeff," *IEEE Trans Ultrason Ferroelectr Freq Control,* vol. 52, pp. 2003-10, Nov 2005.

[54] L. N. Mueller, J. F. de Brouwer, J. S. Almeida, L. J. Stal, and J. B. Xavier, "Analysis of a marine phototrophic biofilm by confocal laser scanning microscopy using the new image quantification software PHLIP," *BMC Ecol,* vol. 6, p. 1, 2006.

[55] R. H. Webb, "Confocal Optical Microscopy," *Rep. Prog. Phys,* pp. 427-471, 1996.

[56] R. Murga, P. S. Stewart, and D. Daly, "Quantitative analysis of biofilm thickness variability," *Biotechnol Bioeng,* vol. 45, pp. 503-10, Mar 20 1995.

[57] Q. Xu, J. R. Casey, A. Chang, and M. E. Pichichero, "When co-colonizing the nasopharynx haemophilus influenzae predominates over Streptococcus pneumoniae except serotype 19A strains to cause acute otitis media," *Pediatr Infect Dis J,* vol. 31, pp. 638-40, Jun 2012.

[58] C. D. Pericone, K. Overweg, P. W. Hermans, and J. N. Weiser, "Inhibitory and bactericidal effects of hydrogen peroxide production by Streptococcus pneumoniae on other inhabitants of the upper respiratory tract," *Infect Immun,* vol. 68, pp. 3990-7, Jul 2000.

[59] T. D. Starner, N. Zhang, G. Kim, M. A. Apicella, and P. B. McCray, Jr., "Haemophilus influenzae forms biofilms on airway epithelia: implications in cystic fibrosis," *Am J Respir Crit Care Med,* vol. 174, pp. 213-20, Jul 15 2006.

[60] R. E. Kania, G. E. Lamers, M. J. Vonk, E. Dorpmans, J. Struik, P. Tran Ba Huy*, et al.*, "Characterization of mucosal biofilms on human adenoid tissues," *Laryngoscope,* vol. 118, pp. 128-34, Jan 2008.